



Elina Hujala

**QUANTIFICATION OF LARGE STEAM BUBBLE
OSCILLATIONS AND CHUGGING USING
IMAGE ANALYSIS**



Elina Hujala

QUANTIFICATION OF LARGE STEAM BUBBLE OSCILLATIONS AND CHUGGING USING IMAGE ANALYSIS

Thesis for the degree of Doctor of Science (Technology) to be presented with due permission for public examination and criticism in Auditorium 1314 at Lappeenranta-Lahti University of Technology LUT, Lappeenranta, Finland on the 1st of November, 2019, at noon.

Acta Universitatis
Lappeenrantaensis 871

Supervisors Professor Juhani Hyvärinen
LUT School of Energy Systems
Lappeenranta-Lahti University of Technology LUT
Finland

Post-Doctoral Researcher Vesa Tanskanen
LUT School of Energy Systems
Lappeenranta-Lahti University of Technology LUT
Finland

Reviewers Professor Walter Ambrosini
Facoltà di Ingegneria
Università di Pisa
Italy

Dr Dominique Bestion
Commissariat à l'énergie atomique et aux énergies alternatives (CEA)
Centre d'Etudes de Grenoble
France

Opponent Mikko Lemmetty, D.Sc. (Tech.)
Teollisuuden Voima Oyj
Olkiluoto, Eurajoki
Finland

ISBN 978-952-335-424-1
ISBN 978-952-335-425-8 (PDF)
ISSN 1456-4491
ISSN-L 1456-4491

Lappeenranta-Lahti University of Technology LUT
LUT University Press 2019

Abstract

Elina Hujala

Quantification of large steam bubble oscillations and chugging using image analysis

Lappeenranta, 2019

69 p.

Acta Universitatis Lappeenrantaensis 871

Diss. Lappeenranta-Lahti University of Technology LUT

ISBN 978-952-335-424-1, ISBN 978-952-335-425-8 (PDF),

ISSN 1456-4491, ISSN-L 1456-4491

The pressure suppression pool of a boiling water reactor as a safety system has vital importance from the nuclear reactor safety point of view. If a loss-of-coolant accident occurs, a large amount of steam is pushed through the blowdown pipes to the suppression pool. Rapid condensation of steam causes high dynamic loads on the suppression pool structures and demands a great deal of its strength. These loads should be recognized and avoided.

A pattern recognition based image analysis algorithm for vertical vent pipes was designed and developed in this study. The direct contact condensation experiment (DCC-05) of the PPOOLEX test facility was used as a reference test. The algorithm consists of three parts: pre-processing, where all image processing takes place, pattern recognition, where the edges of the bubbles are detected, and post-processing part, where all images are analysed and data collected. The algorithm evaluates basic properties of large steam bubbles, such as volume, surface area, surface velocity and acceleration, and different frequencies.

Frequency analysis was also conducted on the DCC-05 case. The analysis showed two main frequencies 53 Hz and 126 Hz. The algorithm was also applied to computational fluid dynamics (CFD) simulations, where the algorithm was used to determine critical wavelengths of condensation driven Rayleigh-Taylor instability in succession to establish the most suitable grid density for the simulations. A frequency analysis was also performed for the CFD simulation cases and compared to the results of the algorithm.

The algorithm was extended to cover cases where multiple bubbles travel at the same time in the frame being analysed. The extended algorithm tracks multiple bubble properties in the same image. The evaluation of surface velocities and acceleration were also improved.

The algorithms work well in evaluating volume, surface area, velocities and accelerations of large steam bubbles. The research verified that even from moderate quality video material, it is possible to acquire high quality quantitative data, if the frame rate of video had been high enough and the most obtrusive objects

could be filtered out from it as well. The algorithms can help to understand phenomena that underlay the design of boiling water reactor (BWR) safety systems.

Keywords: direct contact condensation, large steam bubble, chugging, image processing, image analysis, FFT

Acknowledgements

The research of this thesis was carried out in the Laboratory of Nuclear Engineering at LUT University between 2014–2019. The research has received funding from the Finnish Programmes on Nuclear Power Plant Safety: SAFIR2014, SAFIR2018, and SAFIR2022.

I would like to express my gratitude to my supervisor, Professor Juhani Hyvärinen, for assistance in keeping my progress on schedule, and for useful critique of this research work. I am particularly grateful for the assistance given by my second supervisor, Dr Vesa Tanskanen for his patient guidance, and all the support he provided during the past years.

My special thanks are extended to Professor Emerita Riitta Kyrki-Rajamäki for her great lectures, which inspired me to join the world of nuclear engineering. I am also grateful to her for saving me when I “jäin pois” from the department of physics.

I warmly thank my reviewers, Professor Walter Ambrosini and Dr Dominique Bestion for their valuable and instructive suggestions and comments.

Altogether, I want to thank the whole staff of the Laboratory of Nuclear Engineering, especially co-author Dr Giteshkumar Patel, for his help with the writing process of the publications. I am really grateful to my Project Managers Markku Puustinen, Joonas Telkkä, and Lauri Pyy and our men in the laboratory: Antti Räsänen and Eetu Kotro for providing suitable experiments, although my requests were not always easy to follow or even realistic.

Special thanks goes to the members of our coffee group: the Star of the Seurahuone, Mrs Anne Jordan for being supportive both at the office and at the gym, Ville Rintala for being a peer support during the past years, Dr Juhani Vihavainen and Assistant Professor Heikki Suikkanen for making my life easier with the courses. I am also grateful to Riikka Hämäläinen and Tiina Kronqvist for all their help. Last but not least, I wish to thank Dr Heikki Purhonen for his support: 639 days to go.

Finally, I express my gratitude for my friends and family for their support. Especially, I want to thank Aki who is always there for me, even with English grammar.

Elina Hujala

October 2019

Lappeenranta, Finland

Contents

1	Introduction	13
1.1	Objective of the study	15
1.2	Research approach	15
1.3	Dissertation structure	16
2	Background	17
2.1	Nordic type boiling water reactor suppression pool system and its effects	17
2.1.1	Direct contact condensation of steam injected into water	19
2.2	Modelling of direct contact condensation	19
2.2.1	CFD modelling of direct contact condensation	20
2.2.2	Image processing and analysis of direct contact condensation experiments	21
2.2.3	Facility designed for algorithm development purposes	22
3	Review of the Results	23
3.1	Algorithm for vertical vent pipes	23
3.1.1	PPOOLEX test facility and DCC-05 experiment	23
3.1.2	Development of the algorithm	27
3.1.3	Estimated error of the algorithm	32
3.1.4	Evaluation of the basic properties of large steam bubbles	35
3.2	Frequency analysis	37
3.2.1	Analysis of the DCC-05-4 experiment	37
3.2.2	PPOOLEX hammer tests	41
3.2.3	Effect of the electricity grid	42
3.3	Modelling of DCC in pressure suppression pool systems	43
3.4	Extended algorithm for horizontal sparger orifice	47
3.4.1	SEF-POOL test facility and SEF-INF2 experiment	47
3.4.2	Development of the extended algorithm	50
3.4.3	Analysis of the SEF-INF2-6 experiment	53
4	Discussion	55
4.1	Recommendations for further research	58
5	Conclusions	61
	References	65
	Publications	

List of the original articles and the author's contribution

This thesis consists of an introductory part, three original, refereed articles in scientific journals and one original, refereed conference article. The articles and the author's contribution to them are summarized below.

- I E. Hujala, V. Tanskanen and J. Hyvärinen.** Pattern recognition algorithm for analysis of chugging direct contact condensation, *Nuclear Engineering and Design*, 332, pp. 202-212, 2018.
- II E. Hujala, V. Tanskanen and J. Hyvärinen.** Frequency analysis of chugging condensation in pressure suppression pool system with pattern recognition, *Nuclear Engineering and Design*, 339, pp. 244-252, 2018.
- III G. Patel, V. Tanskanen, E. Hujala and J. Hyvärinen.** Direct contact condensation modeling in pressure suppression pool system, *Nuclear Engineering and Design*, 321, pp. 328-342, 2017.
- IV E. Hujala, V. Tanskanen, G. Patel and J. Hyvärinen.** Image analysis of bubbling mode condensation oscillations in horizontal sparger, *The 18th International Topical Meeting on Nuclear Reactor Thermal Hydraulics (NURETH-18)*, Portland, Oregon, USA, August 18-23, 2019.

The author is the principal author of Publication I, Publication II and Publication IV and has participated in writing Publication III. In Publication III, author has calculated and analysed pattern recognition algorithm based quantities and evaluated frequencies in the computational fluid dynamics simulations.

Nomenclature

Symbols

A	bubble mode A
A	area
\mathbf{a}	acceleration
a_i	interfacial area density
B	bubble mode B
C	bubble mode C
d	diameter
d_i	number of nonzero elements
F_s	frame rate
f	frequency
f_0	natural frequency
G	mass flux
h	height
M	metric unit conversion factor
N	total number of images, number of cylinders
n	image number
P_0	steady state pressure
R_0	steady state radius
r	radius
r_1, r_2, r_3	triangle vertices 1–3
S	area of the patch
T	temperature
t	time
\mathbf{V}	vertex array
V	volume
\mathbf{v}	velocity
$\mathbf{v}_1, \mathbf{v}_2$	vertex vectors 1 and 2
$ Y(f) $	absolute value of an amplitude
y	distance
α	volume fraction
γ	specific heat
λ_c	critical wavelength
λ_m	predominant wavelength
ρ_s	density of steam
ρ_w	density of water
σ	surface tension

Acronyms

BCO	bubbling condensation oscillation mode
BWR	boiling water reactor
CFD	computational fluid dynamics
CO	condensation oscillation mode
DCC	direct contact condensation
EPR	European pressurized water reactor
FFT	fast Fourier transform
FVM	finite volume method
LWR	light water reactor
LOCA	loss-of-coolant accident
NPP	nuclear power plant
PACTEL	parallel channel test loop
PC	polycarbonate
PIV	particle image velocimetry
px	pixel
RTI	Rayleigh-Taylor instability
SEF-POOL	separate effect facility
SRV	safety/relief valve
TIFF	tagged image file format
WMS	wire-mesh sensor

CHAPTER 1

Introduction

Nuclear power is one of the lowest emitters of greenhouse gases available to generate electricity [1]. A total of 447 operable nuclear reactors produced over 10% of the world's electricity in 2017 [2]. As carbon dioxide free energy solutions have a major role in the fight against global warming, the reliability and safety issues of power production techniques become more important.

Commercial nuclear reactors can be classified in several ways (by coolant, by moderator or by generation). All reactor types have their own specific safety issues which have to be taken into account, but they all have the same goal to produce electricity for human needs and avoid the discharge of radioactive material. The radioactivity of the reactor fuel sets strict requirements for the safety systems of the nuclear power plant (NPP). In order to design NPPs so that they can be considered safe, dominant physical phenomena must be adequately understood in all operating conditions. Building upon such understanding, design principles such as defence-in-depth can be implemented, providing confidence that individual equipment failures or human errors do not lead to unacceptable consequences. Although NPPs are among the safest and most secure facilities in the world [3], it is desirable to limit their negative impacts to the practical minimum. Therefore, research is needed to properly understand the physical phenomena that occur during accidents. A sufficient command of the phenomena enables the design and assessment of NPP safety features.

In Lappeenranta, safety research on NPP started in the early 1970s, concentrating mostly on local reactor types: VVER-440 (Loviisa 1 & 2), the Nordic type BWR (Olkiluoto 1 & 2), and European pressurized water reactor (EPR) (Olkiluoto 3). The latest research subject has been VVER-1200 (Hanhikivi 1). LUT University has a wide variety of large scale integrated and separate effect test facilities for thermal hydraulics research of light water reactors (LWRs). For modelling and simulations, system codes, computational fluid dynamics (CFD) and Monte Carlo methods have been used.

One large research area has been Nordic type BWR suppression pool and its per-

formance as a safety device. The BWR containment is small but the volume of water acting as heat absorber is large, and the capability of the water mass to effectively limit containment pressurisation is of interest. Also the stability of the heat absorption and absence of rapid dynamic loads on structures needs to be proven.

The main causes of these structural loads are condensation oscillations and chugging, which have been studied for decades. Test facilities – large [4–7] and small [8–12] – have been used to study these condensation modes.

Dozens of BWR suppression pool experiments have been carried out in the last decades in Lappeenranta [13]. Several large-scale integral test facilities, such as POOLEX and PPOOLEX, have been used to study pool stratification and mixing as well as direct contact condensation (DCC). For more detailed research of these phenomena smaller facilities, such as separate effect facility (SEF-POOL) have been used.

The safety analysis of NPPs relies on computer codes, which need to be validated to be considered as sufficiently reliable for safety analyses. As the computer calculation capacity has increased significantly during the past decades, CFD has become an important part of the modelling of experiments.

One area of model validation based on thermal hydraulics experiments is turbulence, which plays a role in determining the structure of the interface and efficiency of heat transport from the interface deeper into the fluid. Turbulence and interfacial area transport modelling on the pool scale is still semiempirical, which is why modern measuring techniques such as high-speed cameras, particle image velocimetry (PIV), and wire-mesh sensors (WMSs) are gaining ground among more traditional equipment, such as thermocouples and pressure transducers. Traditional data is limited to point values, which do not provide information about key phenomena such as interphase transfers. The physical models (closure laws) in numerical codes are largely empirical and have complex connections to each other. This often limits the code validation process to an integral level, at which the overall behaviour of a model set is compared to experiments instead of validating separately each closure law. Recent advances in high-speed photography enable more detailed interface characterisation; thereby, physics modelling for interfaces can be improved also in computer codes.

As the amount of measuring equipment has increased, accurate design of experiments has become more important. Using experimental facilities, which have power of 1 MW or larger, is expensive. Consequently, optimization of the experiments can reduce costs significantly.

The usefulness of video cameras in the experiments was recognized already in the early 1980s [14] when movie cameras were used to record experiments. Unfortu-

nately, at that time recorded data was hardly ever reported. At LUT University, the need for high-speed video recordings was recognized in 2007 [15]. In the first experiments, normal speed (25 fps) cameras were used, more or less for qualitative analyses. Later on, high-speed cameras came to support other measuring techniques.

The increasing amount of recorded data created a problem, as the semi-automatic observation of the video material was no longer effective. The first pattern recognition algorithm for the detection of steam bubbles in POOLEX tests was created in 2012 [16, 17]. The algorithm was improved in 2013 by the author [18]. These algorithms were made for normal speed cameras. The new high-speed camera system created the need for a new algorithm which could estimate the volume and surface area of condensing steam bubbles better than before, collect more data, and increase knowledge of the optical measuring techniques.

1.1 Objective of the study

The aim of this study was to create pattern recognition based image analysis algorithms to automatically process a large set of frames containing dynamic data for vertical vent pipes and horizontal spargers. The algorithms are used to improve the design of thermal hydraulics experiments and the validation of the models for the rapid condensation of various CFD codes.

1.2 Research approach

Data was obtained from the direct contact condensation experiment DCC-05 of the PPOOLEX test facility and from the SEF-INF2 experiment of the SEF-POOL facility. The particular tests described in Chapter 3 were chosen because of their best possible video quality available and interesting condensation modes. The image processing toolbox of the MATLAB software was used for creating an image analysis algorithm for vertical vent blowdown pipes. The algorithm evaluates the basic properties of condensing steam bubbles, such as volume, surface area, surface velocity and acceleration in the vertical direction. Publication I presents the development process of the algorithm.

The algorithm was used for the frequency analysis of the DCC-05 experiments data. In the frequency analysis, the fast Fourier transform (FFT) was used to study different frequencies of several bubble types. Frequency analysis is presented in Publication II.

The data analysed with the algorithm could determine the critical wavelength of condensation driven Rayleigh-Taylor instability (RTI). This characterisation of

the small interface deformations must also be taken into consideration when generating the grid size for a CFD simulation. Frequency analysis results were also compared to the CFD data. The algorithm developed to analyse experimental data was also applied to give input to CFD application and to compare results of the CFD simulations to data. This is presented in Publication III.

The algorithm was extended to cover steam injection from a horizontal sparger orifice. Here the challenge was to characterise multiple moving bubbles. Improvements for pre-processing, pattern recognition and image analysis was made as well as evaluation of the surface velocities and accelerations were calculated for all angles between 0° to 360° of projected 2D plane instead of vertical direction. This thesis successfully improves the algorithm such that it can track multiple bubbles and process their respective data. Development of the extended algorithm is presented in Publication IV.

1.3 Dissertation structure

The dissertation is divided into five chapters. Chapter 1 presents a brief overview to research area and environment. Chapter 2 contains a closer view to the background of the research. Chapter 3 presents the research process from the design of the algorithm to the data analysis. Results have been discussed in Chapter 4 and shortly concluded in Chapter 5. The related articles Publication I – Publication IV are presented after the References.

CHAPTER 2

Background

2.1 Nordic type boiling water reactor suppression pool system and its effects

Nothing lasts forever, but the safety systems of an NPP should last through the operation lifetime until the decommissioning of the power plant. Out of the 447 operable power plant reactors worldwide, 73 are BWRs [2]. Most of them are over 35 years old such as the Olkiluoto NPPs Nordic type BWRs, Olkiluoto 1 & 2 (OL1 & OL2). Owing to reactor ageing, more attention should be paid to their reliability and the possible safety issues of the NPP.

All operating BWRs use pressure suppression containments [19]. The main part of the pressure suppression system is a wetwell, a water filled suppression pool (condensation pool) whose major function is to protect the environment from an uncontrolled release of radioactive fission products by condensating released steam to the pool water.

Nordic type BWRs are Asea-Atom (later on ABB) supplied BWRs (e.g. BWR 69, BWR 75, BWR 90, and BWR 90+) [20]. Figure 2.1 displays a schematic view of a Nordic type BWR containment building.

As Fig. 2.1 shows, the volumetric size of a nitrogen filled containment building of the BWR is fairly small. The compact size is an advantage during the construction of the power plant, but requires the capability to prevent overpressurization if the energy in the reactor is discharged into the containment.

Pressure suppression capability is needed during the operation of the safety / relief valves (SRVs) in operating transients or other additional steam releases to control reactor pressure [19]. It is also needed in the case of postulated accidents like pipe breaks (loss-of-coolant accident (LOCA)).

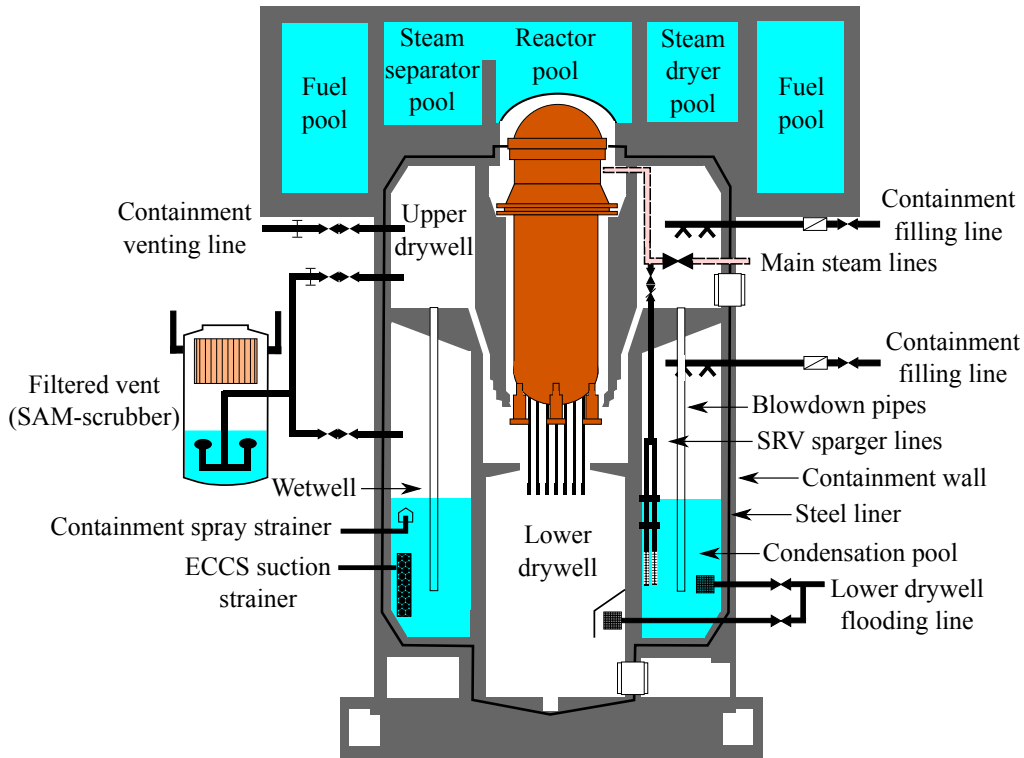


Figure 2.1: Nordic type BWR containment [21].

In a pipe rupture, a large amount of steam is released to the drywell, the primary barrier of the containment. Due to the steam release, the pressure of the drywell increases rapidly. Drywell air and steam are discharged through a vent pipe system to the wetwell. In Nordic type BWRs, the vent pipes are vertical. Pressure suppression takes the steam and condenses it rapidly into pool water.

The released steam causes dynamic short-term loads on the pressure suppression system. These loads demand a great deal of suppression pool strength. Five different dynamic phenomena are associated with these short-term loads, including SRV/vent pipe air clearing, pool swell, condensation oscillations, chugging, and high-temperature condensation instabilities. [19].

2.1.1 Direct contact condensation of steam injected into water

Condensation is the removal of heat from a system so that a part or all of the vapour phase is converted into liquid [22–24]. Several different condensation modes exist: film condensation of vapour/steam on the cold surface of a solid, dropwise condensation on a cold surface, homogeneous condensation resulting from the change in pressure, and DCC. DCC occurs when subcooled liquid (water) comes into contact with vapour (steam). DCC can be divided into three cases: DCC on the vapour of liquid jets, DCC of vapour on a liquid surface, and DCC of vapour injected into a pool of liquid, [25]. This research concentrates on the last case.

DCC acts similarly, when steam is pushed through either horizontal or vertical pipes [16]. When steam is injected into the water of a suppression pool, it can be divided into four regions: steam plume, outer interface of the plume, hot water layer, and bulk water. Steam plume consists of pure steam. Condensation takes place at the outer interface of the plume. Hot water layer collects the outer interface surrounded by bulk water.

DCC is mainly controlled by the liquid side convection and conduction near the bubble surface. Convective heat transfer is controlled by flow motion carrying away the heat, the interfacial area available for the heat transfer, the temperature difference, and fluid properties.

Depending on the steam mass flux G and the temperature of the pool water T , different DCC modes appear. These modes include actually the earlier mentioned instabilities, which may cause short-term loads on the suppression pool. This research concentrates on condensation oscillation and chugging modes.

Condensation oscillations occur during an early discharge of the steam, when the unsteady condensation induces interface oscillations and subsequent accelerations of the bulk water which creates unsteady loads on submerged structures. Bubbling condensation oscillations may occur also if the pool water temperature increases locally. Chugging occurs when the steam mass flux is relatively low [19, 26]. The increased pressure of the steam pushes the steam/water interface out of the end of the vent pipe. The expansion increases the surface area and turbulent mixing at the close neighbourhood of the bubble, which increases the condensation rate. An increased condensation rate reduces the steam pressure and interface collapses back into the vent pipe before growing back.

2.2 Modelling of direct contact condensation

As mentioned before in the Chapter 1, the analysis of the experiments need reliable computer codes which are validated. Advances in high-speed photography

enable more detailed interface characterization, and with a suitable automatic image analysis algorithm, comparison between image analysis and simulations offers an evaluation of initial parameters and boundary conditions for code validation.

2.2.1 CFD modelling of direct contact condensation

Current state-of-the-art two-phase CFD codes allow practical modelling of suppression pool behaviour. However, suppression pool operating conditions involve high level of turbulence and initially the deep subcooling of liquid [16]. In such conditions, DCC has proven difficult to calculate correctly [21].

The most commonly used CFD solvers for two-phase flows are based on the finite volume method (FVM) [27], in which the needed spatial resolution for describing the observed physical behaviour defines the needed discretization (i.e. grid size and time step). The selection of the adequate closure models depends on the discretization. High resolution transient simulation approach leads easily to enormous computational costs.

CFD can address the convection modelling in terms of characteristic velocity and length scales of turbulence near the bubble surface if the turbulence model and the heat transfer models for DCC are properly chosen. The local interfacial area in terms of interfacial area density a_i can be solved in a two-fluid CFD solver by calculating the gradient of volume fraction and using additional models to take into account the effects of lacking spatial resolution [21].

The CFD modelling of an oscillating bubble, even with a low resolution, is time-consuming due to the transient nature of the flow which imposes short time steps. Therefore, even coarser methods have been introduced to make facility scale simulations possible [28]. In such lumped parameter simulations or very coarse scale CFD simulations, the two-fluid solution of a condensing bubble is avoided and replaced with corresponding source terms for momentum and energy. Figure 2.2 illustrates the role of data obtainable from image analysis in the numerical modelling of condensing bubbles.

In the Fig. 2.2 the two-headed arrow refers to values usable for validation/comparison between the image analysis and simulation. The one directional arrow refers to an initial value, parameter, or boundary condition needed for the numerical simulation model obtainable from image analysis. \mathbf{a} is the surface acceleration, \mathbf{v} is the surface velocity, f is frequency, α is the volume fraction, λ_c is the critical wavelength, S_M is the momentum source and S_H is the heat source.

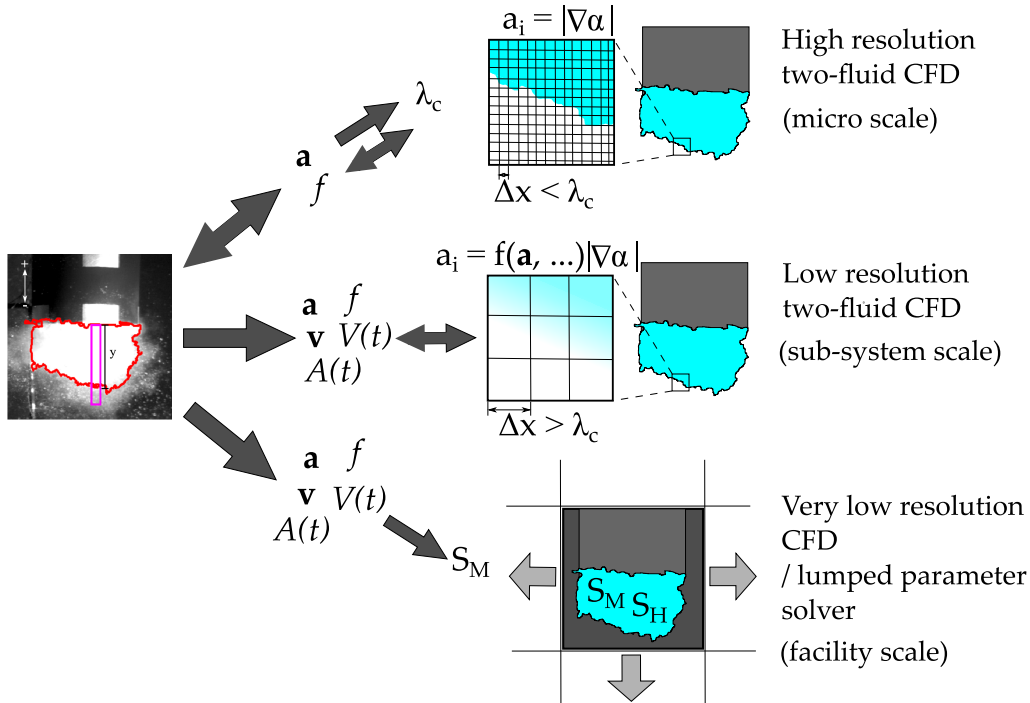


Figure 2.2: Validation data from image analysis for different scale numerical DCC models.

2.2.2 Image processing and analysis of direct contact condensation experiments

Image processing is a subcategory of signal processing, where the original image is modified in such a way that the transformed output image improves and suits the original function better. In other words, in image processing the outcome is also an image, whereas in image analysis the original image (often pre-processed using image processing) is transformed to different readable data such as labelling of the image objects or basic properties of recognized objects.

When designing an image analysis algorithm, two possibilities exist: the development of the algorithm, which is designed for the test facility used in the experiments, or using a facility which is designed for the algorithm. The construction of a test facility designed for algorithm development is not always possible.

When recording complex thermal hydraulics experiments, several different errors may occur. The camera itself produces errors due to geometric optics, although digital cameras can take most aberrations into account. The position of the camera might change from time to time, it can be tilted or at an angle. The

shooting angle might be poor at the beginning, when drilling extra windows is not possible due to pressure system regulations, or when the extra windows might decrease heat exchange in the system which may affect the other measurements. Some light sources produce disturbances in the video, and lighting may change during the mixing of the water. Important test equipment, such as pressure transducers, may cause problems in the pre-processing of the video material, and so on. Finally, the possibility of human error should be remembered.

2.2.3 Facility designed for algorithm development purposes

To test the effect of a physical quantity, constant conditions are created. Other quantities are kept constant while the quantity of interest is changed. A similar approach also works for film shooting. If the main goal is to design an algorithm for specific initial data such as recorded video material, the best way to test the algorithm is to create a test facility, specially developed for algorithm development purposes.

The use of such a test facility enables estimating the number of errors from different sources described above. The test algorithm of a separate facility should be simple due to a lack of pre-processing. Error estimation, which does not include any obtrusive objects, for a separate test facility should show only the errors of the simple algorithm.

In research on DCC phenomena, a possible test facility could be a simple, transparent, water filled box with even lighting and a solid background with strictly desired size range of bubbles. The bubble production method is not important if the experiments are recorded with high quality, because the algorithm does not see a difference between air and steam bubbles. The test facility should have stable, removable mounting system for a high-speed video camera, which allows reshooting identical video material even if the camera is removed and reinserted from time to time.

This kind of facility allows to test different camera conditions such as white balance, apertures, and objectives. When the basic features of the camera are known in different situations, moving towards larger, and more complex test facilities would be easier than rushing straight to large-scale integrated test facilities.

CHAPTER 3

Review of the Results

The aim of this study was to create an algorithm for evaluating large steam bubble properties in integrated test facility experiments using pattern recognition and image analysis methods. The work started with a normal speed camera in an open POOLEX test facility by Tanskanen [16] and continued in a PPOOLEX test facility by the author [18]. The original goal was to create an algorithm for vertical vent blowdown pipe cases to improve knowledge of the effects of DCC in suppression pools. The PPOOLEX DCC-05 experiment was used as a reference for vertical steam blowdown in this study. Then, the algorithm was extended to cover injection from a horizontal sparger orifice, in which a separate SEF-POOL SEF-INF2 experiment was used. This chapter reviews the development of the algorithms and the main results. It also briefly describes the test facilities and experiments.

3.1 Algorithm for vertical vent pipes

3.1.1 PPOOLEX test facility and DCC-05 experiment

The integrated PPOOLEX test facility is a volumetrically scaled (ratio approximately 1:320) thermal hydraulics model of a Nordic-type BWR suppression pool. The main component of the facility is a cylindrical stainless steel vessel, which consists of two parts: a wetwell compartment (suppression pool) and a drywell compartment. An intermediate floor separates the compartments. A vessel also has an inlet plenum and air/steam line piping. A vertical vent pipe is attached non-axisymmetrically underneath the floor to prevent undesirably strong symmetrical reflection of a pressure wave in this cylindrical pool. Depending on the needs of the experiment, the blowdown pipe geometry can be changed. The steam needed in the experiments is produced by steam generators of the parallel channel test loop (PACTEL) facility, which has a heating power of 1 MW at the core section. Figure 3.1 shows the assembly of the PPOOLEX test facility and Table 3.1 lists the main dimensions of the test facility compared to the conditions in

the Olkiluoto power plant.

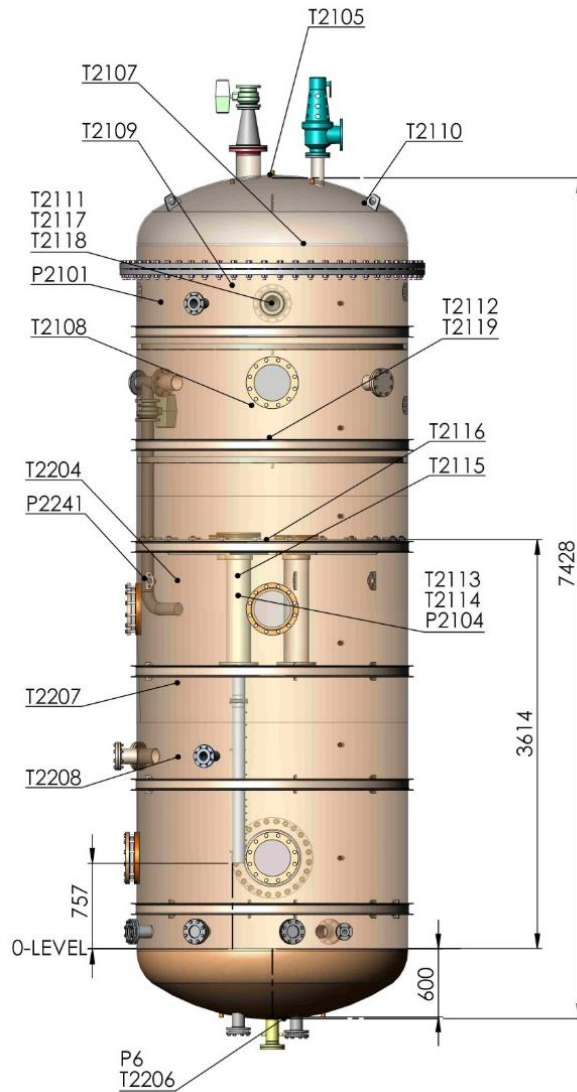


Figure 3.1: PPOOLEX test vessel and locations of some process measurements.

Table 3.1: Comparison between PPOOLEX test facility and the suppression pools of Olkiluoto 1 and 2.

	PPOOLEX test facility	Olkiluoto 1 & 2
Number of blowdown pipes	2	16
Inner diameter of the blowdown pipe [mm]	109.3 [†]	600
Suppression pool cross-sectional area [m ²]	4.45	287.5
Drywell volume [m ³]	13.3	4350
Wetwell compartment [m ³]	17.8	5725
Nominal water volume in the suppression pool [m ³]	8.38 [‡]	2700
Nominal water level in the suppression pool [m]	2.14 [‡]	9.5
Pipes submerged [m]	1.05 [‡]	6.5
$A_{\text{pipes}}/A_{\text{pool}} \times 100\%$	0.8/1.6 [*]	1.6

[†] with DN100 pipe

[‡] can be chosen according to the experiment type in question. The values listed in the table are based on the ratio of normal water and gas volumes in the plant.

^{*} with one / two blowdown pipes

The facility can be used to model various thermal hydraulics phenomena, such as steam bubble condensation and gas bubble propagation in suppression pools, structural loads caused by rapid condensation, and the effect of non-condensable gases on emergency core cooling strainer behaviour.

The experiments are recorded using three similar, almost perpendicularly mounted Phantom Miro high-speed video cameras: one at the bottom of the pool and two side cameras behind the side windows of the vessel. The experiments are lighted with one halogen lamp through another side window. Due to restricted number of windows in the pressurized vessel, the adjustment of the lighting or positions of the cameras are limited. A more detailed description of the PPOOLEX test facility is presented in [13].

The main purpose of the PPOOLEX test DCC-05 was to obtain measurement data for the validation of the DCC models used in the CFD modelling of the chugging condensation mode and to make a high-speed video recording for the development of an image processing and pattern recognition algorithm [18, 29]. The pool water temperature rise was kept as low as possible in the DCC-05 test in order to study only the effect of the variable steam flow rates. To achieve this goal the steam flow rate was quickly adjusted to the new value for the recorded periods, but while data was being transferred from the camera, it was reduced near zero to prevent the unnecessary heat-up of pool water.

Before the experiment, the wetwell pool was filled with water at 298 K so that the blowdown pipe outlet was submerged by 1.05 m and the drywell was filled with air at atmospheric pressure. A DN100 (outer diameter $d = 114.3$ mm) stainless steel blowdown pipe was used in the experiment. The experiment was started

with a clearing phase during which the structures were heated with a high steam flow rate to prevent wall condensation and to remove non-condensable air. The pool temperature rose to 303 K during this process [29].

The valid part of the experiment following the clearing phase consisted of six runs with increasing flow rates between 75 g s^{-1} and 200 g s^{-1} . The pool temperature rose gradually to 313 K during these blows. The individual steam blows of the DCC-05 experiment defined by the steam mass flux and pool bulk temperature are within region 2 of the condensation mode map by Lahey and Moody [19], presented in Fig. 3.2.

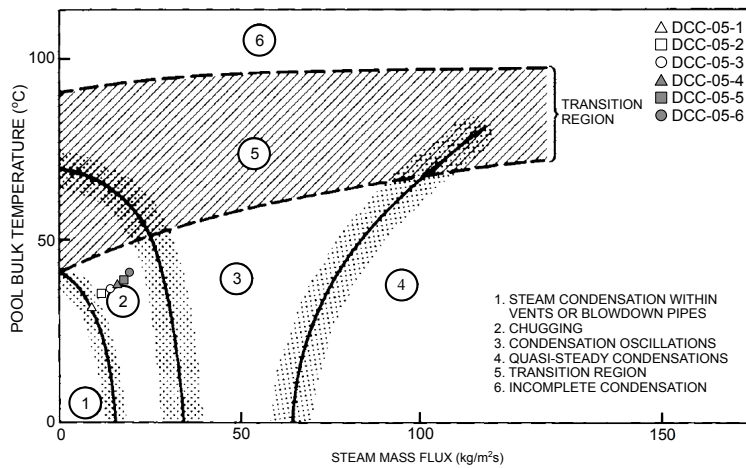


Figure 3.2: Regime map of Lahey & Moody [19]. Schematic view of typical regions for condensation modes during SRV or LOCA blowdown.

The DCC-05 test consisted of six recorded runs with different flow rates, named DCC-05-1...DCC-05-6, with a total length of 52 min. Six 48 s grayscale videos were recorded (one for each runs DCC-05-1...DCC-05-6) with a frame rate of 300 fps. The fourth video, named DCC-05-4, was chosen for this study. Steam flow rate of the DCC-05-4 test was 140 g s^{-1} which approximately corresponds to steam mass flux of $15 \text{ kg m}^{-2} \text{ s}^{-1}$. The resolution (in pixel (px)) of the each video was $768 \text{ px} \times 768 \text{ px}$. The lens focal length was 24 mm and the lens aperture f2.4. The original video format was RGB Cine which was converted to a jpg image sequence with Phantom Camera Control PCC 2.1 software [30]. Before the experiment, a short video of an empty background was taken for image processing purposes.

3.1.2 Development of the algorithm

The algorithm consists of three parts: pre-processing, where all image processing is performed, a simplified pattern recognition part, where the edges of steam bubbles have been detected, and a post-processing part, where all image analysis and data collection takes place. Parallel processing of frames is recommended as the frame count is high. Figure 3.3 presents a simplified flow chart of the algorithm.

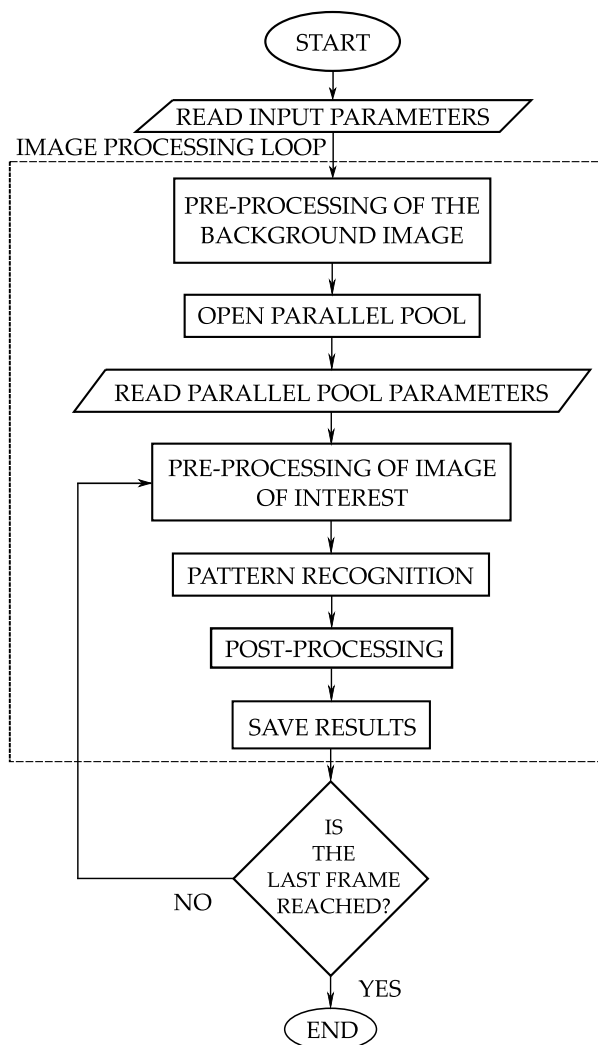


Figure 3.3: Simplified flow chart of the image analysis algorithm for vertical vent pipes.

MATLAB software [31] was used in the development of the algorithm. The algorithm begins by loading the grayscale images and a set of parameters such as the original size of the images. Image processing started from the background image. Some filtering was done to blur obtrusive objects. The idea was to remove an empty background image from each frame, when only the changes in the frames should remain. Steam bubble image data obtained from a large scale facility inevitably contains noise due to local overexposure, shadowing, and extraneous objects such as small bubble swarms. Necessary measuring equipment might also hamper the image analysis. These are the downsides of the large scale integrated test facilities compared to test facilities made only for algorithm development purposes.

Due to these additional objects (see Fig. 3.4), some image processing was carried out for every frame. Image filtering was used to adjust the contrast and brightness in different parts of the image. Overexposed spots were darkened, shadowed bubble sides brightened and disturbing objects blurred, removed or filled otherwise. After the pre-processing of the frames, the background image was subtracted from all frames of the video.

The simplified pattern recognition part of the algorithm uses methods based on unsupervised pattern recognition and gave the name for the algorithm in the original publications. Thresholding by Otsu's method was used as a technique of image segmentation when distinguishing pixels of the bubbles from pixels of the background [32]. Otsu's method performs clustering-based image thresholding, or converts grayscale images to a binary images. The method considers that the image contains two classes of pixels: foreground pixels and background pixels using a bi-model histogram and enumerates the optimum threshold [32, 33]. As a result of this labelling the frames were converted to binary images which contained only white bubble pixels and black background pixels. The edge of the bubble was detected from the binary images by implementing the Moore neighbourhood algorithm, modified by Jacob's stopping criteria [34], which is presented in Fig. 3.5.

In the Moore neighbourhood algorithm, tracing of the boundaries starts from the first column, which contains boundary pixel x (see Fig. 3.5 A). Searching starts clockwise from the bottom neighbour pixel and stops when another boundary pixel is found (Fig. 3.5 B). Now this new boundary pixel becomes the current pixel x . The first new boundary pixel was found from the upper right corner of the starting point. The new trace starts in the direction from which the previous trace came (Fig. 3.5 C). In Jacob's stopping criteria, the algorithm terminates when it visits the start pixel for a second time from the same direction it did the first time around (Fig. 3.5 E).

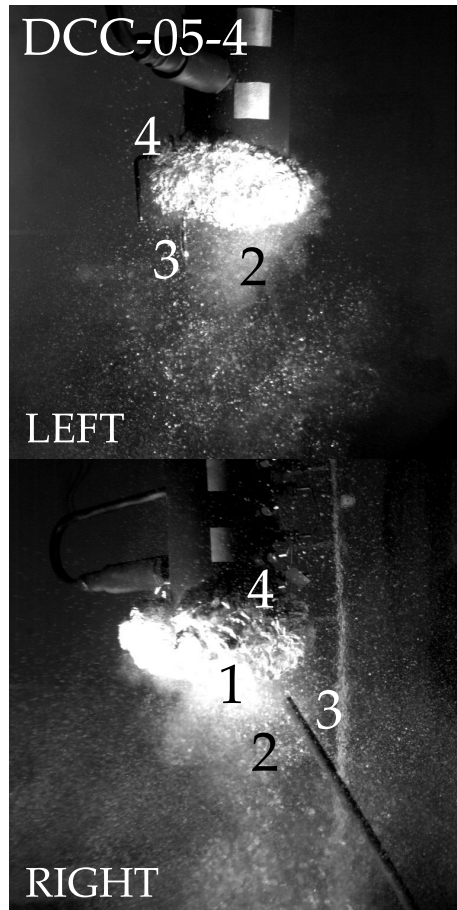


Figure 3.4: Obtrusive objects and structures are common in integrated test facility experiments. (1) overexposed areas, (2) swarm of small bubbles, (3) interfering structures, and (4) shadows.

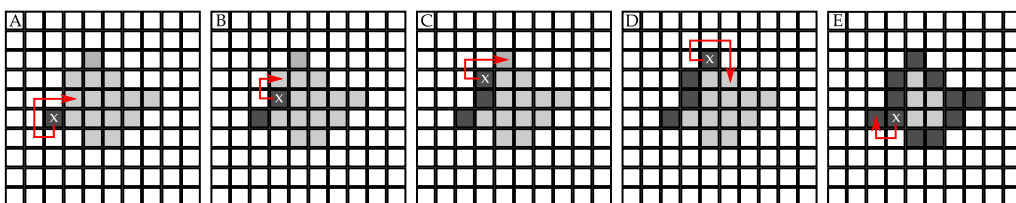


Figure 3.5: Operation of the Moore neighbourhood method. The Moore neighbourhood of a pixel x is the set of 8 pixels which share a vertex or edge with the pixel x .

As a result, the edge detection gives three output arguments: the row and column coordinates of the boundary pixels, the label matrix and the number of objects found. When the bubble recognition was finished, the post-processing (image analysis) started.

DCC-05 was recorded using three cameras: one at the bottom of the pool and two side cameras. As the bottom camera showed that bubbles were approximately axisymmetric during the DCC-05 experiment and the right camera video was noticed to be of poor quality, only the left camera video was used.

The maximum diameters of the bubbles were estimated from the side profiles of the bubbles. When only the side profiles of the bubbles were available some approximation was needed in the estimation of the surface area and volume of the bubbles. The side profiles of the bubbles were known to be of an arbitrary shape, e.g. flat, round or semi-circular. The voxel-based method has been used successfully to evaluate the surface area of brain images [35], and brains are known to have complicated shapes. Thus this method was selected for the evaluation of the bubbles. Figure 3.6 shows a simplified principle of the evaluation of the bubble volume.

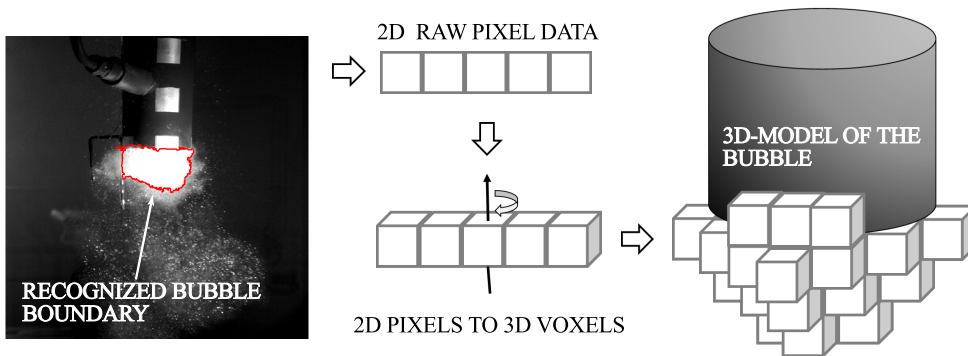


Figure 3.6: Simplified principle of the development of a 3D model of a bubble [36].

Binary images were processed row by row. The recognized bubbles consisted only of white (nonzero) pixels. From each frame, the number of nonzero pixels was calculated and the centre of mass of each pixel row evaluated. Each white pixel row was rotated around a vertical axis that passes through its centre of mass, which produced a cylindrical plate. The sum of the volumes of the cylindrical plates gives the volume V of the bubble in voxels:

$$V = \sum_{i=\text{first row}}^{\text{last row}} \pi \left(\frac{d_i}{2} \right)^2 h_i, \quad (3.1)$$

where d_i is the number of nonzero elements in the i^{th} row, and h_i is the height of the row.

The surface of a bubble was created using an isosurface function which extracts isosurface data – faces F and vertices V – in separate arrays from the volume data. From vertex array V , triangle vertices r_1, r_2 and r_3 were created. The vectors between vertices were named \mathbf{v}_1 and \mathbf{v}_2 . Vectors \mathbf{v}_1 and \mathbf{v}_2 delimited the parallelogram as Fig. 3.7 shows.

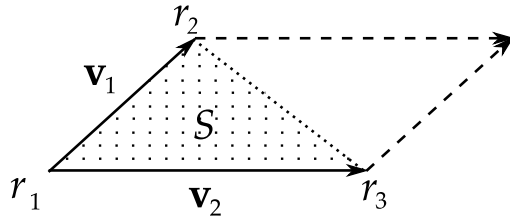


Figure 3.7: Calculation of the surface area. Triangle vertices r_1, r_2 and r_3 . Vectors \mathbf{v}_1 and \mathbf{v}_2 define the parallelogram. The patch S (dotted area) is an area of a triangle defined by the vectors, which is half of the area of the parallelogram [36].

The surface area A of the bubbles can be calculated using these parallelograms as follows:

$$A = \sum_{i=1}^S (S_{i-1} + 0.5 \cdot |\mathbf{v}_{1,i} \times \mathbf{v}_{2,i}|), \quad (3.2)$$

where S_{i-1} is the area of each patch (half of the area of the parallelogram) and $S_0 = 0$. Publication I presents a validation sphere with radius of $r = 10$ pixels constructed using voxels and cylindrical plates with and without a smooth isosurface.

In vertical vent pipes, the bubbles hardly ever detached from the mouth of the pipe. More frequently the bubbles reached only approximately $0.5 d_{\text{pipe}}$ from the outlet. For this reason, only vertical velocity and acceleration were evaluated. They were estimated using the box ratio method [18], where only a thin region of interest is measured as Fig. 3.8 shows. A rectangle of a width of 35 pixels (≈ 2.78 cm) and a height of 344 pixels (≈ 27.3 cm) was placed in the middle of the blowdown pipe outlet with its upper border at the outlet of the pipe. The change in the average lower border of the bubbles was investigated in this rectangle and the average fluctuation of the bubbles was recorded from that.

The vertical velocity \mathbf{v}_n and acceleration \mathbf{a}_n of the bubble were evaluated using forward difference as presented in Equations (3.3) and (3.4), respectively.

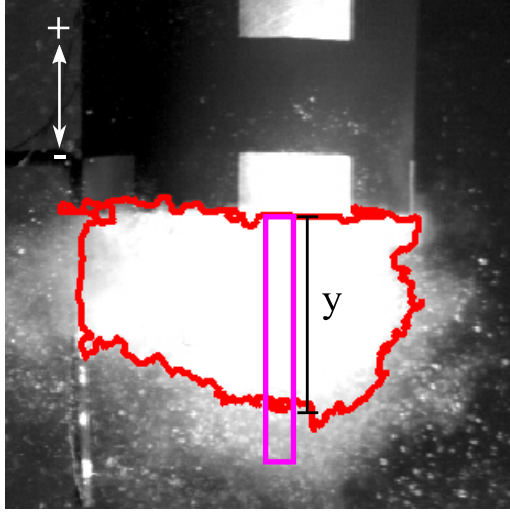


Figure 3.8: Evaluation of the y -distance for velocity and acceleration calculations. The magenta rectangle represents the ratio box (not to scale). In every image n , the average of the y distance inside the rectangle was calculated and velocity \mathbf{v}_n and acceleration \mathbf{a}_n evaluated using a forward difference method [37].

$$\mathbf{v}_n = \begin{cases} F_s (-y_{n+1} - (-y_n)), & \text{when } n = 1 \\ \frac{F_s}{2} (-y_{n+1} - (-y_{n-1})), & \text{when } 2 \leq n \leq N \end{cases} \quad (3.3)$$

and

$$\mathbf{a}_n = \begin{cases} F_s^2 (-y_{n+2} - 2(-y_{n+1}) + (-y_n)), & \text{when } n = 1 \\ F_s^2 (-y_{n+1} - 2(-y_n) + (-y_{n-1})), & \text{when } 2 \leq n \leq N' \end{cases} \quad (3.4)$$

where N is the total number of images in the video material, and n is the image of interest at frame rate F_s .

3.1.3 Estimated error of the algorithm

In this study, building a component system specially for algorithm development purposes was not possible. Therefore, it is useful to separate errors stemming from a large scale integrated test facility and errors stemming from the design of the algorithm.

The algorithm is tailored for the large scale test facility which is used in complex thermal hydraulics experiments of BWR suppression pool systems. The vessel is pressurized and contains multiple measuring devices inside the vessel which cannot be removed from the image area. These circumstances create limitations which need to be recognized and bypassed one way or another. However, these

are also errors which are usually accidentally forgotten. Errors stemming from the test facility in this study include, for example, limitations in camera positioning and lighting, which created challenges presented in Fig. 3.4. These are, nevertheless, errors which can be reduced if taken into account in the design of new test facilities.

More emphasis should be put on the errors based on the design of the algorithm. The basic principle of the development process was to use built-in functions of MATLAB as much as possible to make the algorithm understandable for persons unfamiliar with programming. This makes the algorithm easier to access and lowers the threshold to use it.

The selection of the pre-processing functions may vary depending on the test facility. Also a different edge detection method could be used. The Von Neumann neighbourhood could use less computer capacity in edge detection and would work well for objects with rectangle features, but with arbitrarily shaped bubbles, the Moore neighbourhood method is more convenient. The Von Neumann neighbourhood method uses only four neighbour pixels (at top, bottom, left and right), whereas the Moore neighbourhood method uses all eight neighbour pixels. Edge detection also generates an error when detecting arbitrary objects such as bubbles when the threshold value is close to the foreground threshold limit in Otsu's method. These errors are related closely to the facility limitations.

The algorithm underestimates the volume and surface area of the bubble, regardless of the evaluation method. The algorithm is based on the evaluation of the side profile of the bubble and does not benefit from the topography information of the surface of the bubble. Partly due to the lighting conditions, the surface area is thus highly underestimated. The lighting overexposes the bubbles, making them solid white. A real steam bubble reminds a cauliflower, and its surface has creases and becomes much larger than the surface area of a solid smooth balloon.

As an important mitigating factor, the recognition of transient events in suppression pools is often more important than knowledge of the exact size of a bubble in a video frame. Thus, even if certain volumetric errors prevail in the result, relative errors between two frames remain small.

Since the algorithm is not context-dependent, errors were estimated by comparing synthetic bubbles with different radii to theoretical values of bubble volumes and surface areas. Figure 3.9 presents the relative error of bubble volumes and surface areas.

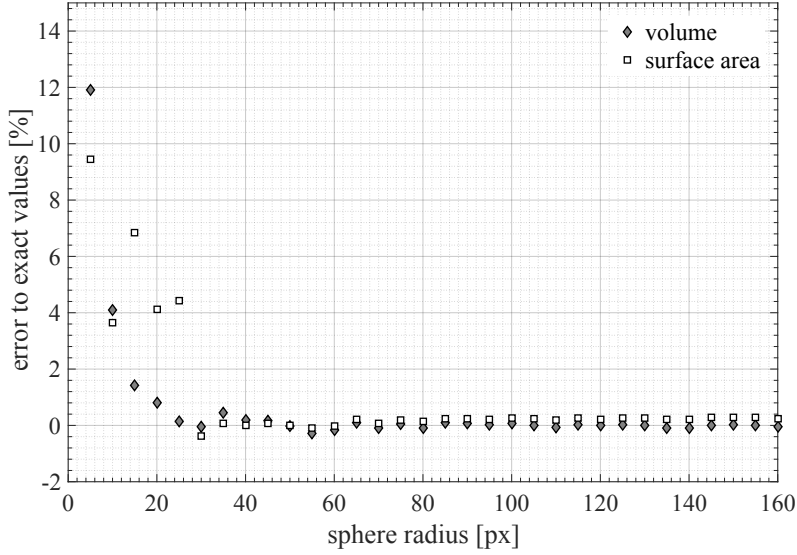


Figure 3.9: Volume and surface area errors of hypothetical spheres, produced using the algorithm for circles with different radii r , compared to exact values of theoretical spheres, $A_{\text{sphere}} = 4\pi r^2$ and $V_{\text{sphere}} = \frac{4}{3}\pi r^3$ [37].

The feasibility and the estimated error of the algorithm have been calculated as follows. Equation (3.5) integrates the volume of the bubble using cylinder plates. Radius r_i of the cylinder is calculated in pixels d and converted to metric units by using the factor M_i , which is the size of one pixel in metric units. Using the radius of the cylinder, the total volume of the bubble is

$$V = \sum_{i=1}^N \pi r_i^2 h_i, \quad (3.5)$$

where N is the number of cylinders, and r_i and h_i are the radius and height of the cylinders i , respectively. Height is always one pixel ($h_i = d$), and the radius is a pixel multiplied by M_i ($r_i = M_i d$):

$$V = \sum_{i=1}^N \pi (M_i d)^2 d = \pi d^3 \sum_{i=1}^N M_i^2. \quad (3.6)$$

The uncertainty of N is assumed to be zero. The error estimation for the volume

V using total differential is:

$$\begin{aligned} \left| \frac{\Delta V}{V} \right| &\leq \frac{1}{V} \left(\left| \frac{\partial V}{\partial d} \right| |\Delta d| + \sum_{i=1}^N \left| \frac{\partial V}{\partial M_i} \right| |\Delta M_i| \right) \\ \frac{\Delta V}{V} &\leq \frac{1}{\pi d^3 \sum_{i=1}^N M_i^2} \left(3\pi d^2 \Delta d \sum_{i=1}^N M_i^2 + 2\pi d^3 \sum_{i=1}^N M_i \Delta M_i \right) \\ \frac{\Delta V}{V} &\leq \frac{3\Delta d}{d} + \frac{2 \sum_{i=1}^N M_i \Delta M_i}{\sum_{i=1}^N M_i^2}. \end{aligned}$$

The uncertainty of the M_i is assumed to be constant $\Delta M_i = \Delta M$, thus

$$\frac{\Delta V}{V} \leq \frac{3\Delta d}{d} + \frac{2\Delta M \sum_{i=1}^N M_i}{\sum_{i=1}^N M_i^2}. \quad (3.7)$$

3.1.4 Evaluation of the basic properties of large steam bubbles

In the DCC-05-4 experiment, a total of 14426 frames were stored. Figure 3.10 presents the evaluated surface area and volume changes of the bubbles during the experiment.

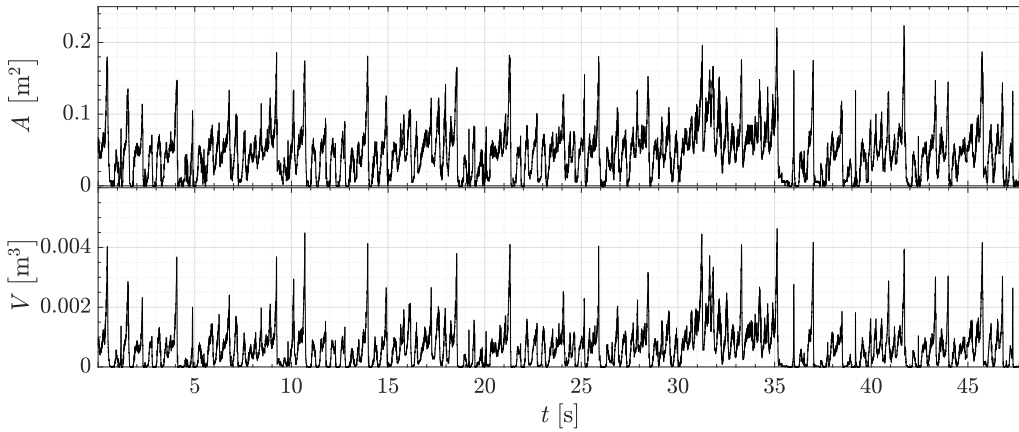


Figure 3.10: Estimated surface areas A (top) and volumes V (bottom) of the bubbles during the DCC-05-4 experiment.

The estimated surface area varies from 0.05 m^2 to 0.20 m^2 . The volumes of the largest bubbles are near 0.004 m^3 . Figure 3.11 shows the distance between the surface of the bubble and the blowdown pipe outlet in the vertical direction, the estimated velocity and the vertical acceleration of the bubbles.

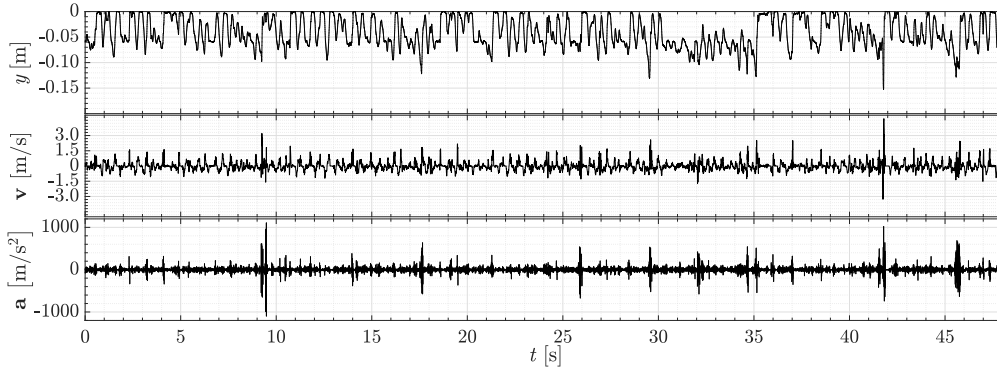


Figure 3.11: Distance between the bubble surface and blowdown pipe outlet y (top), velocity of the bubble growth and collapse v (middle), and the vertical acceleration of growing and collapsing bubbles a (bottom) during the DCC-05-4 experiment [37].

The largest bubbles reached -0.15 m under the blowdown pipe during their expansion with a velocity of -3 m s^{-1} and then condensed with a velocity as high as 4.5 m s^{-1} . The acceleration between the growth and break up of the bubble almost exceeds 2000 m s^{-2} . Figure 3.12 presents a closer view of acceleration data with corresponding images of the bubble modes.

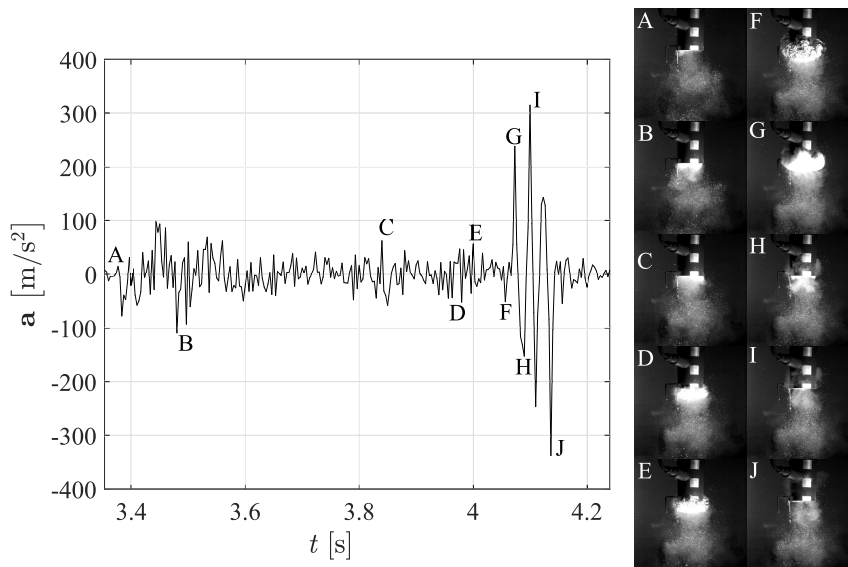


Figure 3.12: Short sample of acceleration data and related bubble modes A to J [37].

3.2 Frequency analysis

In addition to the evaluation of the basic properties of the bubbles, a Fourier transform based frequency analysis was performed. The Fourier transform based on the Fourier series represents periodic time series data as a sum of sinusoidal components [38]. FFT represents the time series in the frequency domain. When the data is not purely sinusoidal, FFT works best when the amount of data is large and the recording period is long. FFT can also be used for short periods, but it should be recalled that in those cases the period of the dominating lowest frequency oscillations becomes comparable to the length of the FFT sampling window, which affects the detection of the lowest frequencies.

3.2.1 Analysis of the DCC-05-4 experiment

Frequency analysis of condensing steam bubbles is an interesting field of research because it enables connecting bubble fluctuations to the other oscillating measured quantities. The frequencies of the bubbles were evaluated using FFT for distance y and volume V data. In other words, the volume (or distance) data are represented in the frequency domain. Figure 3.13 displays a typical FFT of the DCC-05-4 experiment.

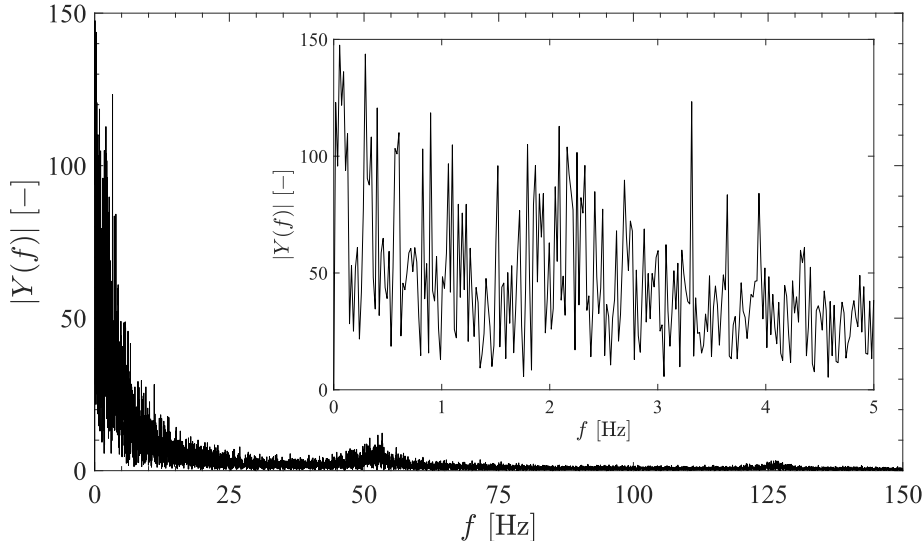


Figure 3.13: FFT of the DCC-05-4 volume data. $|Y(f)|$ is an absolute value of an amplitude of each frequency f .

Figure 3.13 shows that the frequencies are mostly low, but two higher frequencies are also visible, around 53 Hz and 126 Hz. Frequency analysis with FFT can be used to evaluate the most probable chugging frequencies. FFT shows sharp frequency spikes for pure periodic functions. Because the volumetric change of the bubbles is not purely periodic, the FFT spectrum becomes very spiky especially in the low frequencies as shown in Fig. 3.13. With some function fitting, the estimation of the probable chugging frequencies can be made.

The research on the natural oscillation frequencies of the condensing bubbles may benefit from FFT frequency analysis. The natural frequency of the oscillating bubble f_0 can be expressed analytically [39] as

$$f_0 = \frac{1}{2\pi} \sqrt{\frac{3\gamma P_0}{\rho_w R_0^2}} \quad (3.8)$$

where $\gamma [-]$ is the ratio of the specific heat of the steam, P_0 [Pa] is the steady state pressure, $\rho_w \left[\frac{\text{kg}}{\text{m}^3} \right]$ is the density of the water and R_0 [m] is the steady state radius of the steam bubble.

Natural frequencies f_0 [Hz] were calculated by using the evaluated diameters of the bubbles using Eq. (3.8). Frequencies fluctuate between 48 Hz and 250 Hz, when the most common natural frequency being around 80 Hz. The lowest natural frequency of the DCC-05-4 test should be near 44 Hz, corresponding the largest recognized bubble diameter of roughly 24 cm.

The change of the frequencies during the time t [s] can be seen by using a spectrogram. Figure 3.14 displays the spectrogram of the whole DCC-05-4 test.

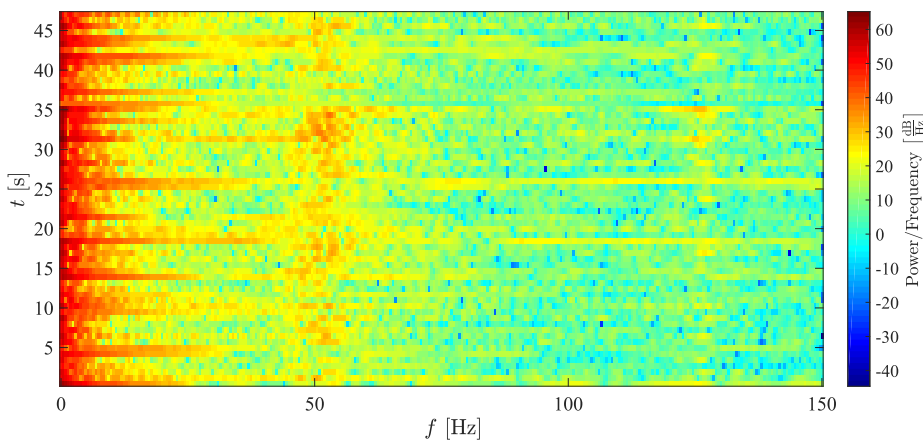


Figure 3.14: Spectrogram of the DCC-05-4 experiment [36].

Lower frequencies are dominant throughout the experiment, but higher values can be seen near 53 Hz and the 126 Hz throughout the experiment. The 53 Hz and 126 Hz frequencies are interesting. They are not a most probable natural frequencies of the bubbles, and are therefore presumably linked to the condensation process. The volume data in Fig. 3.10 shows three alternating bubble volume cycles named types A, B and C. The type A bubble cycle is the simplest one. The bubble grows in two parts: a fluctuating part, where the bubble grows oscillating, and a rapid growth part, where the fluctuating bubble grows fast and condenses completely very rapidly. Figure 3.15 presents the volumetric change of the type A bubble.

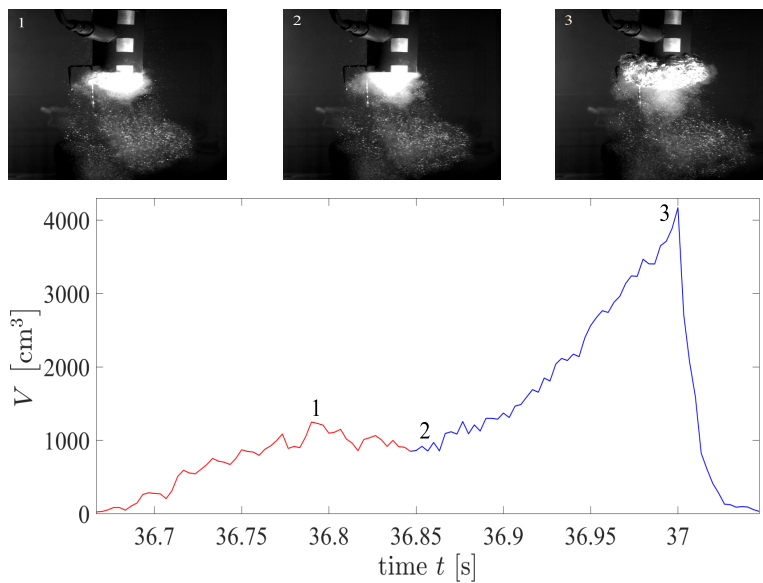


Figure 3.15: The change of volume V of the type A bubble. The red line presents the fluctuating part and the blue line presents the rapid growth part. Images 1 to 3 represent different phases of the type A bubble.

The type B bubble cycle consists of multiple oscillating parts of which the final one grows faster and breaks up rapidly. The volume in the preceding fluctuating parts does not fall to zero at any time. Figure 3.16 presents the type B bubble volume change.

The type C bubble consists of one or multiple fluctuating parts. The bubble oscillates, grows, and breaks with comparable rates without having a rapidly collapsing volume period. Figure 3.17 displays the type C bubble.

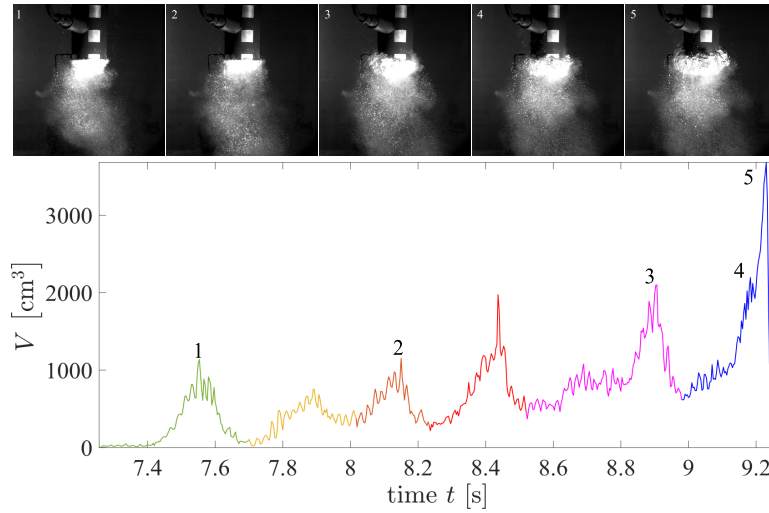


Figure 3.16: The change of volume V of the type B bubble. Lines from green to magenta represent the fluctuating parts and blue represents rapid growth similarly to type A. Images 1 to 5 represent different phases of the type B bubble.

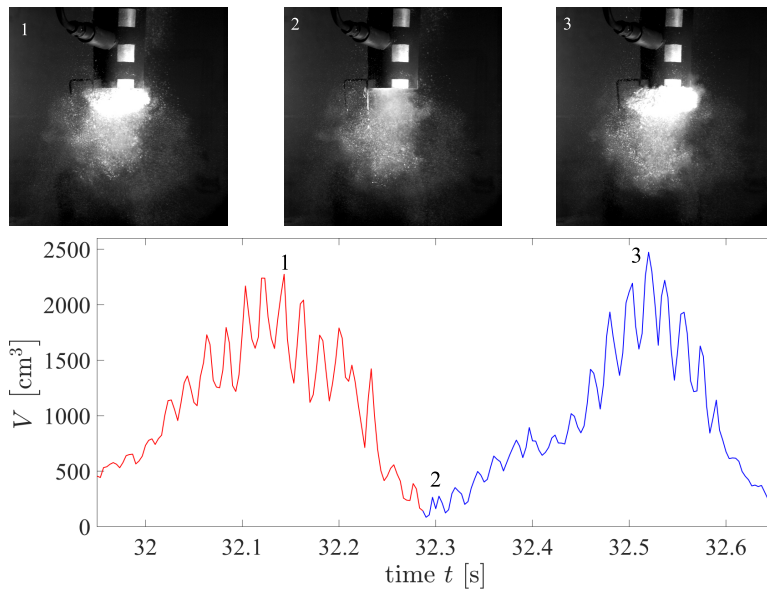


Figure 3.17: The change of volume V of the type C bubble. Red and blue lines represent different fluctuating parts. Images 1 to 3 represent different phases of the type C bubble.

A total of 77 bubble cycles were found, in which 23.5 % of the bubbles were type A, 18 % were type B and 58.5 % were type C. The FFT was calculated for all three types of bubbles. The FFT of the full cycle of types A, B and C showed that a frequency around 53 Hz was found in every bubble type, but a frequency around 126 Hz was found only in types A and B.

These three bubble types A, B and C have similar structures. Studying the frequencies more deeply and calculating the FFT for different phases of bubble oscillation (colours in Figs. 3.15–3.17) showed that 53 Hz appears through the whole condensation process in type A and B bubbles, while 126 Hz arises when the oscillating bubble grows to its full size. Oscillating bubbles which grow and diminish oscillating, as the green part of the type B bubble in Fig. 3.16, or type C bubble in Fig. 3.17, show a dominating 53 Hz frequency with no other considerable frequencies. These bubbles do not grow larger than the diameter of the blowdown pipe, change their sizes rapidly or have parts that grow or condensate rapidly. This makes it clear that 53 Hz spikes correspond to the frequency of the bubble surface whereas 126 Hz is linked to rapid condensation. Type A and C bubbles spread evenly throughout the experiment, whereas 71 % of type B bubble appear halfway through the experiment.

3.2.2 PPOOLEX hammer tests

FFT was also used to evaluate the frequency modes of the PPOOLEX facility. The frequency modes of the facility were evaluated from the pressure transducer data of hammer tests, where the PPOOLEX vessel was hit with a hammer, and pressure transducer and strain gauge data were recorded. The hammer tests were carried out for both a drained and filled pool. For the filled pool, the water level was the same as in the DCC-05 experiment. The pressure transducer p_6 was placed at the bottom of the pool, where it stood also during the blowdown experiments. Figure 3.18 shows the FFT of the hammer tests.

In the empty pool, the FFT shows a couple of sharp spikes: a high spike at 71.5 Hz and a lower one at 150.2 Hz. When the pool was filled with water up to 1.03 m above the pipe outlet, the vibrations increased significantly. The largest spikes are around 125 Hz, 136 Hz and 151 Hz. In the blowdown experiments, 126 Hz spike appears only with abruptly condensing type A and B bubbles but not with type C bubbles or as noise in video frames without bubble. It is highly possible that the vibrations of the pool resonate with the surface vibrations of the bubbles and strengthen the condensation.

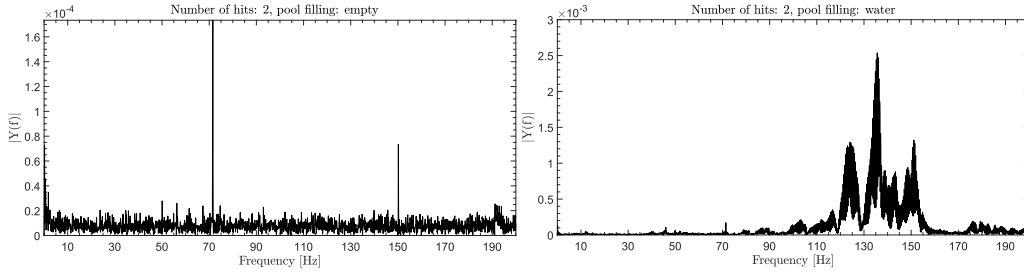


Figure 3.18: FFTs of the hammer tests. The PPOOLEX tank was hit twice with a hammer and the data was recorded using pressure transducers. The amplitudes are comparable. Notice the tenfold difference between the empty tank (left) and the water filled tank (right) [36].

3.2.3 Effect of the electricity grid

The possible effect of electric grid noise was measured comparing pressure transducer data during the experiment (steam injection on) to pressure transducer data without steam blowdown. Two pressure transducers in different places were compared, p_5 in the pool water, 5 cm from the blowdown pipes outlet, and p_6 at the suppression pool bottom. Figure 3.19 displays the FFTs of the pressure transducers data without the steam injection and during the experiment.

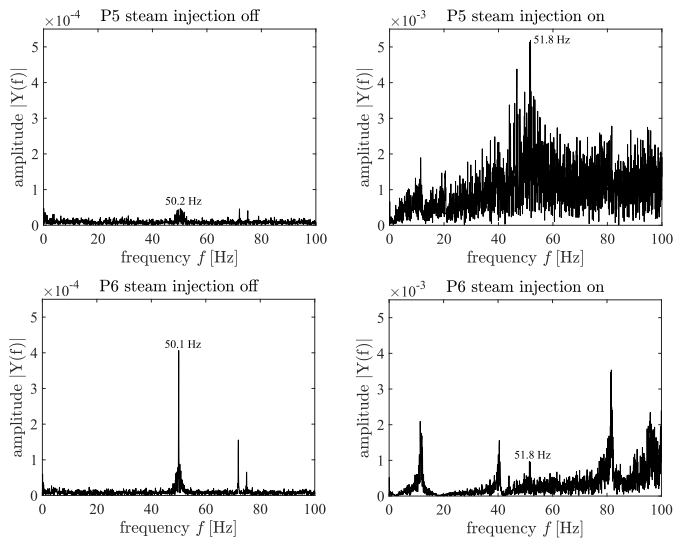


Figure 3.19: Pressure transducers p_5 and p_6 FFTs without steam injection (left) and with steam injection (during the experiment) (right). The amplitudes $|Y(f)|$ are comparable [36].

When the steam injection is off, the pressure transducer p_6 at the bottom of the pool shows a high, sharp signal from the electric grid (50.0 ± 0.1) Hz (lower left in Fig. 3.19), whereas in the middle of the pool, 5 cm from the blowdown pipes outlet, the grid signal blends into the noise in pressure transducer p_5 (top left in Fig. 3.19). When the steam injection is on, the noise of the electricity grid vanishes in the measured signal. The frequency of the electricity grid is also far from the frequencies observed in the DCC-05-4 experiment.

3.3 Modelling of DCC in pressure suppression pool systems

The image analysis data of the vertical vent pipe algorithm provided initial parameters and boundary conditions for CFD simulations of the DCC-05-4 case.

The velocity and acceleration values of the interfacial area are crucial when choosing computational grid resolution and interfacial area density models for Eulerian two-fluid CFD simulations of chugging DCC cases. As described in Chapter 2, the grid cell size in CFD simulations is limited by critical wavelength λ_c , which can be obtained from [40]:

$$\lambda_c = 2\pi \sqrt{\frac{\sigma}{\mathbf{a}(\rho_w - \rho_s)}}, \quad (3.9)$$

where σ is the surface tension, \mathbf{a} is the acceleration, ρ_w is the density of the water and ρ_s is the density of the steam. This limits the grid cell size in the CFD simulations of DCC-05-4 experiment to 1.0 mm-1.3 mm ($\mathbf{a} = 1100 \text{ m s}^{-2}$, $p = 3.1 \text{ bar}$). At the same time, the predominant wavelength λ_m ,

$$\lambda_m = 2\pi \sqrt{\frac{3\sigma}{\mathbf{a}(\rho_w - \rho_s)}}, \quad (3.10)$$

is 1.7 mm-2.4 mm. The grid resolution scale of 1 mm is overwhelming for practical CFD simulations of transient 3D phenomena such as chugging. This is why the subgrid scale models are being developed to capture interfacial area density even with relatively low resolution grids.

The FFT of the original algorithm volume data was also compared to the simulation data of NEPTUNE_CFD. Five CFD cases were compared. Table 3.2 presents simulated cases and parameters.

Four out of five cases (cases 1 to 4) were successful and the chugging mode appeared. Case 5 had no chugging. Cases 1 and 2 have been simulated without the RTI model [42] and cases 3 and 4 with the RTI model.

Table 3.2: CFD simulation parameters.

Case ID	DCC Model	Interfacial Area Density	Interfacial Momentum Transfer	σ Model	Grid
Case 1	Coste C	$ \Delta\alpha_1 $	Coste LIM	none	1 mm
Case 2	Coste C	$ \Delta\alpha_1 $	Coste LIM	devel.	1 mm
Case 3	Coste C	$ \Delta\alpha_1 $ + RTI	Coste LIM	none	5 mm
Case 4	Coste C	$ \Delta\alpha_1 $ + RTI	Coste LIM	devel.	5 mm
Case 5	Coste C	$ \Delta\alpha_1 $	Coste LIM	none	5 mm

Coste C = Coste 2004 continuous model [41], RTI = Rayleigh-Taylor Instability model [42], LIM = Large Interface Model of Coste [43], devel. = under development/not validated

Case 5 was similar to case 1, but a low resolution grid was used. The RTI model of Pellegrini *et al.* [42] directly uses the pressure gradient causing a force accelerating the gas-liquid interface. This acceleration can be orders of magnitude higher on condensing bubbles than the acceleration of gravity typically imagined when considering Rayleigh-Taylor instability between heavier and lighter fluid. The FFTs of each of the cases 1 to 5 are presented in Figs. 3.20–3.24.

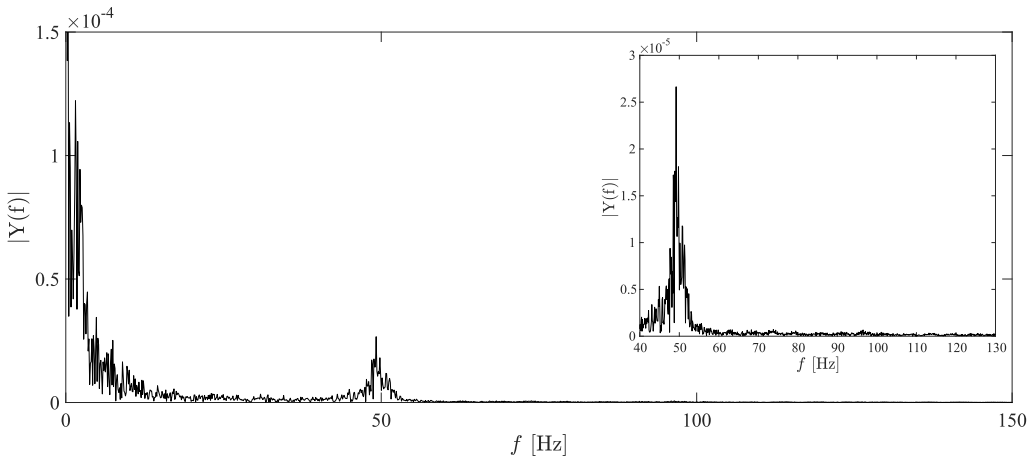


Figure 3.20: FFT of Case 1. A high resolution grid (1 mm) was used without σ and RTI models.

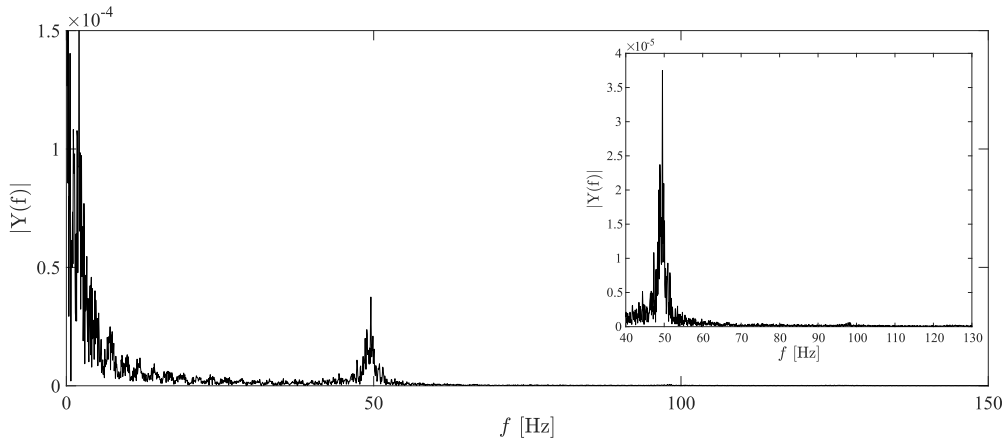


Figure 3.21: FFT of Case 2. A high resolution grid (1 mm) was used with the σ model and without the RTI model.

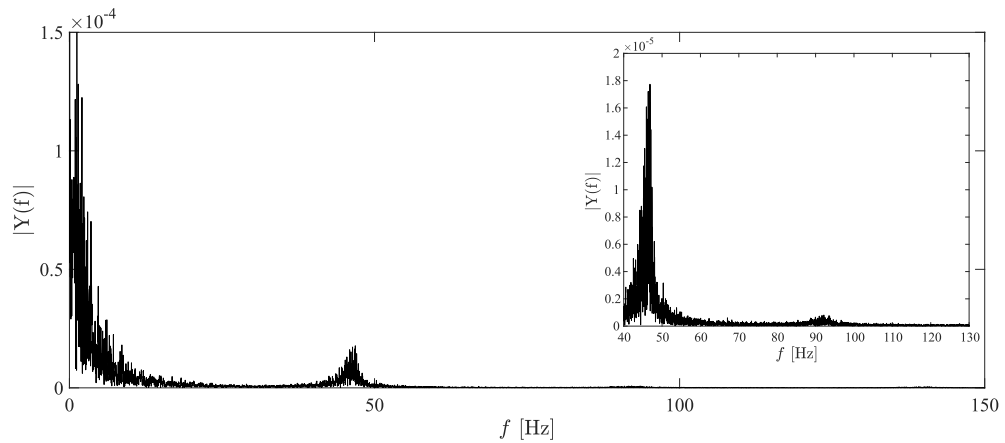


Figure 3.22: FFT of Case 3. A low resolution grid (5 mm) was used without the σ model with the RTI model.

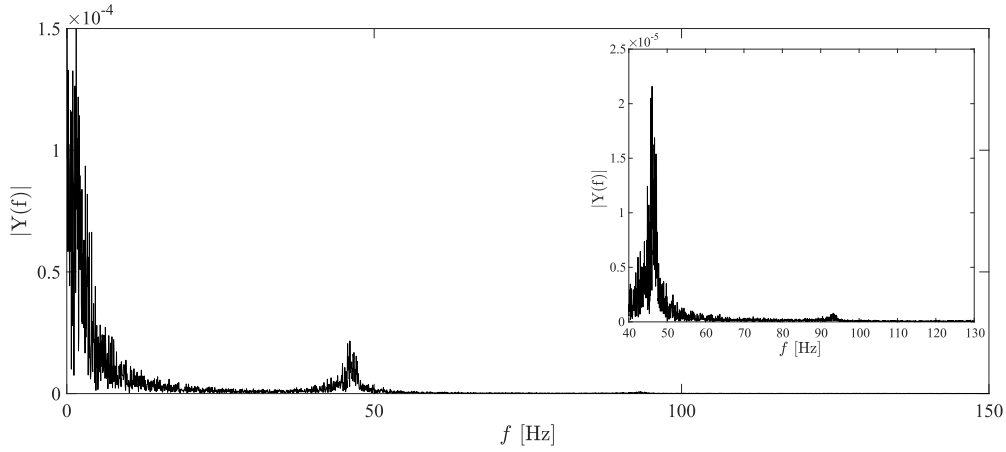


Figure 3.23: FFT of Case 4. A low resolution grid (5 mm) was used with the σ model and the RTI model.

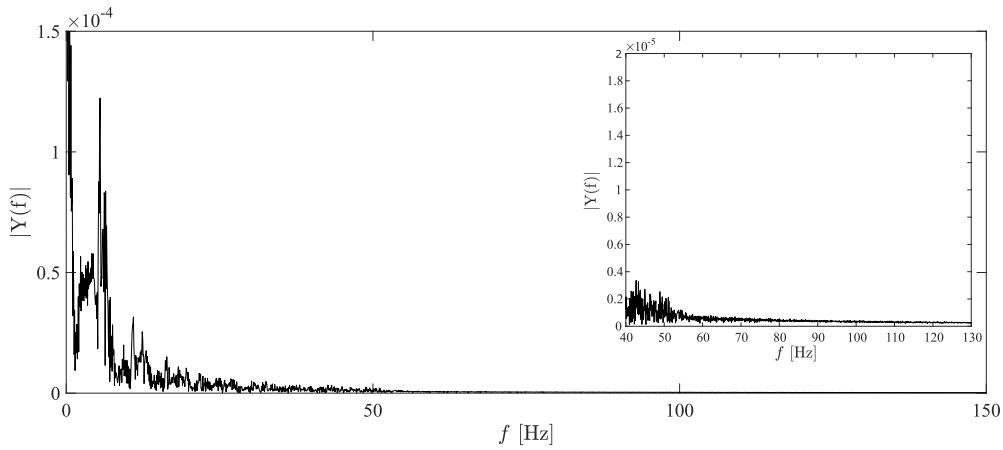


Figure 3.24: FFT of Case 5. A low resolution grid (5 mm) was used without σ or RTI models.

In the successful cases 1 to 4 where chugging occurred, a sharp spike around 50 Hz was clearly visible and the most probable chugging frequencies varied at the same level as in the FFT of the original algorithm's volumetric data. In the bigger picture, no other higher frequencies are present. A closer look reveals that another small spike appears near 90 Hz, when the RTI model is used. The spike sharpens when a surface tension σ model is included. Without the σ and the RTI models in case 1, no extra spikes appear at higher frequencies. With the σ model without the RTI model in case 2, some changes may be seen near 100 Hz, but their significance is difficult to determine.

Unsuccessful case 5 as well as other unsuccessful cases where chugging did not occur, had sharp spikes neither around 50 Hz nor higher. This shows that the 50 Hz spike should be a feature of the bubble during rapid condensation.

Higher spikes in cases 3 and 4 showed that using the RTI model affects the simulation results positively when comparing to the image analysis results. The higher frequency spikes in the CFD and the image analysis data are not exactly at the same frequency, but because the form of the FFT is similar in both cases, further research is recommended.

3.4 Extended algorithm for horizontal sparger orifice

The original algorithm was made for vertical vent blowdown pipe cases, where the bubbles hardly ever detached from the vent outlet and only a single bubble appeared at a time. When the algorithm was successfully applied to vertical cases, a decision was made to expand the algorithm to cover injection from a horizontal sparger orifice. Separate effect test facility SEF-POOL and the SEF-INF2 experiment was used to develop the extended algorithm.

3.4.1 SEF-POOL test facility and SEF-INF2 experiment

The separate effect test facility SEF-POOL was designed for the direct measurement of the effective momentum induced by a steam injection through a single hole or a few sparger holes. The phenomenological reference system for the SEF-POOL facility is the SRV sparger pipe of a BWR. Figures 3.25 and 3.26 present a general view of the SEF-POOL test facility.

The SEF-POOL test facility consists of an open, water filled, uninsulated, 1500 mm long, 300 mm wide, and 600 mm high stainless steel pool with sparger piping; an insulated stainless steel DN80 line ending up at an orifice plate. A steam line, connected to a steam generator of the PACTEL test facility runs downwards from the top of the suppression pool and bends in the horizontal direction. The steam is injected through the orifice plate, which has one or multiple orifices.

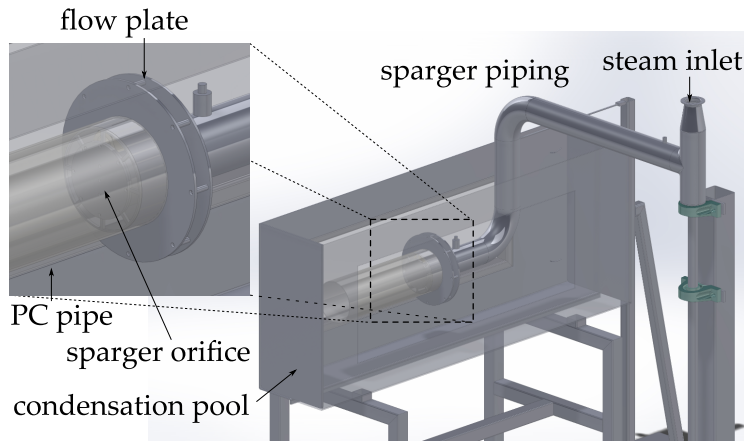


Figure 3.25: SEF-POOL test facility.

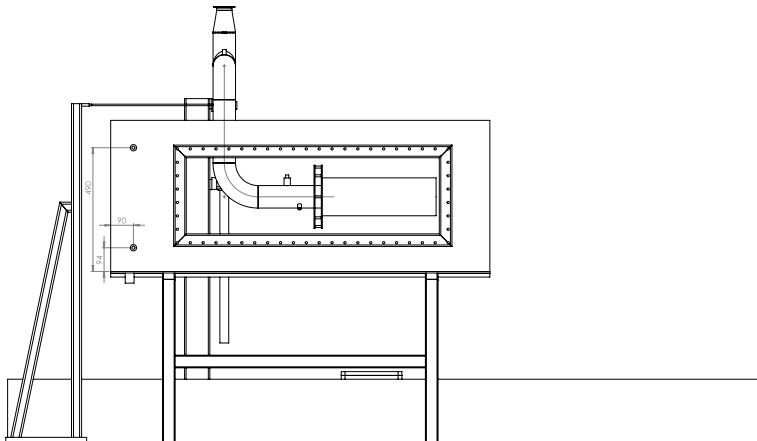


Figure 3.26: Side view of the SEF-POOL test facility.

Different orifice diameters and extension angles can be used. Steam condenses inside an open detachable polycarbonate (PC) pipe connected to the flow plate system which guides replacement water to the PC pipe. The purpose of the PC pipe is to create a parallel flow pattern so that the amount of momentum transferred from the steam to the liquid can be estimated at the outlet of the PC pipe with, for example, hot wire probes. Temperatures are measured from the sparger pipe and suppression pool. Pressure transducers are used to measure steam pressure in the sparger piping. The water level in the pool is measured with a differential pressure transducer. Large windows along both sides of the pool enable the use of one high-speed video camera and different lighting conditions. A more detailed description of the SEF-POOL test facility is presented in [44].

The main purpose of the SEF-INF2 experiment was to test the validity of large interface condensation and interfacial area models in sparger cases of CFD simulations with NEPTUNE_CFD and OpenFOAM CFD codes. It was also considered as a first reference case for the development of the extended algorithm.

SEF-INF2 experiment consists of six recorded short tests named SEF-INF2-1. . .SEF-INF2-6. A single orifice with a diameter of 16 mm was used. The initial water temperature of the pool was 285 K. The steam mass flow rate was 36 g s^{-1} which approximately corresponds to the steam mass flux of $180 \text{ kg m}^{-2} \text{ s}^{-1}$. The steam mass flow rate was kept constant. Six tests, SEF-INF2-1. . .SEF-INF2-6, were recorded at different pool temperatures varying from $T_w = 317 \text{ K}$ to 358 K (44°C to 85°C). According to the condensation regime map of Song *et al.* [26] presented in Fig. 3.27, SEF-INF2 was operated mostly in condensation oscillation mode (CO), but SEF-INF2-6 was in bubbling condensation oscillation mode (BCO).

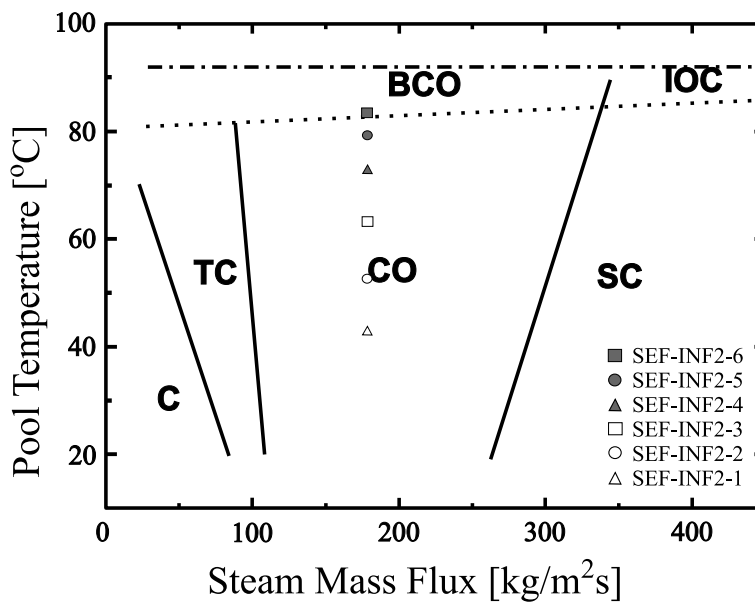


Figure 3.27: Condensation regime map of Song *et al.* for horizontal steam injection [26]. C refers chugging, TC transitional chugging, CO condensation oscillation, BCO bubbling condensation oscillation, SC stable oscillation, and IOC interfacial oscillation condensation mode.

The SEF-INF2-6 experiment was chosen for this study. The bubbles in SEF-INF2-6 have a clear continuous interface and they detach from the orifice and condense frequently. Thus, this sample of the BCO mode is interesting for both the numerical large interface condensation modelling and the image analysis of large

bubbles. Furthermore, these warmed up pool BCO conditions are among the less frequently measured and modelled modes.

3.4.2 Development of the extended algorithm

In the horizontal sparger cases, bubbles detach from the sparger orifice, travel forward oscillating, and finally condensate in the pool water. Multiple bubbles might exist at the same time. Due to the high momentum, none of the bubbles travel backwards to the pipe. These multiple bubbles have to be tracked and labelled in such a way that all of the bubbles can be sorted out.

Six 0.935 s grayscale videos were recorded (one for each run SEF-INF2-1 . . . SEF-INF2-6) with a frame rate of 2800 fps. The resolution of each video frame was $1024 \text{ px} \times 528 \text{ px}$. The lens focal length was 24 mm and the lens aperture f2.4. An updated version of Phantom Camera Control (PCC) software was used [45], which allowed the use of a lossless tagged image file format (TIFF). The RGB Cine video was converted to 2618 TIFF images. Figure 3.28 displays a typical view of the SEF-INF2-6.

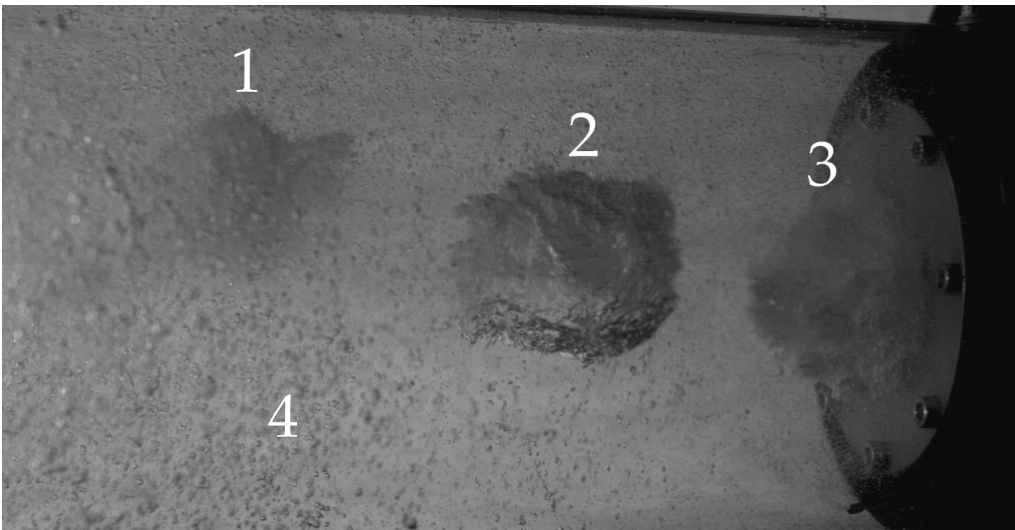


Figure 3.28: A typical view of the SEF-INF2-6 test. The image is captured near the end of the test. (1) a bubble near the end of its lifetime, (2) a detached bubble, (3) a nascent bubble, and (4) a swarm of small bubbles.

As Fig. 3.28 shows, the facility does not have many obtrusive objects such as measuring devices in the image area, but the threshold differences are much smaller than in the DCC-05 case. The difference between the grayscale values of the bubbles and the image background is minor. Three different bubbles can be seen: a

bubble near the end of its lifetime (1), one nicely shaped detached bubble (2) and one nascent bubble near the orifice (3). The last one (3) is difficult to distinguish from the orifice plate. At the end of the experiment, a large number of small bubbles (4) have appeared and are visible inside the PC pipe.

Minor threshold difference leads to extensive pre-processing. The image has been divided in twenty parts which are separately modified by brightening and sharpening. Because bubbles travel through the whole image, the threshold values of the pixels vary largely. All frames are allotted into twenty parts. This image segmentation takes the largest amount of computer capacity. For each part, the best threshold value has been found and the grayscale image converted to a binary image. After the conversion process in the pattern recognition part, the edges of the bubbles were detected using the Moore neighbourhood method with Jacob's stopping criteria, as in the original algorithm. Also the label matrix and number of objects in the image were calculated. Figure 4 in Publication IV presents an image sequence of recognized bubble boundaries.

The greatest difference between the original algorithm and the extended algorithm comes in post-processing. For all recognized bubbles, the centres of mass were calculated and the distance between the centre of mass and bubble boundary pixels was evaluated for all integer angles 0° to 360° in 2D plane. In some cases, incorrect boundary recognitions appeared, because there was only a slight difference between the bubble and background thresholds. Due to incorrect recognition, more than one pixel of the border might be located on the same line between the centre of mass and the border pixel. In these cases, distance r is calculated for all border pixels in the same direction and the mean value is calculated. Figure 5 in Publication IV presents a more descriptive image of this correction. Surface velocities and accelerations for all integer angles from 0° to 360° were calculated using centres of masses and the forward-difference method. Standard polar coordinate system angles are used, in where 0° faces the orifice and the angle increases counterclockwise.

The consecutive frames have one to three bubbles which should be connected. Tracking of the condensing bubbles is based on a Simple Tracker by Tinevez [46]. The Simple Tracker is a particle tracking algorithm which can deal with "gaps". A gap appears when one particle that was detected in one frame is not detected in the next one. If not dealt with, this generates a track break, or a gap, in the frame where the particle disappears, and a false new track in the frame where it reappears. In this study, the centres of mass of the bubbles act as such particles.

The Simple Tracker needs two input values, the maximum linking distance and the maximum gap closing. The maximum linking distance defines a maximum value in bubble linking. Two bubbles will not be linked even if they are the closest pair, if the distance of their centres of mass is larger than the maximum linking

distance. The maximum gap closing defines a maximum frame distance in gap closing. Frames further away than this value will not be investigated for gap closing. This study employs a maximum linking distance of 100 px (approx. 30 mm) and a gap closing value of five frames is used. In other words, when a bubble grows, the tracker tracks the coordinates of the centres of mass. When the growing bubble detaches from the orifice plate and a new bubble starts to grow, this new bubble is linked to the first bubble as long as the distance between the centres of mass of these two bubbles is smaller than 100 px. When a bubble starts to condensate, it might disappear for a while. If the bubble or rather a swarm of its residue bubbles does not reappear within five frames, the tracking of that bubble ends. If the bubble returns after a five frame gap, it will be marked as a new track even if the distance between the returning bubble and the previous bubble is less than 100 px. Figure 3.29 displays the operation of the Simple Tracker by showing the centres of mass of recognized bubbles and their linking distance in seven consecutive images.

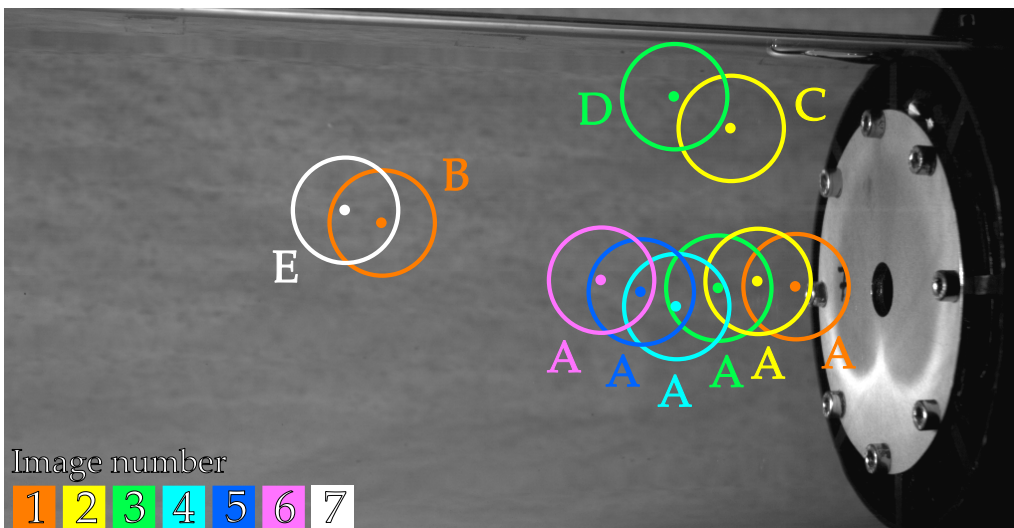


Figure 3.29: Operation of the Simple Tracker. Figure represents the centres of mass of recognized bubbles in 7 consecutive images: 1 (orange), 2 (yellow), 3 (green), 4 (cyan), 5 (blue), 6 (pink) and 7 (white). Coloured dots are centres of mass of the bubbles and circles around the dots represent the maximum linking distance. The image sequence consists of 5 different tracked bubbles named A to E.

The first image (orange dots and circles), contains two bubbles A and B. The second image (yellow), also has two bubbles. The positions of the bubbles in the second image are compared to the positions in the first image. The first new bubble (yellow) is within the linking distance of bubble A, so the tracker links it to

the track of bubble A. The second bubble in the second image is not within the linking distance from bubble A or B and is marked as C. In the second image, there is no bubbles within the linking distance from bubble B, so bubble B has disappeared. In the third image (green), two bubbles are found, and their positions are compared to the positions in the second image. One bubble is connected to bubble A and one is near bubble C. This new bubble (green) is not within linking distance from bubble C, and it is marked as D. Bubble C has disappeared and bubble B is still missing. In the fourth image (cyan), only one bubble appears. It is within the linking distance from A and is marked to belong to the track of bubble A. Bubble B has not appeared in three consecutive images, bubble C has been absent from two images, and bubble D has simply disappeared.

The fifth (blue) image also includes only one bubble. It is still within the linking distance from A. Similarly the sixth image (pink) contains only one bubble marked as A. Now, bubble B has been gone for five images, so its track has ended (gap closing was set to five images).

The seventh image (white) contains one bubble near the place where the bubble B disappeared. It is actually within the linking distance from the last detected position of bubble B, but because the tracking of bubble B ended, the bubble is marked as a new bubble, E. Bubble A has disappeared and if it does not appear during the following four images, its tracking will end. Tracking of the bubble C ends in this image, because it has been gone for five images. Bubble D is still being tracked, but if it does not appear in the following image, its tracking will also end. Short tracks, such as those of bubble C, will be removed from the data.

After constructing the tracks of the bubbles, different properties of the bubbles can be evaluated, such as bubble lifetime, formation frequency, and surface velocities and accelerations to different directions in the 2D plane.

3.4.3 Analysis of the SEF-INF2-6 experiment

Overall, 67 bubbles were tracked; the mean lifetime of the bubbles was 24.7 ms and the bubble lifetimes varied from 9.6 ms to 36.1 ms. A total of 70% of the bubbles had a lifetime between 20 ms to 30 ms, and approximately 20% had a longer lifetime.

The formation frequency of the bubbles remained quite constant during the experiment. The mean time difference between bubble formations was 14.0 ms, ranging from 1.8 ms to 29.3 ms. The corresponding mean formation frequency of the bubbles was approximately 71.6 Hz.

The SEF-INF2 experiment was recorded using one side camera, which recorded the side profile of the bubbles. Thus, all of the properties of the bubbles were evaluated in the 2D plane. Surface velocities and accelerations were evaluated

for directions 0° to 360° , with 1° resolution. The positive direction of velocity is in the direction of the bubble's growth, in other words, from right to left. Velocities are plotted in steps of 45° . Figure 9 in Publication IV presents the surface velocities of the one bubble through its lifetime. The greatest change in bubble surface velocities can be found in the 90° direction – straight upwards. The largest velocities found in this bubble are near 50 m s^{-1} . Some bubble surfaces had velocities higher than 80 m s^{-1} . Larger changes can be found also in other upward directions: 45° , and 135° . In contrast, the forward direction, 180° , seems to be calm and changes in the velocity small for the whole lifetime of the bubble. Downward directions are quite calm, except 270° , where a large, nearly 30 m s^{-1} change occurs at 0.03 s.

Figure 10 in Publication IV presents the surface acceleration of the one bubble through its lifetime. Due to the high frame rate, calculated accelerations of the bubble surfaces grew large. The most significant acceleration difference corresponding to two consecutive images was near $5 \cdot 10^5 \text{ m s}^{-2}$ in the upward direction. In the vertical direction, only one larger change was visible in the middle of the bubble's lifetime. In other upward directions of 45° and 135° , larger changes in acceleration can be seen during the whole lifetime of the bubble. The downward directions remained calm, but the horizontal directions of 180° and 360° showed more activity than the corresponding velocities showed. Velocities and accelerations for all directions between 0° to 360° with a 1° interval were estimated in this study.

The volumes and surface areas of the bubbles were not evaluated. In the case of DCC-05 blowdown pipe experiment, three cameras were used. The bottom camera data indicated that the bubbles were approximately axisymmetric during the experiment, and thus the volumes and surface areas were evaluated using cylindrical plates. In the SEF-INF2 experiment only one camera was available. Assumption of the symmetrical shape could have been used, but because of its uncertainty, the evaluation of the volumes and surface areas were left for future research.

CHAPTER 4

Discussion

The MATLAB software was a natural choice for developing the algorithm. It has a built-in image processing toolbox, it is easy to use and it was readily available. However, nothing limits the use of other programming languages, such as Python or the Julia, which are widely used in scientific research. Languages suitable for high-performance numerical analysis might be even better in the hands of an experienced programmer. With MATLAB, a wide variety of readily available functions can be used if the background of the functions is known.

The amount of pre-processing needed in the algorithms depends highly on the test facility used and the prevailing video shooting conditions. The more unwanted objects there are in the video, the more pre-processing is needed. The original algorithm for vertical vent pipes needed pre-processing mostly due to obtrusive measuring equipments and uneven lighting. The darkest shadows could not be removed and part of the bubble was always overexposed, but otherwise pre-processing worked well enough.

A clearly visible difference between the intensity values of the background and the intensity values of the bubble made edge detection easier. The darkest side of the largest bubbles is missed, but the effect of this error is mitigated in the large amount of data.

Fortunately, the abandoned bottom camera video showed that with a DN100 blowdown pipe the bubbles were symmetrically shaped, which enabled the use of cylindrical plates in volume and surface area evaluation. The method was appropriate and showed realistic results, notwithstanding the underestimated surface area.

A large amount of data was needed for the first algorithm. Due to the limitations of the camera capacity, a larger amount of data, in other words a longer video, meant a smaller frame rate. 300 fps was chosen, which was suitable also for frequency analysis. In frequency analysis the Nyquist frequency is a half of the sampling rate, which allows FFT up to 150 Hz, far enough above the typical

chugging frequency of 2 Hz, so that the bubble dynamics could be well detected and characterised. A 48 s video provided almost two bubbles per second, which offered a sufficient amount of comparable data. A lower frame rate may affect the evaluation of the surface velocities and acceleration. When the frame rate is low, the time difference between consecutive images becomes long, and thus the position of the surface may change significantly between two images, and some fluctuations may disappear. In spite of this lower frame rate, vertical surface velocities remained realistic. The accelerations rose to a high level, but in the case of rapid condensation, even higher accelerations are possible.

The frequency analysis of the vertical vent pipe case DCC-05-4 showed three different bubble types: A, B and C. The bubbles were selected purely visually from the volumetric data. Type A and B bubbles consist of steam bubble expansion and a break up period, whereas the type C bubble just fluctuated without visible collapse. Frequency analysis showed two visible spikes: around 53 Hz and around 126 Hz. The 53 Hz frequency appears through the whole experiment, irrespective of the bubble type, and seems to be the natural fluctuation frequency of the bubbles. In contrast, 126 Hz is visible only in type A and B bubbles, which have rapid expansion and collapse parts. The 126 Hz frequency is interesting. It appears, most of the time, during the expansion period of the A type bubble, and with type B bubbles, it appears little by little, when the sharp expansion parts became visible. In type C bubbles, there is no 126 Hz frequency. Further analysis is required for other DCC-05 tests to better understand these frequencies.

Similarly to the effect of the experimental facility, the effect of the frequency of the electricity grid was studied. The effect is visible when the steam injection is off, but it disappears from sight in the data when the steam injection is on and tests are running. Also the choice of light source affects the results. Fluorescent lights may disturb video recording by blinking visibly, and should be avoided in the experiments, whereas halogen lamps and LED lights are generally suitable. A well fitted diffuser can be used to avoid bright spots from LED lights. It is also important to record technical details of the lighting used in the experiments for potential problem situations.

The image analysis data of the algorithm was applied successfully to CFD simulations, to which it provided initial parameters and boundary conditions. The FFT data of the CFD simulations was compared to the FFT data produced by the algorithm. A similar lower frequency around 50 Hz was found in successful NEPTUNE_CFD simulations, but not in unsuccessful cases which did not contain chugging. 126 Hz spikes were missing, but low resolution cases with RTI model showed secondary spikes around 90 Hz. High resolution cases with RTI model were not available. Both low and high resolution cases without RTI model did not include secondary spikes. In CFD simulations, the facility walls are completely rigid and cannot resonate with the bubble. If the density of the grid is high

enough, absence of the 126 Hz peak in CFD supports the notion that wall-bubble resonance accelerates bubble collapse. An excessively coarse computational grid might also cause the absence of the 126 Hz frequency. In conclusion, the pattern recognition based image analysis algorithm provided valuable data for CFD simulations.

After the development of the original algorithm for vertical vent pipes, the basic principles of the extended algorithm for horizontal spargers were easy to identify. Similarly, the extended algorithm consists of three parts: a pre-processing part, a pattern recognition based edge detection part, and a post-processing, i.e. image analysis part.

The frame rate of the SEF-INF2 was set higher than in the DCC-05 tests, which shortened the videos. 700 fps was noticed to be too slow [47], and therefore a frame rate of 2800 fps was chosen. This allowed six approximately one second recordings with the same amount of data as was in 48 s at 300 fps in DCC-05. A higher frame rate made sure that none of the bubbles remained unnoticed due to a long time difference between consecutive images.

Whereas the intensity values between the background and the bubbles differed clearly in the DCC-05 experiment, the intensity values of the SEF-INF2 experiment video were very close to each other, therefore a complicated thresholding process was needed to separate the bubbles from the background. Edge detection was corrected and improved. Due to multiple bubbles appearing in the same figure, bubbles were tracked and labelled. A simple particle tracker worked well. Visual observation of the video showed that there were no sporadic bubbles when all short tracks were removed from the data. Volumes and surface areas were not evaluated in this study but will be added to the algorithm in the future.

A high frame rate better enabled the evaluation of the interfacial area of the bubbles. Surface velocities and accelerations were calculated for all integer angles between 0° to 360° instead of the vertical direction. This allowed a more detailed analysis of the interfacial area and is one of the best improvements in the extended algorithm. Because only one side camera was available, only the side profiles of the bubbles in 2D plane were recorded. This may cause errors if the bubbles do not travel straight in the pool. A second camera should be added to the front or top side of the pool for future research. The velocities and accelerations should be analysed in more detail and the evaluation of angle-resolved velocities and accelerations should be added to the vertical vent pipe algorithm.

Altogether, the algorithms work well when studying condensation instabilities in suppression systems. The computer processing time with the longer original algorithm remains reasonable: two to three hours with one computer (Intel[®] Xeon[®] CPU at 3.30 GHz, 4 cores, 8 threads, 16 GB RAM). Although the algorithms are made for quantification of large steam bubble oscillations and chug-

ging, the algorithms consist of several parts, which are not dependent on the details of the experimental results. Algorithms for various purposes can be produced by combining different parts. In other words, the algorithms should work also i.e. with small bubbles in boiling or with different pipe flows, when the video shooting conditions, pre-processing, edge detection and post-processing are chosen properly.

4.1 Recommendations for further research

In the design of future test facilities, it is recommended to plan filming conditions before the construction of the facility. In every experiment, there should be a possibility for a removable, rigid camera base. Even if there is a suitable computer aided camera calibration software at hand, in a rerun of the experiment it should be possible to use exactly the same camera positions as before. Also, a profound knowledge of camera utility programs increases the quality of filming and improves the experiments by recognizing possible errors in advance. Optical errors of the camera system should be recognized, as well as the optical aberrations and the effects of geometric optics, caused by e.g. the refractive index difference of different materials.

The construction of a separate test facility for algorithm development purposes is highly recommended. The facility would help to optimize and evaluate programming based errors (errors in pre-processing and edge detection) without introducing errors arising from complex test facilities. It also provides a more accurate error estimation for the algorithms. The separate facility can also be used to study the effect of different filming conditions, such as aperture, exposure, white balance, frame rate, shooting angles, calibration, and other techniques which would have a positive effect on both the algorithm development and knowledge of experiment design.

To enhance the surface area and volume evaluations of the steam bubbles, the use of spherical harmonics can be tested for improving the edge detection data to obtain more accurate results. The use of spherical harmonics enables a high quality 3D modelling from 2D images. Spherical harmonics have been successfully used to characterize aggregate shapes in concrete [48] and with particle shape generation [49]. Similarly, steam bubbles are known to have complicated shapes, so the method is worth trying.

The algorithms will be made more user friendly in the future. The evaluation of the volume and surface area will be added to the extended algorithm. Also the frequency analysis of the vertical vent pipe cases will continue and the evaluation of the angle-resolved velocities and accelerations will be performed for the vertical vent pipe data.

In CFD simulations, a high resolution grid sensitivity analysis should be carried out in cases where the RTI model is used for finding reasons for the higher frequencies in FFTs.

Finally, future developments of the algorithm and test facilities should also consider the needs of data users. The algorithm already enables detailed characterisation of the geometry of the phase interface, and this information can be used to estimate the size of largest turbulent eddies which control the liquid-side heat transfer away from the interface, and thereby, the rate of condensation. At high frame rates, even the interface wrinkle dynamics could become tractable.

CHAPTER 5

Conclusions

The direct contact condensation of steam, condensation oscillations and chugging phenomena are relevant for nuclear safety and the design of safety features for nuclear power plants. Large steam bubble oscillations and chugging have been investigated experimentally at LUT University in PPOOLEX and SEF-POOL facilities. A large amount of high-speed video data has been collected. It was necessary to create pattern recognition based image analysis algorithms to automatically extract quantitative data from the raw image sequences.

The DCC-05 experiment of the PPOOLEX large scale integrated test facility was used as a reference experiment for the original algorithm. A stainless steel DN100 blowdown pipe was used and the pipe was submerged 1.05 m into the condensation pool water. Initial water temperature was 298 K and steam mass flow rate varied between 75 g s^{-1} to 200 g s^{-1} . Condensation mode of the experiment was considered chugging based on the regime map of Lahey & Moody [19].

An image analysis algorithm based on pattern recognition was successfully designed and developed for vertical vent blowdown pipes. The algorithm evaluates the basic properties of steam bubbles, such as surface area, volume, vertical surface velocities and accelerations, and frequencies for one bubble in a stationary location. The volumetric change of the bubble is well quantified, but the surface area is underestimated due to smoothing of the voxelized bubble surface. Frequency analysis showed three different bubble types: A, B, and C. Types A and B collapse rapidly at the end of an oscillation sequence, whereas the most common bubble type C fluctuates slowly without a rapid collapse. Frequency analysis also showed that all bubble types have a frequency of 53 Hz, but only fast condensing bubbles A and B have a higher 126 Hz frequency.

The algorithm was also applied to CFD simulations, where it was used to determine critical wavelengths of condensation driven Rayleigh-Taylor instability in order to establish the most suitable grid density for the simulations. The frequency analysis of the CFD volume data showed a similar frequency spike around 50 Hz in all successful cases, while in the unsuccessful cases the spikes

around 50 Hz were missing. In the low resolution grid cases where the RTI model was used, the second spike appeared around 90 Hz with and without the surface tension model. A high resolution grid case with the RTI model was not available. Without the RTI model, the second spike did not appear, even with the high resolution grid. This raised discussion about the possibility of a connection between the steam bubble condensation process and the resonance frequency of the test vessel.

The algorithm was extended to cover cases where multiple bubbles appear within the image area at the same time. The SEF-INF2 experiment of the SEF-POOL facility was used as a reference test for the extended algorithm. Multiple simultaneous, horizontally moving steam bubbles were recognized using similar and improved pre-processing functions as with vertical vent pipes. A particle tracker was added to distinguish different bubbles in the same image from each other. The formation frequencies of the bubbles were evaluated, and instead of vertical surface velocities and accelerations, the algorithm was extended to calculate velocities and accelerations in all directions in a 2D plane.

The research verified that even from moderate quality video material, it is possible to acquire high quality quantitative data, if the frame rate of video had been high enough and the most obtrusive objects could be filtered out from it as well. The algorithms work well. The use of cylindrical plates for volume calculations of the large steam bubbles in transients is a good and working solution in cases where bubbles are identified symmetrical from the the original video, and pure stereoscopic data are not available.

Surface velocities and accelerations of large steam bubbles give valuable information on bubble dynamics for CFD modelling and code validation. With the frequency analysis of image analysis data, different bubble modes and bubble behaviour can be studied.

The algorithms can help to understand phenomena that underlay the design of BWR safety systems. Deeper understanding allows design changes to improve safety and/or economics of plant operation. Moreover, direct contact condensation phenomena are relevant for other reactor designs as well. In particular, many passive safety systems contain components or operational features where condensation instabilities are possible, and, unless properly taken account in design, potentially detrimental to system performance.

The algorithms are not limited to specific cases. They consist of parts which are easily applied to different research needs. For example, the principles of the algorithms should work properly with small bubbles in nucleate boiling if the video resolution, magnification and frame rate are selected properly.

The algorithms facilitate lighting design and the filming of experiments. In the

long term, the algorithms may reduce the costs of experiments when knowledge of large steam bubble dynamics increases and the demand for reproduction of the experiments diminishes.

In future studies, the construction of a separate test facility made only for algorithm development could give valuable information about optical limitations, suitable initial values and perfect experimental conditions for the design of thermal hydraulics experiments.

As new measuring techniques, such as PIV and WMS, have already been applied separately to thermal hydraulics experiments, the algorithm data could be used to analyse PIV and WMS data. Also, important information can be obtained by comparing algorithm data to other modern measuring techniques.

Improved understanding of interface dynamics and heat transfer mechanisms at the interface in turn allow faster and/or more accurate prediction of global parameters of interest, such as condensation driven loads on pool structures, or system pressure variations due to rapid condensation. Such knowledge, in turn, allows optimisation of nuclear power plant safety, availability and economy in all applications where rapid contact condensation is of interest.

References

- [1] IAEA. Nuclear power and climate change. <https://www.iaea.org/topics/nuclear-power-and-climate-change>, 2019. Accessed: 2019-05-13.
- [2] WNA. World nuclear power reactors & uranium requirements. <http://www.world-nuclear.org/information-library/facts-and-figures/world-nuclear-power-reactors-and-uranium-requireme.aspx>, 2019. Accessed: 2019-05-09.
- [3] IAEA. Nuclear power plant safety. <https://www.iaea.org/topics/nuclear-power-plant-safety>, 2019. Accessed: 2019-05-16.
- [4] M. Utamura, K. Moriya, & H. Uozumi. Numerical analysis on pressure propagation in pressure suppression system due to steam bubble collapse. *Journal of Nuclear Science and Technology*, **21**(4):279, 1984.
- [5] Y. Kukita, K. Namatame, & M. Shiba. The LOCA air-injection loads in BWR Mark II pressure suppression containment systems. *Nuclear Engineering and Design*, **77**:117, 1984.
- [6] Y. Kukita, K. Namatame, I. Takeshita, & M. Shiba. LOCA steam condensation loads in BWR Mark II pressure suppression containment system. *Nuclear Engineering and Design*, **102**:225, 1987.
- [7] M. Pellegrini, L. Araneo, H. Ninokata, M. Ricotti, M. Naitoh, & A. Achilli. Suppression pool testing at the SIET laboratory: experimental investigation of critical phenomena expected in the Fukushima Daiichi suppression chamber. *Nucl. Sci. Tech.*, **53**(3):614, 2016.
- [8] I. Aya, H. Nariai, & M. Kobayashi. Pressure and fluid oscillations in vent system due to steam condensation, (I) experimental results and analysis model for chugging. *Journal of Nuclear Science and Technology*, **17**(7):499, 1980.
- [9] I. Aya & M. Kobayashi. Pressure and fluid oscillations in vent system due to steam condensation, (II) high-frequency component of pressure oscillations in vent tubes under at chugging and condensation oscillation. *Journal of Nuclear Science and Technology*, **20**(3):213, 1983.

- [10] I. Aya & H. Nariai. Boundaries between regimes of pressure oscillation induced by steam condensation in pressure suppression containment. *Nuclear Engineering and Design*, **99**:31, 1987.
- [11] M. E. Simpson & C. K. Chan. Hydrodynamics of a subsonic vapor jet in subcooled liquid. *Journal of Heat Transfer*, **104**:271, 1982.
- [12] G. Gregu, M. Takahashi, M. Pellegrini, & R. Mereu. Experimental study on steam chugging phenomenon in a vertical sparger. *International Journal of Multiphase Flow*, **88**:87, 2017.
- [13] M. Puustinen, R. Kyrki-Rajamäki, V. Tanskanen, A. Räsänen, H. Purhonen, V. Riikonen, J. Laine, & E. Hujala. BWR Suppression Pool Studies with POOLEX and PPOOLEX Test Facilities at LUT. In *The 15th International Topical Meeting on Nuclear Thermal Hydraulics (NURETH-15)*. 2013.
- [14] C. K. Chan & C. K. B. Lee. A regime map for direct contact condensation. *International Journal of Multiphase Flow*, **8**(1):11, 1982.
- [15] H. Purhonen. *Experimental thermal hydraulic studies on the enhancement of safety of LWRs*. Acta Universitatis Lappeenrantaensis 293, Lappeenranta University of Technology, 2007. ISBN 978-952-214-500-0, ISBN 978-952-214-505-5 (PDF), ISSN 1456-4491.
- [16] V. Tanskanen. *CFD modelling of direct contact condensation in suppression pools by applying condensation models of separated flow*. Acta Universitatis Lappeenrantaensis 472, Lappeenranta University of Technology, 2012. ISBN 978-952-265-221-8, ISBN 978-952-265-222-5 (PDF), ISSN 1456-4491.
- [17] V. Tanskanen, A. Jordan, M. Puustinen, & R. Kyrki-Rajamäki. CFD simulation and pattern recognition analysis of the chugging condensation regime. *Annals of Nuclear Energy*, **66**:133, 2014.
- [18] E. Hujala. *Evaluation of Bubble Formation and Break Up in Suppression Pools by Using Pattern Recognition Methods*. Master's thesis, Lappeenranta University of Technology, LUT Energy, Lappeenranta, Finland, 2013. Available online: <http://urn.fi/URN:NBN:fi-fe201304082709>.
- [19] R. Lahey & F. Moody. *The Thermal-Hydraulics of a Boiling Water Reactor*. American Nuclear Society, La Grange Park, Illinois, USA, 2. edition, 1993. ISBN: 0-89448-037-5.
- [20] S. Haukeland, B. Ivung, & T. Pedersen. BWR 90 & BWR 90+ – two advanced BWR design generations from ABB. Technical Report IAEA-SM-353/44, International Atomic Energy Agency (IAEA), 1999.
- [21] J. Joshi & A. Nayak. *Advances of Computational Fluid Dynamics in Nuclear*

- Reactor Design and Safety Assessment*. Woodhead Publishing Series in Energy. Elsevier Science, 2019. ISBN 9780081023389.
- [22] P. B. Whalley. *Boiling, Condensation and Gas-Liquid Flow*. 1987. ISBN: 9780198562344.
- [23] J. G. Collier & J. R. Thome. *Convective Boiling and Condensation*. Oxford Science Publication, Oxford, 1996. ISBN: 978-0198562962.
- [24] S. M. Ghiaasiaan. *Two-Phase Flow, Boiling and Condensation*. Cambridge University Press, 2008. ISBN: 978-0-521-88276-7.
- [25] L. Cheng & D. Mewes, editors. *Advances in Multiphase Flow and Heat Transfer*, volume 4. Bentham Science, 2012.
- [26] C. H. Song, S. Cho, & H. S. Kang. Steam jet condensation in a pool: from fundamental understanding to engineering scale analysis. *Journal of Heat Transfer*, **143**, 2012.
- [27] N. I. Kolev. *Multiphase Flow Dynamics 1*. Springer, 2011. ISBN: 978-3-642-20604-7.
- [28] I. Gallego-Marcos, W. Villanueva, & P. Kudinov. Modelling of pool stratification and mixing induced by steam injection through blowdown pipes. *Annals of Nuclear Energy*, **112**:624, 2018.
- [29] V. Tanskanen, E. Hujala, & M. Puustinen. Numerical simulation and analysis of PPOOLEX DCC-05 chugging test. Technical report, Lappeenranta University of Technology, School of Energy Systems, Nuclear Engineering, 2014.
- [30] P. C. C. P. Software. *version 2.2.737.0*. Vision Research Inc., Wayne, New Jersey, USA, 2013.
- [31] MATLAB. *version 8.6 (R2015b)*. The MathWorks Inc., Natick, Massachusetts, USA, 2015.
- [32] N. Otsu. A threshold selection method from gray-level histograms. *IEEE Transactions on Systems, Man, and Cybernetics*, **9**(1):62, 1979.
- [33] S. Bangare & S. Patil. Reviewing Otsu's method for image thresholding. *International Journal of Applied Engineering Research*, **10**(9):21777, 2015.
- [34] MATLAB. *version 9.2 (R2017a)*. The MathWorks Inc., Natick, Massachusetts, USA, 2017.
- [35] G. Windreich, N. Kiryati, & G. Lohmann. Voxel-based surface area estimation: From theory to practice. *Pattern Recognition*, **36**:2531, 2003.

- [36] E. Hujala, V. Tanskanen, & J. Hyvärinen. Frequency analysis of chugging condensation in pressure suppression pool system with pattern recognition. *Nuclear Engineering and Design*, **339**:244, 2018.
- [37] E. Hujala, V. Tanskanen, & J. Hyvärinen. Pattern recognition algorithm for analysis of chugging direct contact condensation. *Nuclear Engineering and Design*, **332**:202, 2018.
- [38] M. Giaquinta & G. Modica. *Mathematical Analysis: Foundations and Advanced Techniques for Functions of Several Variables*. Birkhäuser, 2012. ISBN: 978-0-8176-8309-2.
- [39] C. Brennen. *Cavitation and Bubble Dynamics*. 1st edn. Cambridge University Press. ISBN 978-1-107-64476-2, 2014.
- [40] M. Ishii & T. Hibiki. *Thermo-Fluid Dynamics of Two-Phase Flow*. 2nd edn. Springer Science+Business Media. ISBN 978-1-4419-7984-1, e-ISBN 978-1-4419-7985-8, 2011.
- [41] P. Coste. Computational simulation of multi-d liquid-vapor thermal shock with condensation. In *Proceedings of ICMF04, Yokohama, Japan*. 2004.
- [42] M. Pellegrini, M. Naitoh, C. Josey, & E. Baglietto. Modeling of Rayleigh-Taylor instability for steam direct contact condensation. In *The 16th International Topical Meeting on Nuclear Reactor Thermal Hydraulics (NURETH-16), Chicago, IL, August 30-September 4*, p. 15. 2015.
- [43] P. Coste. A large interface model for two-phase CFD. *Nuclear Engineering and Design*, **255**:38, 2013.
- [44] K. Tielinen, A. Räsänen, E. Kotro, & I. Saure. General description of SEF-POOL test rig. Technical report, Lappeenranta University of Technology, Nuclear Safety Research Unit, 2017.
- [45] P. C. C. P. Software. *version 3.3.781.0*. Vision Research Inc., Wayne, New Jersey, USA, 2018.
- [46] J.-Y. Tinevez. *Simple Tracker, version 1.5.0.0*. Matlab Central File Exchange, Retrieved 17 February 2019, <https://se.mathworks.com/matlabcentral/fileexchange/34040-simple-tracker>, 2019.
- [47] I. Gallego-Marcos. *Steam condensation in a water pool and its effect on thermal stratification and mixing*. Ph.D. thesis, KTH, Sweden, 2018. Retrieved from <http://urn.kb.se/resolve?urn=urn:nbn:se:kth:diva-238732>.
- [48] E. J. Garboczi. Three-dimensional mathematical analysis of particle shape using X-ray tomography and spherical harmonics: Application to aggregates used in concrete. *Cement and Concrete research*, **32**:1621, 2002.

-
- [49] D. Wei, J. Wang, & B. Zhao. A simple method for particle shape generation with spherical harmonics. *Powder Technology*, **330**:284, 2018.

Publication I

E. Hujala, V. Tanskanen and J. Hyvärinen
**Pattern recognition algorithm for analysis of chugging direct contact
condensation**

Reprinted with permission from
Nuclear Engineering and Design,
Vol. 332, pp. 202-212, 2018
© 2018, Elsevier B.V.



Contents lists available at ScienceDirect

Nuclear Engineering and Design

journal homepage: www.elsevier.com/locate/nucengdes

Pattern recognition algorithm for analysis of chugging direct contact condensation

Elina Hujala^{*}, Vesa Tanskanen, Juhani Hyvärinen

LUT School of Energy Systems, Nuclear Engineering, Lappeenranta University of Technology (LUT), P.O. Box 20, FIN-53851 Lappeenranta, Finland

A B S T R A C T

Direct contact condensation of steam bubbles in a boiling water reactor suppression pool has long been studied utilizing video recording of experiments. The use of video recording enables observation of the behaviour of the bubble surface area and can assist in validation of computational fluid dynamics models.

A direct contact condensation experiment of the suppression pool test facility PPOOLEX was recorded using high-speed cameras. The recorded video material was used for development of a pattern recognition and data analysis algorithm. 300 fps video of 48 s duration was cut into frames with a resolution of 768 px × 768 px. The side profile of the bubbles was identified and the volumes and surface areas of the bubbles were evaluated using a voxel-based method.

The purpose of the algorithm was to determine the shape and size of steam bubbles during their formation, expansion, collapse and re-formation. The most probabilistic chugging frequencies were estimated. The bubble geometry data were also used to determine the velocity and acceleration of the phase interface, as condensation induced Rayleigh-Taylor instability develops on the bubble surface during the bubble collapse, as the heavy phase accelerates towards the light phase. Knowledge of the critical wave length is necessary for mesh spacing in CFD calculations.

The algorithm appears to be promising. Some limitations exist and approximations need to be made due to the challenging video shooting conditions. The algorithm works well for cylindrical bubbles and provides important data on the dynamics of the phase interface necessary for numerical modelling of direct contact condensation.

1. Introduction

Direct contact condensation (DCC) of saturated steam in subcooled water can cause rapid pressure transients and accelerate the liquid to high velocity, leading to high dynamic loads on surrounding structures. These loads are encountered in many engineered systems e.g. in the form of instantaneous water hammer in pipes or as periodic condensation oscillations of submerged steam injections. DCC is, however, an essential phenomenon in certain nuclear engineering applications such as steam-driven water injection systems and suppression pools.

Liquid phase turbulence near the gas-liquid interface and available interfacial area determine the DCC heat transfer coefficient. DCC is controlled by the liquid heat on the liquid side and by surface pollutants such as non-condensable gases on the gas side. The conduction dominated boundary layer on the liquid side can be thin, and heat transfer from the interface is controlled mainly by turbulent convection, i.e., eddies. Thus, a valid liquid side heat transfer correlation is the most important part when modelling DCC in mildly sheared and lowly

subcooled stratified flows. However, if the subcooling is high and the interface is wavy or unstable, as on a bubble in a liquid, the interfacial area modelling has increased importance in the heat transfer solution. This importance is not only due to the increased heat transfer area in such conditions, but also due to the interface motion, which is two-way coupled with the liquid side turbulent heat transfer mechanism. That is, a higher DCC heat transfer rate causes suction on the interface, reshaping it and increasing the interfacial area. Waviness and other interfacial instabilities play a significant role in determining the rate of interfacial area increase and the eddy size in the liquid side.

DCC of steam bubbles has long been an important research subject in study of boiling water reactor (BWR) suppression pools. In order to prevent pressure build-up, it can be essential to condense a large amount of steam rapidly, e.g., during a loss of coolant accident (LOCA) or safety relief valve operation. DCC is the most rapid and straightforward means to achieve rapid condensation. In BWR suppression pools, saturated steam is discharged through large submerged vent pipes into a deeply subcooled mass of water. In such a case, the condensation mass

^{*} Corresponding author.

E-mail address: Elina.Hujala@lut.fi (E. Hujala).

<https://doi.org/10.1016/j.nucengdes.2018.03.032>

Received 28 July 2017; Received in revised form 16 March 2018; Accepted 20 March 2018

Available online 28 March 2018

0029-5493/ © 2018 Elsevier B.V. All rights reserved.

Nomenclature			
<i>Variables</i>		v	velocity
a	acceleration	V	volume
A	surface area	\mathbf{V}	vertex array
d	size of a one pixel	y	distance
d_i	number of nonzero elements of a row	$ Y(f) $	absolute value of amplitude
f	frequency	<i>Subscripts</i>	
FS	frame rate	i	index
\mathbf{F}	face array	l	liquid (water)
h_i	height	s	element
λ_c	critical wavelength	v	vapour (steam)
λ_m	predominant wavelength	<i>Abbreviations</i>	
M_i	number of pixels	BWR	boiling water reactor
n	image number	CFD	computational fluid dynamics
N	total number of images/cylinders	DCC	direct contact condensation
r_i	radius	FFT	fast Fourier transform
$r_{i,s}$	vertices	fps	frames per second
ρ_l	density of liquid	LOCA	loss of coolant accident
ρ_v	density of vapour	PACTEL	parallel channel test loop
S	patch area	PIV	particle image velocimetry
σ	surface tension	(P)POOLEX	condensation pool experiments
t	time	WMS	wire-mesh sensor
\mathbf{v}_i	vertex vector		

flow rate is high, and it is possible that the pressure decrease within the lighter phase causes interfacial accelerations higher than the acceleration of gravity. Interfacial accelerations of order of $100\text{--}1000\text{ ms}^{-2}$ magnitude have been observed in suppression pool cases (Patel et al., 2017). Such high accelerations invoke interfacial instabilities, i.e., Rayleigh-Taylor (Strutt, 1883; Taylor, 1950), Kelvin-Helmholz (Drazin, 2002) and Richtmyer-Meshkov (Richtmyer, 1960; Meshkov, 1969; Brouillette, 2002) instability, which cause roughening of the steam-

water interface. Interface roughening increases heat transfer rate (Brennen, 2014), and thus also condensation heat transfer rate should increase temporarily. This recurrently increasing interfacial area together with high turbulence cause condensation oscillations and a phenomenon called chugging. In consequence, the steam injected to the pool causes high dynamic loads on the walls and internal structures. Due to the rapid movement of the phase interface, direct measurement of heat and mass transfer is impossible during chugging with existing

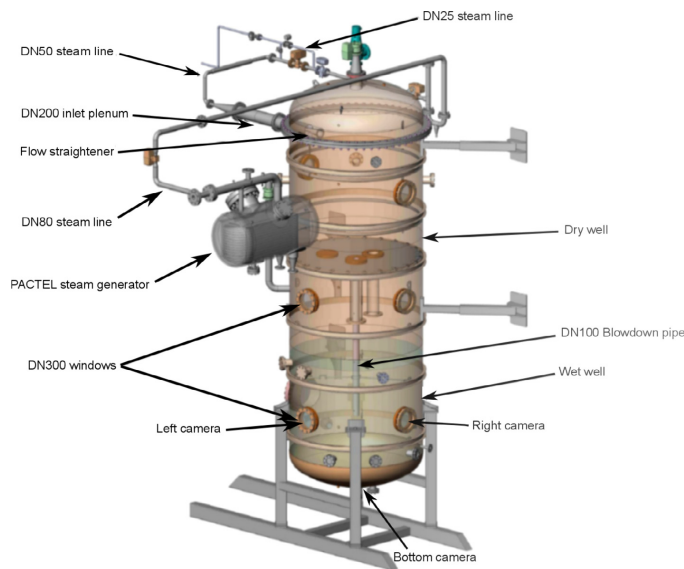


Fig. 1. PPOOLEX test facility. Locations of the high-speed cameras are also marked.

techniques. However, DCC model validation against experiments becomes possible if the time evolution of the phase interface - its size and shape - can be determined.

As DCC has a major role in nuclear power plant safety, test facilities – small (Aya et al., 1980; Aya and Kobayashi, 1983; Aya and Nariai, 1987; Simpson and Chan, 1982; Gregu et al., 2017) and large (Motoaki Utamura and Uozumi, 1984; Kukita et al., 1984; Kukita et al., 1987; Pellegrini et al., 2016) – have been used to study condensation modes. The experimental results have been used for improvement and validation of different condensation models of computational fluid dynamic (CFD) codes (Patel et al., 2017; Mimouni et al., 2011). Validation of CFD models for two-phase flows often requires measurement techniques that are currently not feasible (Bestion, 2014). In the case of DCC, some of these challenges can be addressed by using video recording of the experiments, analyzing the recorded films and comparing results to the simulations. Movie cameras or, more recently, modern high-speed cameras, have been utilized to record experiments (Chan and Lee, 1982; Issa et al., 2014). For decades, only ocular investigations of video material of condensing bubbles were mostly used to compare the results of the system codes, CFD models and simulations (Chan and Lee, 1982; Aust et al., 1983). Moreover, the analysis methods and findings of the ocular estimations were not reported extensively. Recently, however, more systematic means to take advantage of the video material have become more popular, see e.g. (Issa et al., 2014).

A preliminary pattern recognition algorithm has been presented for the former BWR suppression pool model, POOLEX test facility (Tanskanen et al., 2014b). The aim of the algorithm was to evaluate the size distribution and chugging frequencies of steam bubbles. The limited length of the available high-speed video material samples resulted in standard 25 fps samples having to be used for algorithm development.

This current study presents an updated pattern recognition and data analysis algorithm for a direct contact condensation mode called chugging by making use of high-speed cameras and improved resolution images. The algorithm is based on experiments with the present-day pressurised suppression pool model, the PPOOLEX test facility. The aim of the study is to increase knowledge of DCC of steam bubbles. The algorithm estimates the change of volumetric and surface area distributions of the condensing steam bubbles and determines the velocities and accelerations of growing and collapsing bubbles. Additionally, chugging frequencies and surface instabilities are investigated in frequency analysis of the algorithm output.

2. PPOOLEX DCC-05 experiment

2.1. PPOOLEX test facility

The PPOOLEX test facility is a scaled thermal hydraulic model of a Nordic-type BWR suppression pool. It is a 31 m³ stainless steel vessel of 2.4 m diameter which consists of two parts: a wet well compartment (suppression pool) and a dry well compartment, separated by an intermediate floor, an inlet plenum and air/steam line piping. A route for air/steam flow from the dry well to the wet well is created by a vertical blowdown pipe attached non-axisymmetrically underneath the floor. The length and width of the blowdown pipe can be changed depending on the needs of the ongoing experiment. The assembly of the PPOOLEX test facility is shown in Fig. 1.

Steam needed in the experiments is produced with the PACTEL test facility, which has three steam generators and a heating power of 1 MW at the core section. The facility can be used to model various thermal hydraulic phenomena, such as steam bubble condensation and gas bubble propagation in suppression pools, structural loads caused by rapid condensation and the effect of non-condensable gases on emergency core cooling strainer behaviour. A more detailed description of the PPOOLEX test facility is presented in Puustinen et al. (2013).

2.2. DCC-05 experiment

The PPOOLEX DCC-05 test was a part of a direct contact condensation test program. The main purpose of DCC-05 was to obtain measurement data for validation of the DCC models used in CFD modelling of chugging and to make a high-speed video recording for use in development work of a pattern recognition algorithm (Tanskanen et al., 2014a; Hujala et al., 2013). The pool water temperature rise was kept as low as possible in the DCC-05 test in order to study only the effect of the variable steam flow rate. The suppressed temperature increase was achieved by minimizing the steam injection during waiting times due to flow rate adjustments and camera data transfer processes. Before the experiment the wet well pool was filled with water at 298 K so that the blowdown pipe outlet was submerged by 1.05 m and the dry well was filled with air at atmospheric pressure. A DN100 stainless steel blowdown pipe was used in the experiment. The experiment was started with a clearing phase during which the structures were heated to prevent wall condensation and non-condensable air was removed from the dry well as much as possible. This was achieved by using a

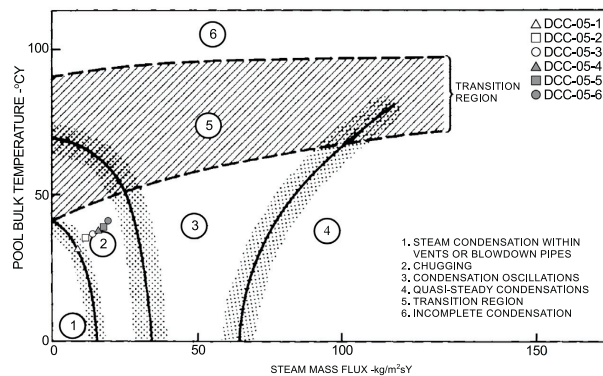


Fig. 2. Steam blows of the DCC-05 experiment on the condensation mode map by Lahey and Moody (1993). Chugging was the dominant DCC mode during the DCC-05 test.

high steam flow rate ($320\text{--}340\text{ gs}^{-1}$) blow for 500 s, filling the dry well with steam and pushing the air to the wetwell gas space. Pool temperature rose to 303 K during this process (Tanskanen et al., 2014a). The valid part of the experiment following the clearing phase consisted of six runs with increasing flow rates between 75 gs^{-1} and 200 gs^{-1} . Pool temperature rose gradually to 313 K during these blows. The individual steam blows of the DCC-05 experiment defined by the steam mass flux and pool bulk temperature are in region 2 of the condensation mode map by Lahey and Moody (1993) presented in Fig. 2.

The DCC-05 test consisted of six runs with different flow rates, named (DCC-05-1–DCC-05-6), with total length of 52 min. Each run had its own challenges with image quality. Lighting conditions caused blurred overexposed edges of the bubbles and, alternatively, shadowed edges. Swarms of small bubbles created bright additional objects, and transparent large bubbles were hard to recognize. Different issues hampering bubble image processing are presented in Fig. 3. This paper concentrates on test DCC-05-4, whose recorded video material appeared to have the best quality.

Test facility instrumentation comprised three Phantom Miro M/R/LC110 high-speed cameras with 24 mm f1.8-22 lenses operating at a framerate of 300 fps. 300 fps was chosen due to the limited recording capacity and because it allowed a longer recording time. One camera was recording at the bottom of the pool, under the blowdown pipe, and the two others were recording from the side of the pool, almost perpendicularly to each other (see Fig. 1). Various thermocouples and pressure transducers recorded numerical data within the pool and blowdown pipe and stress strain sensors at the pool bottom. A typical view from each camera is shown in Fig. 4.

Further information of the DCC-05 experiment is documented in Puustinen et al. (2014).

3. Pattern recognition and data analysis algorithm

3.1. Development of the algorithm

The main purpose of the pattern recognition algorithm was to

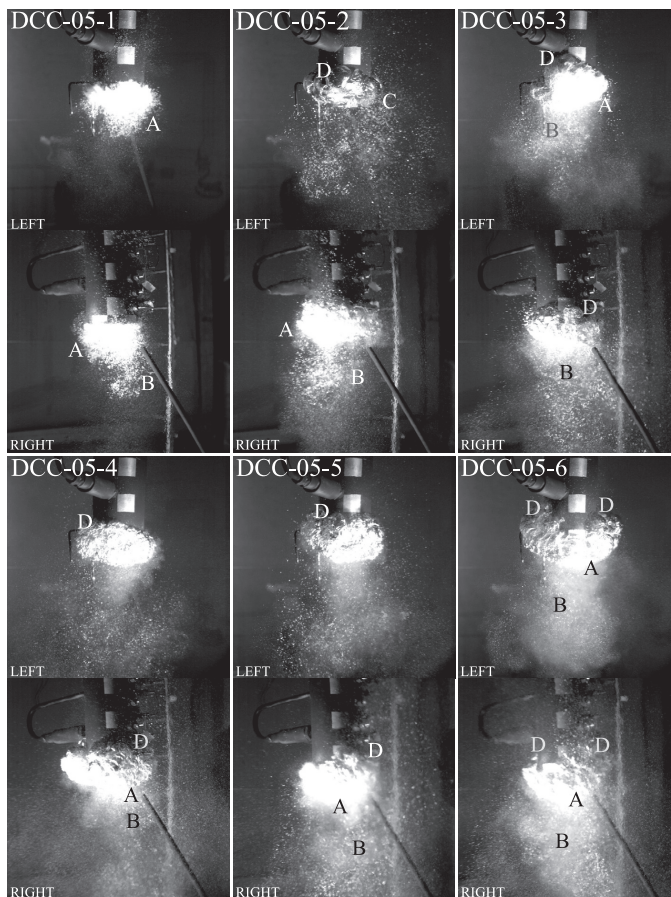


Fig. 3. Challenges in image processing of different runs DCC-05-1–DCC-05-6 using left and right cameras. (A) Blurred overexposed edge of the bubble, (B) bright swarms of small bubbles, (C) transparent, hard to recognize bubbles, and (D) shadowed edges of the bubbles were the most common challenges during the DCC-05 experiment. Camera: Phantom Miro M/R/LC110 with 24 mm lens at an aperture of f2.4 at a framerate of 300 fps.

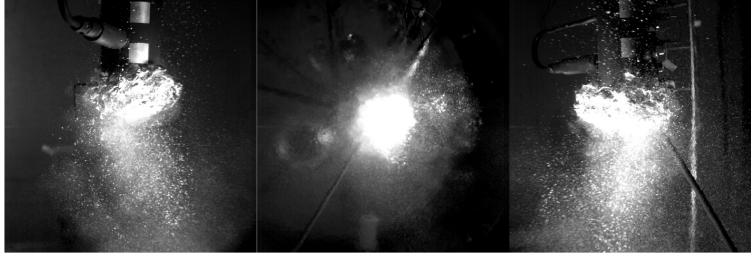


Fig. 4. Typical frames from left, bottom and right side cameras. $t = 45.72$ s, estimated volume $V = 3256$ cm³ and surface area $A = 1696$ cm².

improve knowledge of the effects of DCC during chugging in suppression pools. The goal was to evaluate the volumetric size distribution, average surface area, velocity and acceleration of the condensing steam bubbles and their chugging frequencies and investigate transport processes at the bubble surface area. The different stages of average-size steam bubble growth and collapse are presented in Fig. 5.

The image processing functions of MATLAB software (MATLAB, 2017) were used for construction of the pattern recognition and data analysis algorithm. The first version of the pattern recognition algorithm was introduced earlier in Hujala (2013) and Hujala et al. (2013). The basic operation of the algorithm is presented as a flow diagram in Fig. 6.

The video sample recorded during the DCC-05-4 test was cut into frames. The resolution of each frame was 768×768 pixels. From every frame, an empty background image was removed in a way that only the changes - the bubbles - remain. Disturbing bright objects such as reflecting structures of the facility were removed. The boundaries of the bubbles were then identified from black-and-white images. An example of identified bubble boundaries is presented in Fig. 7. An animation of the pattern recognition process is available in the Supplementary Material of the online version of this article.

As the right-side camera images were noticed to be of poor quality, as shown earlier in Fig. 3, due to blurred, overexposed or shadowed edges and large swarms of small bubbles between the pipe and the camera, images from the right-side camera were not utilized further. A part of bubble shape information was lost due to the absence of images from this camera. Fortunately, the bottom camera data indicated that the bubbles were symmetrically rounded during the DCC-05 test. For this reason, the data of the single side camera was considered to be a sufficient representation of the chugging bubbles in this case. The side profile of the bubbles were known to be arbitrary shaped, e.g., flat, round or semi-circular. A voxel-based method has been used successfully to evaluate the surface of brain images (Windreich et al., 2003), and brain images are known to be arbitrary shaped, and this approach was thus selected for evaluation of the bubble volumes. Fitting of ellipses to the images and evaluating the volume of a spheroid would have been an alternative solution for evaluation of the shape and size of the bubbles (Tanskanen et al., 2014b).

The identified bubbles were processed row by row. Recognized binary images contained only a white side profile of a bubble in a black background. The number of nonzero elements - that is to say, white pixels - of every row was calculated and the center of mass evaluated. The line with height of one pixel was rolled over to its center of mass, which produced a cylindrical plate. The sum of the cylindrical plates of each nonzero row gives the volume V of the bubble in voxels:

$$V = \sum_{i=\text{firstrow}}^{\text{lastrow}} \pi \left(\frac{d_i}{2} \right)^2 h_i \quad (1)$$

where d_i is the number of nonzero elements in the i^{th} row and h_i is the height of a row.

Calculating the surface area A from the sphere made using voxels overestimates the surface area significantly, so smoothing of the sharp edges was carried out.

The surface of a bubble was created using an isosurface function which extracts isosurface data - faces F and the vertices V - in separate arrays from volume data. From vertex array V , triangle vertices r_1 , r_2 and r_3 were created:

$$r_{1,s} = V(F(s,1),:) \quad (2)$$

$$r_{2,s} = V(F(s,2),:) \quad (3)$$

$$r_{3,s} = V(F(s,3),:) \quad (4)$$

where s is the s^{th} element of the face array F . The vectors v_1 and v_2 from vertices 1, 2 and 3 are:

$$v_1 = r_2 - r_1 \quad (5)$$

$$v_2 = r_3 - r_1 \quad (6)$$

Vectors v_1 and v_2 delimited the parallelogram as shown in Fig. 8.

The surface area A of the bubbles can be calculated using these parallelograms as:

$$A = \sum_{i=1}^s (S_{i-1} + 0.5 \cdot |v_{1,i} \times v_{2,i}|) \quad (7)$$

where S_{i-1} is the area of each patch, half of the area of the parallelogram and $S_0 = 0$. Spheres with radius of $r = 10$ pixels constructed using voxels and cylindrical plates with and without a smooth isosurface are presented in Fig. 9.

The axial velocity and acceleration of the condensing bubbles were estimated using a box ratio method (Hujala, 2013). In this method, just a thin region of interest is considered as shown in Fig. 10. A rectangle of width 35 pixels (≈ 2.78 cm) and height of 344 pixels (≈ 27.3 cm) was selected in the middle of the blowdown pipe outlet in a way that its

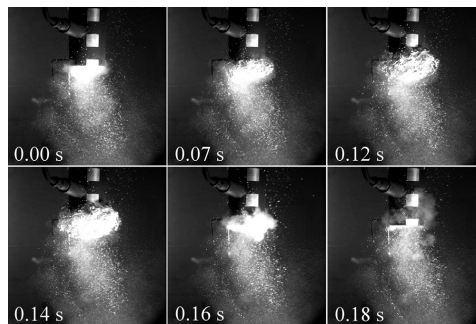


Fig. 5. Expansion and collapse of a bubble during the DCC-05-4 test.

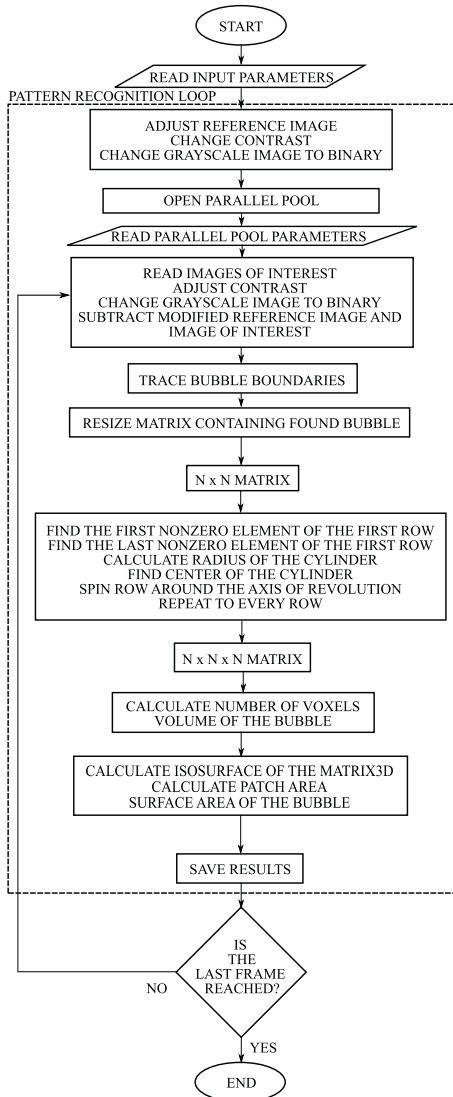


Fig. 6. Simplified flow diagram of the pattern recognition algorithm.

upper border was at the outlet of the pipe. The change in the lower border of the bubbles was investigated and the average fluctuation of the bubbles recorded.

The velocity $v(n)$ and acceleration $a(n)$ in the image of interest n at framerate F_s were evaluated using forward difference as presented in Eqs. (8) and (9) respectively. N is the total number of images.

$$v(n) = \begin{cases} F_s(-y(n+1)-(-y(n))), & \text{when } n = 1 \\ \frac{F_s}{2}(-y(n+1)-(-y(n-1))), & \text{when } 2 \leq n \leq N \end{cases} \quad (8)$$

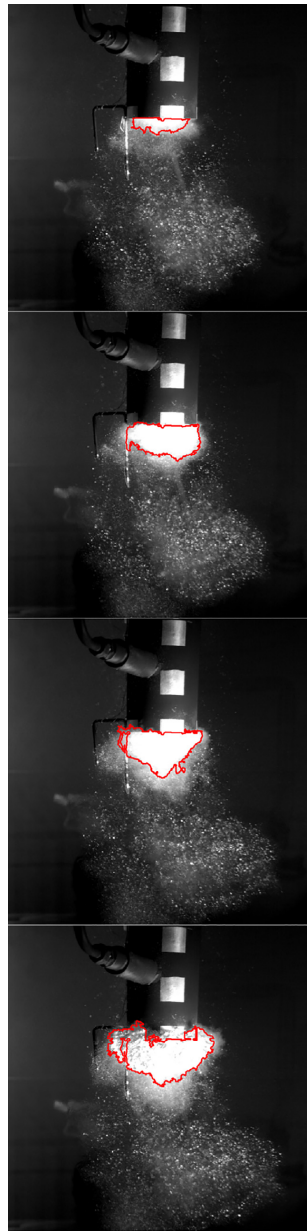


Fig. 7. Pattern recognition process. Identified bubble boundaries are marked as red. Some errors of recognition can be seen at the top of the bubble, near to the outlet of the blowdown pipe.

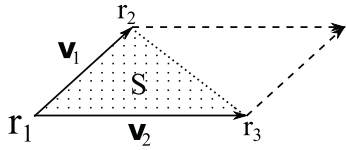


Fig. 8. Calculation of the surface area. Triangle vertices r_1 , r_2 and r_3 . Vectors v_1 and v_2 define the parallelogram. A patch S (dotted area) is an area of a triangle defined by the vectors, which is half of the area of the parallelogram.

$$a(n) = \begin{cases} Fs^2(-y(n+2)-2(-y(n+1)) + (-y(n))), & \text{when } n = 1 \\ Fs^2(-y(n+1)-2(-y(n)) + (-y(n-1))), & \text{when } 2 \leq n \leq N \end{cases} \quad (9)$$

In this study, only the vertical direction of the velocity and acceleration has been evaluated; evaluation will be extended to other directions in future work.

The chugging frequency, i.e. the frequency at which periodic chugging condensation oscillations occur, has been a topic of interest in fluid oscillation measurement since the 1970s (Aya et al., 1980). The transient volume data produced by the algorithm makes it possible to evaluate the most probabilistic chugging frequencies using fast Fourier transform (FFT).

3.2. Error estimation

Due to the challenging camera set-up in the test, many approximative actions had to be included in the pattern recognition algorithm to analyse the data. The number and size of the observation windows were limited in the test facility in order to maintain its ability to withstand large dynamical loads. Thus, the three high-speed cameras were put in places which already existed instead of drilling new windows in the facility walls. In the blowdown experiments with the DN100 blowdown pipe, the bubbles can be said to be axisymmetric but still closer to knobly ellipsoids than spheres. Also the halogen lamp lighting of the PPOOLEX test facility is challenging and a part of the bubbles are always lost. Lighting limitations made the right-side camera images so blurry - due to the large swarms of small bubbles and the blurriness of the stratified warm water between the camera and the pipe - that the frames could not be used. The same problem was found with the bottom camera. Therefore, cylinder plates were chosen for the evaluation of the bubble volume even though their use could lead to larger errors with non-rounded bubbles.

Relative error of the volume of the cylinder has been calculated as follows. Eq. (1) constructed the volume of the bubble using cylinder plates. Radius r_i of the cylinder is calculated in pixels M_i and converted

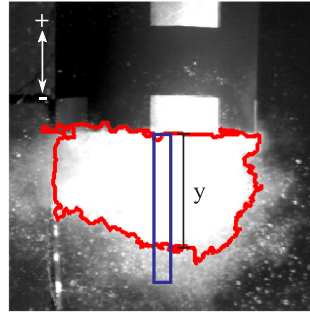


Fig. 10. Evaluation of the y -distance for velocity and acceleration calculations. The blue rectangle represents the ratio box (not in scale). In every image n , the average of the y -distance inside the rectangle was measured and velocity $v(n)$ and acceleration $a(n)$ evaluated using the forward difference method.

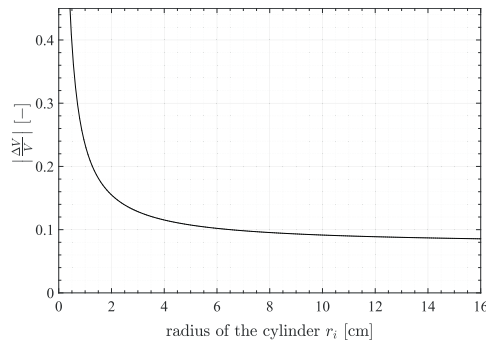


Fig. 11. Relative error of the volume of the cylinder for different cylinder radii. The error drops under the 10 % with radii larger than 6.5 cm (≈ 82 px).

to metric units by multiplying pixels by the size of one pixel d . Using the radius of the cylinder, the total volume of the bubble is:

$$V = \sum_{i=1}^N \pi r_i^2 h_i \quad (10)$$

where N is the total number of the cylinders, and r_i and h_i are the radius

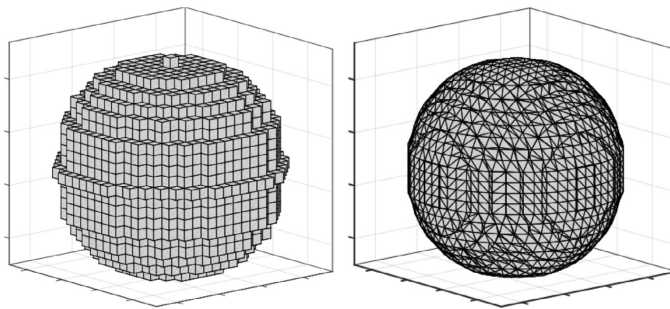


Fig. 9. Spheres with radius of $r = 10$ px created using the voxel-based method (left). At right, the same sphere after use of the isosurface function and smoothing for evaluation of the surface area.

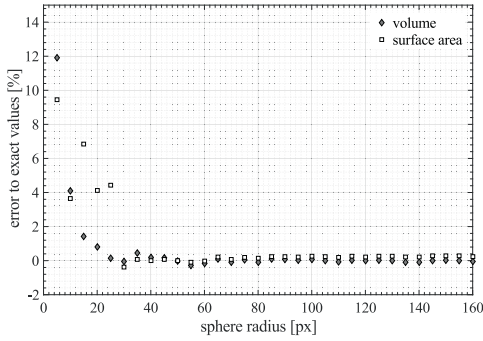


Fig. 12. Volume and surface area errors of hypothetical spheres, produced using the algorithm for circles with different radii r_i , compared to exact values of theoretical spheres $V_{\text{sphere}} = \frac{4}{3}\pi r_i^3$ and $A_{\text{sphere}} = 4\pi r_i^2$.

and height of the cylinder i respectively. Height is always a size of one pixel ($h_i = d$) and the radius is a pixel multiplied by the number of pixels M_i ($r_i = M_i d$).

$$V = \sum_{i=1}^N \pi (M_i d)^2 d = \pi d^3 \sum_{i=1}^N M_i^2 \quad (11)$$

The uncertainty of N is assumed to be zero. The error estimation for the volume V using the total differential is:

$$\left| \frac{\Delta V}{V} \right| \leq \frac{1}{V} \left(\left| \frac{\partial V}{\partial d} \right| |\Delta d| + \sum_{i=1}^N \left| \frac{\partial V}{\partial M_i} \right| |\Delta M_i| \right) \quad (12)$$

The uncertainty of M_i is assumed to be constant, i.e. $\Delta M_i = \Delta M$, thus

$$\frac{\Delta V}{V} \leq \frac{3\Delta d}{d} + \frac{2\Delta M \sum_{i=1}^N M_i}{\sum_{i=1}^N M_i^2} \quad (13)$$

When the error of the size of one pixel is $\Delta D = 2 \cdot 10^{-3}$ cm and the size of one pixel is $D = 79.4 \cdot 10^{-3}$ cm, and the error of the number of pixels is $\Delta M = 1$, the relative error of the volume of the cylinders $\left| \frac{\Delta V}{V} \right|$ for different cylinder radii is as presented in Fig. 11.

Relative error less than 10 % for volume with radii larger than 6.5 cm is suitable, if it is taken into account that the error can be decreased by increasing the resolution of the images or zooming the camera in future experiments.

Relative error of the surface area by using cylinder plates is

practically unfeasible to calculate analytically, but it can be estimated using hypothetical spheres produced using the algorithm and comparing them to theoretical values of the volume and surface area of spheres with the same radii. Hypothetical synthetic spheres created using the pattern recognition algorithm were introduced in Fig. 9. When comparing evaluated hypothetical synthetic sphere volume, Eq. (1), and surface area, Eq. (7), with different sphere radii r_i to theoretical values of the sphere volume $V_{\text{sphere}} = \frac{4}{3}\pi r_i^3$ and to the surface area $A_{\text{sphere}} = 4\pi r_i^2$, the errors drop under 1 %, if the radius of the sphere is more than 30 px (≈ 2.4 cm) as shown in Fig. 12.

The nearer the steam bubbles are to pure spheres, the better is the performance of the pattern recognition algorithm and the more accurate the volumetric and surface area estimations. Combining the above errors together, it can be said that the algorithm is suitable for estimation of the temporal volumetric and area changes of the steam bubbles as the effect of systematic errors diminish even further in transient study.

4. Results

The DCC-05-4 experiment was investigated using the pattern recognition and data analysis algorithm. A total length of 48 s of video material was recorded. At a framerate of 300 fps, a total of 14426 frames were stored. Evaluated surface areas and volumes of the bubbles during the experiment are presented in Fig. 13.

Estimated surface area varies between 0.05 m^2 to 0.2 m^2 . The volumes of the largest bubbles are near to 4 dm^3 . The distance between the surface of the bubble and the blowdown pipe outlet in the y -direction, the estimated velocity and the vertical acceleration of the bubbles evaluated as described in Chapter 3.1 are shown in Fig. 14.

The largest bubbles reached -0.15 m below the blowdown pipe during expansion with a velocity of -3 ms^{-1} and then condensed with a velocity as high as 4.5 ms^{-1} . The acceleration between the growth and break up of the bubble exceeds almost 2000 ms^{-2} . A closer view of acceleration data is presented in Fig. 15.

The velocity and acceleration values are crucial when choosing nodalization resolution and interfacial area density models for Eulerian two-fluid CFD simulations of chugging cases (Patel et al., 2017). The commonly used interfacial area density calculated from the gradient of the void fraction yields effectively the minimum surface area allowed by the nodalization density (Pellegrini et al., 2015). Interfacial details smaller than the node size are filtered out if no additional sub-grid scale interfacial area density models are included. Interfacial area increase due to interfacial instabilities can reach almost arbitrarily high values, but a preliminary maximum for node size can be assumed to be at least less than the critical wave length for the Rayleigh-Taylor instability (Patel et al., 2017). However, better results can be obtained by decreasing node size further. Critical wavelength λ_c is:

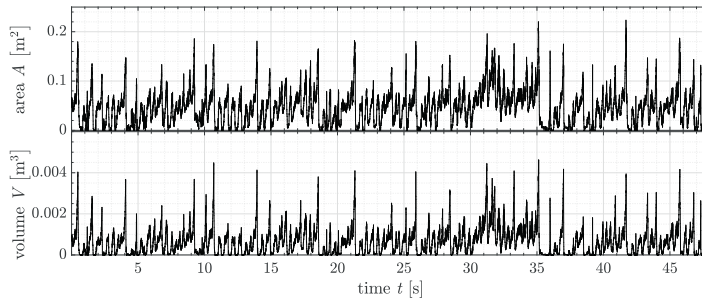


Fig. 13. Estimated surface areas A (top) and volumes V (bottom) of the bubbles during the DCC-05-4 experiment using pattern recognition algorithm.

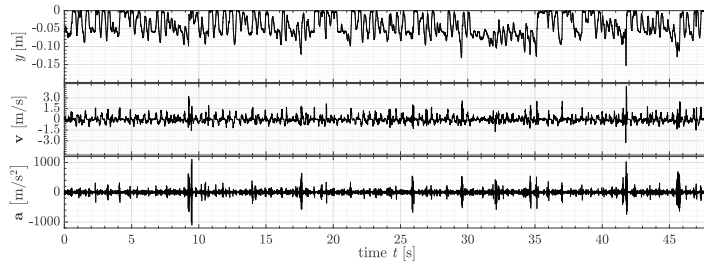


Fig. 14. Distance between the bubble surface and blowdown pipe outlet y (top), velocity of the bubble growth and collapse v (middle) and the vertical acceleration of growing and collapsing bubbles a (bottom) during the DCC-05-4 experiment.

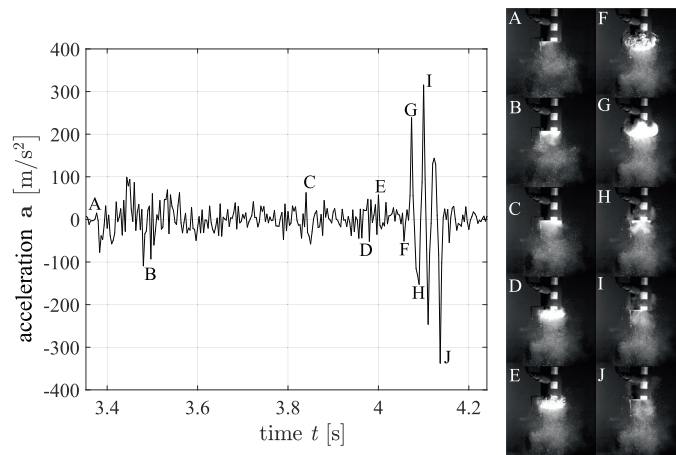


Fig. 15. Short sample of acceleration data and related bubble modes A to J.

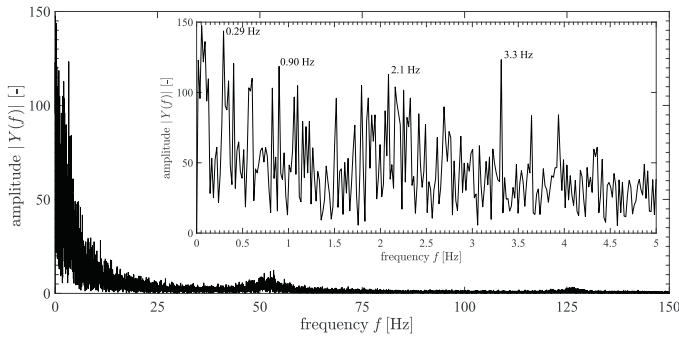


Fig. 16. FFT of the DCC-05-4 volume data. The most probable chugging frequencies f were estimated as between 0.29 Hz to 3.3 Hz. $|Y(f)|$ is an absolute value of an amplitude of each frequency f and t is time.

$$\lambda_c = 2\pi \sqrt{\frac{\sigma}{a(\rho_l - \rho_v)}} \tag{14}$$

where σ is the surface tension, a is the acceleration, ρ_l is the density of the water and ρ_v is the density of the steam (Ishii and Hibiki, 2011). High acceleration due to chugging limits the node size in CFD

simulations to 1.0 mm–1.3 mm ($a = 1100 \text{ ms}^{-2}$, $p = 3.1 \text{ bar}$) in the DCC-05-4 case. At the same time, predominant wavelength λ_m :

$$\lambda_m = 2\pi \sqrt{\frac{3\sigma}{a(\rho_l - \rho_v)}} \tag{15}$$

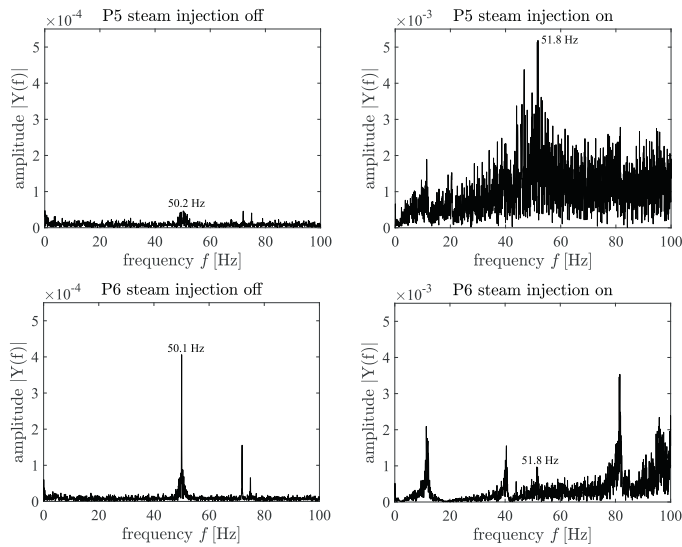


Fig. 17. Pressure transducers p_5 and p_6 FFTs without steam injection (left) and with steam injection (during the experiment) (right). The amplitudes $|Y(f)|$ are made comparable by limiting sample length. Notice the tenfold difference between the amplitudes.

is 1.7 mm–2.4 mm.

The chugging frequencies were acquired using FFT for the volume data. The FFT image is shown in Fig. 16.

The frequencies are concentrated at low frequencies, but two higher frequencies are also visible, around 53.4 Hz and 126.4 Hz. The low frequencies $0.6 \text{ Hz} \pm 0.3 \text{ Hz}$ and around 2.1 Hz can be confirmed to be very near the chugging frequencies seen also with ocular investigation. In ocular investigation, the video material was reviewed frame by frame and the frequencies calculated manually.

The possible effect of electric grid noise was studied comparing FFT of the pressure transducer data during the experiment (steam injection on) to the data without steam injection by making FFT amplitudes comparable. Two pressure transducers in different places were compared. Pressure transducer p_5 was in the pool water, 5 cm away from the blowdown pipe outlet, and pressure transducer p_6 was at the bottom of the suppression pool. FFTs of the pressure transducer data with and without the steam injection are shown in Fig. 17.

When the steam injection is off, the pressure transducer p_6 at the bottom of the pool shows a high, sharp signal from the electric grid ($50.0 \pm 0.1 \text{ Hz}$ (lower left in Fig. 17)), whereas at the middle of the pool, 5 cm from the blowdown pipe outlet, the grid signal blends into the noise in pressure transducer p_5 (top left in Fig. 17). When the steam injection is on, the noise of the electricity grid has to vanish in the measured signal, because its amplitude is tenfold lower than pressure oscillations during chugging.

5. Discussion

Despite numerous approximations made in the pattern recognition algorithm, the data acquired from the transient phenomena match visual observations of the oscillation frequency. Systematic errors have no significant effect on the final analyses, which are based mostly on the values obtained by differentials of location, i.e. velocity, acceleration and volume/area change rate in FFT. The fluctuation of the bubble volume and surface area can be recorded reliably. The relative error of the volume can be decreased by increasing the resolution of the images

or zooming the camera in future experiments.

The velocities of the growing and condensing bubbles are moderate, $\pm 3 \text{ ms}^{-1}$, but the acceleration, $\pm 1100 \text{ ms}^{-2}$, is remarkable. Acceleration of this magnitude affects inevitably the strength requirements of suppression pool structures. Furthermore, it makes difficult to include delicate intrusive measurement instruments near the vent pipe outlet. Critical wavelength $\lambda_c = 1.0 \text{ mm} - 1.3 \text{ mm}$ limited the maximum node size in CFD simulation to 1 mm, which is still quickly runnable with a few computer cores as a transient 2D-axisymmetric simulation. The chugging frequencies were known to be around 1–4 Hz, calculating visually from the video. The most probable frequencies were estimated to be around 0.29 Hz–3.3 Hz, which fits well to expectations. The chugging oscillations are not periodic all the time, so the frequency spikes in FFT spread over a quite wide range. Furthermore, the experiment consists of various bubble types (Hujala et al., 2017) which condense differently. Frequency analysis also showed two higher frequencies around 53.4 Hz and 126.4 Hz. The first frequency is close to the natural frequency of this size of bubbles (Brennen, 2014). The latter frequency seems to be related to the interfacial area oscillations of the bubbles (Hujala et al., 2017). The frequency of the electricity grid is ($50.0 \pm 0.1 \text{ Hz}$), which has some effect on FFT evaluated using pressure transducer data. 53.4 Hz is so far from the grid frequency of 50 Hz that the 53.4 Hz frequency must be due to physical phenomena in the system, and not due to electricity grid excitation. The frequency analysis presented elsewhere showed that the 53.4 Hz is from the surface area of the bubbles (Hujala et al., 2017). Halogen lamps, which produce steady light intensity independent of grid frequency, were used in the DCC-05 experiment. Considering these points, the algorithm looks promising for investigation of surface events of bubbles, but more frequency analysis with other measured data is needed to establish the sources for each frequency observed.

6. Conclusions

The pattern recognition and data analysis algorithm presented in this work is able to acquire novel non-intrusive measurement data

about chugging direct contact condensation. The algorithm is well suited for symmetrical bubbles but not for precise evaluation of the volume and surface area, especially of small and very asymmetric steam bubbles. In addition to suppression pool problems, the algorithm can be applied to video material from other measurement environments too. Higher grade data from smaller scale facilities could be used to further validate the algorithm. More cylindrically symmetric bubbles are preferable for the algorithm. Such bubbles can be reached with more stable flow modes such as bubbly and slug flows within ducts or in some sparger blowdown phases. The performance of the algorithm can be benchmarked against wire mesh sensor (WMS) and particle image velocimetry (PIV) measurements.

The algorithm works well for estimation of growing and breaking up velocities and acceleration of the bubbles and gives significant information about events in the direct contact condensation process. The algorithm also gives valuable information about critical wavelength and maximum node size in CFD simulations. FFT and other frequency analysis methods are suitable means for comparison of pressure oscillation data and structure wall strain rate sensor data to the pattern recognition data of oscillating bubbles. Since the conditions of the PPOOLEX facility are challenging and some approximation always needs to be done, a framerate of at least 1000 fps should be used when possible. Furthermore the possibility of image zooming should be considered for a closer view of the bubbles and consequently better quality pattern recognition. Moreover, image zooming or increasing the resolution would decrease the amount of relative error of the algorithm.

Acknowledgements

The research leading to these results was partly funded by the Finnish Nuclear Waste Management Fund (VVR) via the Finnish Research Programs on Nuclear Power Plant Safety, SAFIR2014 and SAFIR2018. The authors gratefully acknowledge all this support. The authors wish to thank Mr. Peter Jones, who assisted in language revision of the manuscript.

Appendix A. Supplementary data

Supplementary data associated with this article can be found, in the online version, at <http://dx.doi.org/10.1016/j.nucengdes.2018.03.032>.

References

- Aust, E., Schultheiss, G., Seeliger, D., McCauley, E., 1983. Experimental results about dynamic load mitigation for BWR-pressure suppression containments under LOCA-conditions. *J. Loading Conditions Struct. Anal. Reactor Containment IASMIT* 43–50 <http://www.lib.ncsu.edu/resolver/1840.20/26068>.
- Aya, I., Kobayashi, M., 1983. Pressure and fluid oscillations in vent system due to steam condensation, (II) high-frequency component of pressure oscillations in vent tubes under at chugging and condensation oscillation. *J. Nucl. Sci. Technol.* 20, 213–227.
- Aya, I., Nariai, H., 1987. Boundaries between regimes of pressure oscillation induced by steam condensation in pressure suppression containment. *Nucl. Eng. Des.* 99, 31–40.
- Aya, I., Nariai, H., Kobayashi, M., 1980. Pressure and fluid oscillations in vent system due to steam condensation, (I) experimental results and analysis model for chugging. *J. Nucl. Sci. Technol.* 17, 499–515.
- Bestion, D., 2014. The difficult challenge of a two-phase CFD modelling for all flow regimes. *Nucl. Eng. Des.* 279, 116–125.
- Brennen, C., 2014. first ed. *Cavitation and Bubble Dynamics* Cambridge University Press 978-1-107-64476-2.
- Brouillette, M., 2002. The Richtmyer-Meshkov instability. *Annu. Rev. Fluid Mech.* 34, 445–468.
- Chan, C.K., Lee, C.K.B., 1982. A regime map for direct contact condensation. *Int. J. Multiph. Flow* 8, 11–20.
- Drazin, P.G., 2002. *Introduction to Hydrodynamic Stability*. Cambridge Texts in Applied Mathematics. Cambridge University Press.
- Gregu, G., Takahashi, M., Pellegrini, M., Meru, R., 2017. Experimental study on steam chugging phenomenon in a vertical sparger. *Int. J. Multiph. Flow* 88, 87–98.
- Hujala, E., 2013. Evaluation of Bubble Formation and Break Up in Suppression Pools by Using Pattern Recognition Methods (Master thesis). Lappeenranta University of Technology. LUT Energy, Lappeenranta, Finland. Available online: <http://urn.fi/URN:NBN:fi:fo201304082709>.
- Hujala, E., Tanskanen, V., Hyvärinen, J., 2017. Frequency analysis of chugging condensation in pressure suppression pool system with pattern recognition. In: The 17th International Topical Meeting on Nuclear Thermal Hydraulics (NURETH-17), Xi'an, Shaanxi, China, September 3–8.
- Hujala, E., Tanskanen, V., Puustinen, M., 2013. Progress in the development of pattern recognition algorithm for the PPOOLEX video data. Technical Report. Lappeenranta University of Technology, School of Technology, Laboratory of Nuclear Engineering.
- Ishii, M., Hibiki, T., 2011. 2nd edn. *Thermo-Fluid Dynamics of Two-Phase Flow* Springer Science + Business Media 978-1-4419-7984-1 e-ISBN 978-1-4419-7985-8.
- Issa, S.A., Weisenbe, P., Macian-Juan, R., 2014. Experimental investigation of steam bubble condensation in vertical large diameter geometry under atmospheric pressure and different flow conditions. *Int. J. Heat Mass Transf.* 70, 918–929.
- Kukita, Y., Namatame, K., Shiba, M., 1984. The LOCA air-injection loads in BWR Mark II pressure suppression containment systems. *Nucl. Eng. Des.* 77, 117–129.
- Kukita, Y., Namatame, K., Takeshita, I., Shiba, M., 1987. LOCA steam condensation loads in BWR Mark II pressure suppression containment system. *Nucl. Eng. Des.* 102, 225–228.
- Lahey, R., Moody, F., 1993. *The Thermal-Hydraulics of a Boiling Water Reactor*, 2 ed. American Nuclear Society, La Grange Park, Illinois, USA 0-89448-037-5.
- MATLAB, 2017. version 9.2.0 (R2017a). The MathWorks Inc., Natick, Massachusetts, USA.
- Meshkov, E.E., 1969. Instability of the interface of two gases accelerated by a shock wave. *Sov. Fluid Dyn.* 4, 101–104.
- Mimouni, S., Mechtoua, N., Foissac, A., Hassanaly, M., Ouraou, M., 2011. CFD modeling of wall steam condensation: Two-phase flow approach versus homogeneous flow approach. *Science and Technology of Nuclear Installations* 2011.
- Motoaki Utamura, K.M., Uozumi, H., 1984. Numerical analysis on pressure propagation in pressure suppression system due to steam bubble collapse. *J. Nucl. Sci. Technol.* 21, 279–287.
- Patel, G., Tanskanen, V., Hujala, E., Hyvärinen, J., 2017. Direct contact condensation modeling in pressure suppression pool system. *Nucl. Eng. Des.* 321, 328–342.
- Pellegrini, M., Araneo, L., Ninokata, H., Ricotti, M., Naitoh, M., Achilli, A., 2016. Suppression pool testing at the SIET laboratory: experimental investigation of critical phenomena expected in the Fukushima Daiichi suppression chamber. *J. Nucl. Sci. Technol.* 53, 614–629.
- Pellegrini, M., Naitoh, M., Josey, C., Baglietto, E., 2015. Modeling of Rayleigh-Taylor instability for steam direct contact condensation. In: The 16th International Topical Meeting on Nuclear Reactor Thermal Hydraulics (NURETH-16), Chicago, IL, August 30–September 4, pp. 15.
- Puustinen, M., Kyrki-Rajamäki, R., Tanskanen, V., Räsänen, A., Purhonen, H., Riikonen, V., Laine, J., Hujala, E., 2013. BWR Suppression Pool Studies with POOLEX and PPOOLEX Test Facilities at LUT. In: The 15th International Topical Meeting on Nuclear Thermal Hydraulics (NURETH-15), Pisa, Italy, 12–17 May, pp. 061.
- Puustinen, M., Laine, J., Räsänen, A., Hujala, E., 2014. Chugging Test with DN100 Blowdown Pipe in the PPOOLEX Facility. Technical Report. Lappeenranta University of Technology, Nuclear Safety Research Unit.
- Richtmyer, R.D., 1960. Taylor instability in shock acceleration of compressible fluids. *Commun. Pure Appl. Math.* XIII 297–319.
- Simpson, M.E., Chan, C.K., 1982. Hydrodynamics of a subsonic vapor jet in subcooled liquid. *J. Heat Transfer* 104, 271–278.
- Strutt, J.W. (Lord Rayleigh), 1883. Investigation of the character of the equilibrium of an incompressible heavy fluid of variable density. *Proc. London Math. Soc.* 14, 170–177.
- Tanskanen, V., Hujala, E., Puustinen, M., 2014a. Numerical simulation and analysis of PPOOLEX DCC-05 chugging test. Technical Report. Lappeenranta University of Technology, School of Energy Systems, Nuclear Engineering.
- Tanskanen, V., Jordan, A., Puustinen, M., Kyrki-Rajamäki, R., 2014b. CFD simulation and pattern recognition analysis of the chugging condensation regime. *Ann. Nucl. Energy* 66, 133–143.
- Taylor, G., 1950. The instability of liquid surfaces when accelerated in a direction perpendicular to their planes. Part I. *Proc. R. Soc. London, Ser. A* 201, 192–196.
- Windreich, G., Kiryati, N., Lohmann, G., 2003. Voxel-based surface area estimation: from theory to practice. *Pattern Recogn.* 36, 2531–2541.

Publication II

E. Hujala, V. Tanskanen and J. Hyvärinen
**Frequency analysis of chugging condensation in pressure suppression pool
system with pattern recognition**

Reprinted with permission from
Nuclear Engineering and Design,
Vol. 339, pp. 244-252, 2018
© 2018, Elsevier B.V.



Contents lists available at ScienceDirect

Nuclear Engineering and Design

journal homepage: www.elsevier.com/locate/nucengdes

Frequency analysis of chugging condensation in pressure suppression pool system with pattern recognition

Elina Hujala^{*}, Vesa Tanskanen, Juhani Hyvärinen

LUT School of Energy Systems, Nuclear Engineering, Lappeenranta University of Technology (LUT), P.O. Box 20, FIN-53851 Lappeenranta, Finland

ARTICLE INFO

Keywords:

Two-phase flow
Suppression pool
Chugging
Pattern recognition
FFT

ABSTRACT

Direct contact condensation (DCC) phenomena in boiling water reactor (BWR) pressure suppression pool systems need to be understood to properly assess the performance of the pool as a heat sink and as a safety critical structure. Condensation oscillations in the form of chugging are challenging to predict by computational fluid dynamics (CFD) methods but safety relevant because of associated high dynamic loads on in-pool structures and the pool itself. Recently, new measurement methods for CFD validation purposes have become available. One of these techniques is visual observation using the high-speed cameras and suitable data processing method. Pattern recognition is a well suited technique for the determination of large oscillating bubble dynamics in a pressure suppression pool.

In this work, the formation and collapse of the steam bubbles in chugging condensation mode are evaluated by using the pattern recognition algorithm. The pattern recognition algorithm is based on video material recorded during the direct contact condensation experiment DCC-05 of the PPOOLEX test facility. The formation speed, the shape and size of the steam bubbles and the acceleration of collapsing bubbles are estimated with the algorithm. Fast Fourier transform (FFT) is used for frequency analysis of the pattern recognized data. The frequencies found are compared to the frequency data of the pressure transducers collected during the experiment and to the previous results of the NEPTUNE_CFD simulations of the same experiment.

The frequency analysis shows that the chugging frequencies of the steam bubbles range from 1 to 3 Hz, as predicted. Also the natural frequencies of the bubbles are visible around 53 Hz. Another frequency spike was observed close to the 125 Hz. This frequency is close to the mechanical resonance frequencies of the suppression pool and the blowdown pipe. Because of neither the pressure suppression pool nor the blowdown pipe are visible to the pattern recognition, the spike of the higher frequencies is most likely from the interfacial area of the bubble which resonates with the suppression pool system, affecting rapid condensation at a certain point.

1. Introduction

The small size of the BWR containment bring on the possibility that a large amount of steam should be rapidly condensed into the suppression pool during the loss of coolant accident (LOCA). Injected steam causes structural loads to the suppression pool and demands a lot of its strength. One main cause of these structural loads are the pressure oscillations and chugging of condensed steam, which have been studied through the decades. Test facilities small (Aya et al., 1980; Aya and Kobayashi, 1983; Aya and Nariai, 1987; Simpson and Chan, 1982; Gregu et al., 2017) and large size (Utamura, Moriya, and Uozumi, 1984; Kukita et al., 1984; Kukita et al., 1987; Pellegrini et al., 2016) have been used to study these condensation modes. DCC is present in all of the modes, which emphasizes the need to validate and develop

condensation models being able to capture interfacial condensation rate correctly with the CFD software. Already, even in the old experiments, movie cameras were used for visual observation, but the observation results were hardly published. At first, the data analysis concentrated for pressure data analysis, but the arrival of the CFD made possible to model the physical behavior of the condensation more accurately than with simplified analytical models (Lahey and Moody, 1993; Lahey, 2005). Different condensation modes have been modeled by using CFD (Patel et al., 2017; Mimouni et al., 2011). As the modeling of two-phase flows using CFD has challenges (Bestion, 2014), a new measurement methods for CFD model validation purposes has been put into operation. Lately, the high-speed cameras have been started to use to record the experiments in more thorough manner (Issa et al., 2014; Tanskanen, 2012) to make data analysis more feasible. The measured data is used

^{*} Corresponding author.

E-mail address: Elina.Hujala@lut.fi (E. Hujala).

<https://doi.org/10.1016/j.nucengdes.2018.09.018>

Received 29 June 2018; Accepted 18 September 2018
0029-5493/ © 2018 Elsevier B.V. All rights reserved.

Nomenclature		$ Y(f) $	dimensionless absolute value of amplitude
<i>Variables</i>		γ	ratio of the specific heat of the water
		ρ_w	density of the water
<i>Abbreviations</i>			
A	surface area	BWR	boiling water reactor
d	diameter	CFD	computational fluid dynamics
f	frequency	DCC	direct contact condensation
f_0	natural frequency of oscillating bubble	FFT	Fast Fourier Transform
P_0	steady state pressure	LOCA	Loss of coolant accident
p_1, p_5	pressure transducers p_1 and p_5	LUT	Lappeenranta University of Technology
r	radius	PACTEL	parallel channel test loop
R_0	steady state radius of the bubble	(P)POOLEX	condensation pool experiments
t	time		
V	volume		

to evaluate different features diameter, velocity, position of the condensing bubbles (Issa et al., 2014). At Lappeenranta University of Technology (LUT) a preliminary pattern recognition algorithm was created for the use of former condensation pool test facility POOLEX (Tanskanen et al., 2014b). Later on, the pattern recognition and data analysis algorithm has been upgraded to evaluation of diameter, surface area, volume, velocity, acceleration and frequencies of the condensing steam bubbles (Hujala, 2013; Hujala et al., 2013; Hujala et al., 2018).

This paper presents the frequency analysis of the recorded video data of direct contact condensation experiment DCC-05-4 of the PPOOLEX test facility using FFT on the volume data evaluated by using the upgraded pattern recognition and data analysis algorithm. The results are briefly compared to the NEPTUNE_CFD code simulations and the pressure transducer data. The source of some frequency spikes have also been tracked by applying hammer tests to the PPOOLEX facility.

2. Experiments and methods of analysis

2.1. PPOOLEX test facility and DCC-05 experiment

The PPOOLEX test facility is a scaled down test facility of Nordic type BWR containment. The schematic view of the PPOOLEX test facility is shown in Fig. 1.

The 31 m³ stainless steel pressurized vessel has the total height of 7.45 m and diameter of 2.4 m. It consists of two main parts, the dry well compartment and the wet well compartment separated by an intermediate floor, an inlet plenum and air/steam piping. A route for air/steam flow from the dry well to the wet well is created by a vertical blowdown pipe attached non-axisymmetrically underneath the floor. The different lengths and widths of the blowdown pipe can be used depending on the needs of the ongoing experiment. Steam needed in the experiments is produced by near PACTEL test facility, which has the core power of 1 MW. The more detailed description of the PPOOLEX test facility is presented in (Puustinen et al., 2013).

DCC-05 experiment was one part of the direct contact condensation

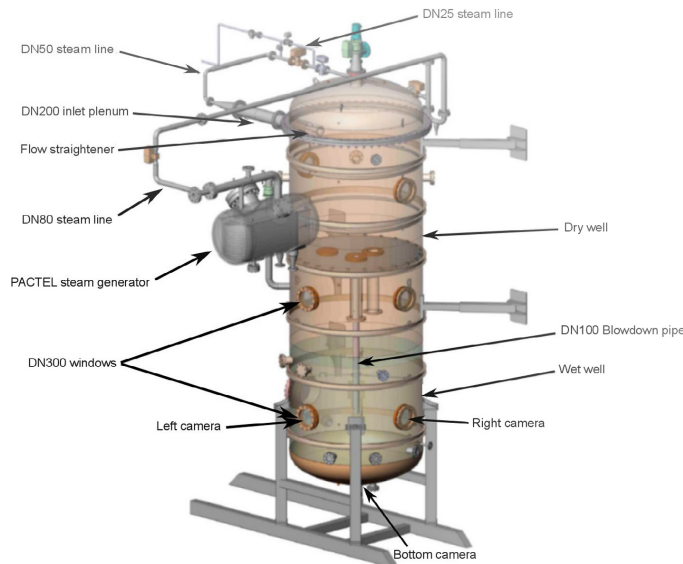


Fig. 1. Schematic view of the PPOOLEX test facility.

test program. The main purpose of the DCC-05 was to obtain measurement data for the validation of the DCC models used in CFD, and to make a high-speed video recording to be used in the development work of the pattern recognition algorithm (Hujala, 2013; Hujala et al., 2018). The aim of the DCC-05 experiment was to keep the pool water temperature as constant as possible and change the steam flow rate in a wide range. The goal was achieved by adjusting the steam flow rate quickly to a new value for the recorded periods, but when the data was being transferred from the camera memory, the steam flow rate was reduced to almost zero to prevent unnecessary heat-up of the pool water. Regardless, the pool water at the blowdown pipe outlet rose about 10 K. DN100 blowdown pipe was used in the experiment. The more detailed description of the DCC-05 experiment is presented in (Tanskanen et al., 2014a).

DCC-05 experiment was recorded by using three high-speed cameras at framerate of 300 frames per second. Places of two side cameras and the bottom camera are shown in Fig. 1. DCC-05 consists of six parts named DCC-05-1–DCC-05-6. DCC-05-4 part was chosen for closer investigation due to the best quality of the video material. 48 s of video material was recorded during that part. The video was cut in frames of the resolution of 768×768 pixels. MATLAB software was used to create the pattern recognition and data analysis algorithm, which recognizes the shapes of the steam bubbles pushed through the blowdown pipe and evaluates the volume and the surface area of each bubble using voxel-based method (Windreich et al., 2003) and smoothing. Algorithm also evaluates the diameter, growth and break up velocities and accelerations of the bubble. The simplified principle of the algorithm is presented in Fig. 2 and explained more accurately in (Hujala et al., 2018).

2.2. Frequency analysis

Frequency analysis of the condensing steam bubbles is an interesting area, because that makes possible to connect bubble fluctuations to the other oscillating measured quantities. FFT have been used to evaluate different frequencies in the experiment. It works best when the amount of data is large and the recording period is long. FFT can be used for short periods too, but it should be recalled, that in those cases the dominating lowest frequencies are not reliable. FFT is also used to evaluate frequency modes of the PPOOLEX facility. Frequency modes of the facility were evaluated from the pressure transducer data of the hammer tests. In the hammer tests the PPOOLEX tank was hit by the hammer and pressure transducer and strain gauge data were recorded. The hammer test was carried out for the both, drained and filled conditions of the pool. In the filled conditions, the water level was the same as in the DCC-05 experiment. The results of the blowdown experiment were also compared to the frequencies obtained from CFD simulations.

Natural oscillation frequency of the condensing bubbles is one potential research area which may exploit the FFT. The natural frequency of the oscillating bubble f_0 can be expressed analytically (Brennen, 2014), as shown in Eq. (1).

$$f_0 = \frac{1}{2\pi} \sqrt{\frac{3\gamma P_0}{\rho_w R_0^3}}, \tag{1}$$

where γ [–] is the ratio of the specific heat of the water, P_0 [Pa] is the steady state pressure, ρ_w $\left[\frac{\text{kg}}{\text{m}^3}\right]$ is the density of the water and R_0 [m] is the steady state radius of the steam bubble.

3. Results and discussion

The pattern recognition and data analysis algorithm was used to evaluate the diameter d [cm], surface area A [cm²] and volume V [cm³] of the bubbles. The change of d , A and V during the DCC-05-4 test are presented in Fig. 3.

The diameter d of the bubble is rarely a zero numerically due to the evaluation method which calculates the number of nonzero elements in the figure. The diameter has been evaluated by looking for the row with the largest amount of nonzero elements, even if only a one row the border of the bubble of the bubble is visible. The surface area varies between zero to a bit over 2000 cm² and the volumes between zero and 4500 cm³. However, the calculation method based on the side profile of the bubbles underestimates the surface area and volume. Error estimation showed that the errors of the volume and surface area remain under 10 %, when the diameter of the bubble is under 13 cm. For really small bubbles ($d < 4.0$ cm) errors may build up over 20 %, but otherwise lay between 10 and 20 %, (Hujala et al., 2018). However, the uncertainty caused by these systematic errors should remain small in this study, because the bubble size difference between successive frames is more important than the absolute size of a bubble.

Natural frequencies f_0 [Hz] were calculated by using the evaluated diameters of the bubbles using the Eq. (1). Frequencies fluctuate between the 53 Hz and the 250 Hz, and the most common natural frequency is around 80 Hz. The distribution of the natural frequencies of the bubbles is presented as a histogram in Fig. 4. The natural frequency cannot be less than 44 Hz, as the natural frequency is lower for larger bubbles and the largest recognized diameter of the bubble in DCC-05-4 test was approximately 24 cm.

The FFT calculated from the volume data is presented in Fig. 5. As a part of non-intrusive measurement, the data of it is not contaminated by the oscillations of the pools structures or the blowdown pipe i.e. the obtained frequencies in FFT should be the characteristics of the bubbles. However, it is still possible, that the structures of the pool resonate at the same frequencies as the bubbles and strengthens the influence of the oscillations. In FFT, the lower frequencies under the 10 Hz are dominant and the most probable chugging frequencies were between the 0.29 Hz and 3.3 Hz as marked in Fig. 5. Two larger swells higher frequencies are visible, one near to the 53 Hz and another near to the 125 Hz.

Theoretical natural frequencies of DCC-05-4 experiment at different radii of the bubbles were calculated by using Eq. (1). The highest spike near to the 53 Hz is 53.4 Hz in FFT (Fig. 5), which corresponds to the bubble radius of 10.9 cm. On the other hand, the biggest diameter of the

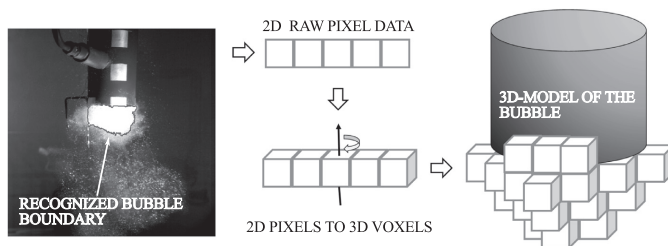


Fig. 2. Simplified principle of the pattern recognition algorithm.

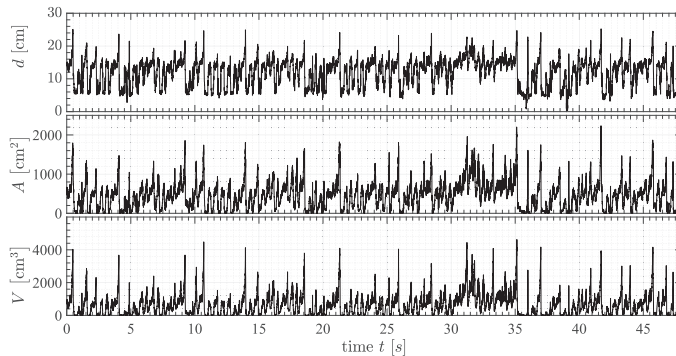


Fig. 3. Estimated diameter d [cm], surface area A [cm²] and volume V [cm³] of the bubbles during the DCC-05-4 experiment.

bubble measured from the video data is 24.2 cm, which corresponds to the frequency of 48.1 Hz.

Calculated possible natural frequencies of the bubbles, the most common frequency in FFT of the volume data, and the biggest bubble in the DCC-05-4 video are presented in Fig. 6. The biggest bubble of the video and the most common bubble size in FFT are so close to each other, that it can be said that the sizes of the bubbles are almost even, recalling the inaccuracies of the pattern recognition and interpretation of the FFT. Visual observation of the video material supports this result.

The change of the frequencies during the time t [s] can be seen by using a spectrogram. The spectrogram of the whole DCC-05-4 test is presented in Fig. 7. Lower frequencies are dominant through the experiment, but higher values can be seen near the 53 Hz and the 125 Hz through the experiment.

The 53 Hz and the 125 Hz frequencies are interesting, because large 53 Hz bubbles are rare in the experiment and small 125 Hz bubbles are just smaller than the pipe diameter and cannot be considered spherical bubbles anymore. Those should not be the most probable natural frequencies of the bubbles, so those are assumed to be linked up to the condensation process. From volume data of Fig. 3, three alternating bubble volume cycles can be seen, types A, B and C. Type A bubble cycle is the simplest one. The bubble grows up in two parts, as a fluctuating part where the bubble builds up oscillating and the rapid growth part, where the fluctuating bubble grows up fast and condensates then completely very rapidly. The volumetric change of type A bubble is presented in Fig. 8A.

Type B bubble cycle consists of multiple oscillating parts of which

the final one grows up faster and breaks up rapidly. The volume in the preceding fluctuating parts does not fall to zero at any time. Type B bubble volume change is presented in Fig. 9A.

Type C bubble consists one or multiple fluctuating parts. The bubble oscillates, grows up, and breaks up with comparable rates without having a rapidly collapsing volume period. Type C bubble is presented in Fig. 10A. The images of the different phases of type A, B and C bubbles are presented in Figs. 8, 9, and 10.

Animations of the A, B and C type bubbles are available in the [Supplementary Material](#) of the online version of this article.

The FFT was calculated for all three types of bubbles. The FFT of full parts of different types A, B and C are marked as black line and are presented in Fig. 8B, Fig. 9B and Fig. 10B. High, but unreliable low frequency part under the 10 Hz has been cut off to get better view to more reliable frequencies. All of the cases have clearly visible elevation around the 50 Hz. At type A, the 53 Hz spike is not as distinguishable as in type B or C, due to the extremely short time period, but the 53 Hz spike still exists. By contrast, the 125 Hz spike appears in type A and B bubbles, but not in type C bubble.

The volumetric change of each bubble type A, B and C have been divided two or more parts, to investigate how different frequencies split at different parts. Type A bubble were split in two parts. Red line in Fig. 8A, represents the fluctuating part of the bubble, when the bubble volume grew up from zero to over 1000 cm³ oscillating slightly. The corresponding FFT of the red part is shown in Fig. 8C. The FFT shows clear spikes around 53 Hz and 125 Hz. Blue line in Fig. 8A represents the fast growth and rapid condensation part and the Fig. 8D shows the

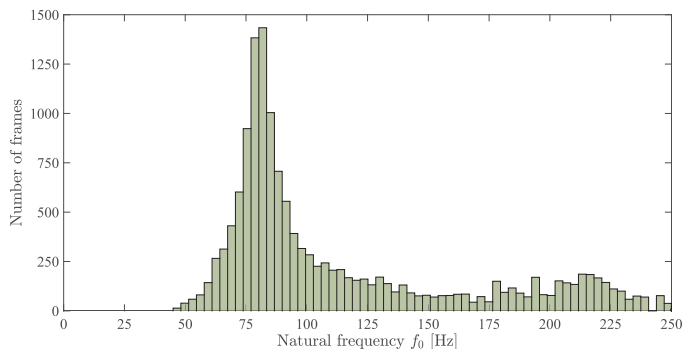


Fig. 4. Distribution of the natural frequencies f_0 [Hz] of the bubbles evaluated using the recognized bubble diameters.

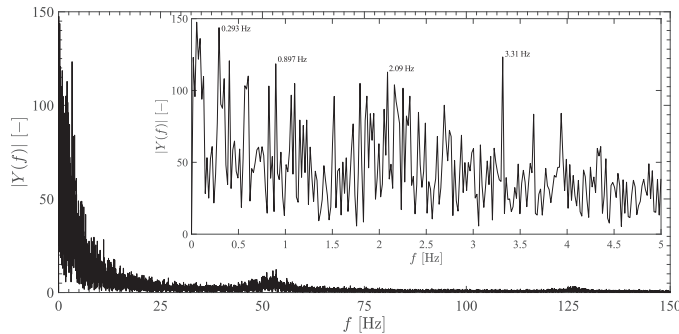


Fig. 5. FFT of the volume data of DCC-05-4 test. $|Y(f)|$ is dimensionless absolute value of an amplitude and f [Hz] is the frequency. The most probable chugging frequencies 0.293 Hz, 0.897 Hz, 2.09 Hz and 3.31 Hz are marked at their places (Hujala et al., 2018).

corresponding FFT. The latter part of the bubble consists of the 53 Hz and the 125 Hz spikes too, but also other spikes around those are clear.

Type B bubble in Fig. 9 was cut in six parts (green to blue). The first five parts are fluctuating parts and the last part is similar fast growth part with rapid condensation as in the type A bubble. The corresponding FFTs are presented in Fig. 9C–H. The first green part in Fig. 9C contains visible spike around 53 Hz, but no 125 Hz spike. The second part starts near to zero and grows up oscillating, causing a significant 53 Hz spike and a smaller, but visible 125 Hz spike. The third part starts from bigger volume than the second one, but oscillates similarly having 53 Hz spike. The 125 Hz spike is also present, but it does not come out from group of other high frequencies. The fourth part shows some change in the later phase of the cycle. Oscillating bubble grows up, but then loses its volume more rapidly than in previous parts. The corresponding FFT in Fig. 9F presents significant 53 Hz spike with multiple lower level high frequency spikes and also poorly distinguishable 125 Hz with the same amplitude. The fifth (magenta) part of the bubble reminds type A bubble cycle. Bubble oscillates, grows up and oscillates more, then it rapidly increases its volume still fluctuating and finally decreases fast oscillating. The FFT of it shows multiple significant spikes around 53 Hz and once more clearly emerged 125 Hz frequency spike. The sixth and last (blue) part represents fast growth and rapid condensation of the bubble. The FFT shows slightly flatten out frequency spikes where the 53 Hz spike is still significant and the 125 Hz visible, but more leveled out amongst other high frequencies.

Type C bubble in Fig. 10 consists of two very identical oscillating parts, marked as red and blue. Both parts grow up oscillating and decreases their volumes oscillating. Between these two parts, the bubble disappears almost totally inside the blowdown pipe. Both parts FFTs are quite identical too. Both show dominating 53 Hz spikes with no other considerable frequencies.

These three different bubble types A, B and C have similar structures. Oscillating bubbles which grow up and diminish oscillating, as the green part in type B in Fig. 9 and type C bubbles in Fig. 10. These bubbles do not grow up larger than the diameter of the blowdown pipe is, neither change their sizes rapidly nor have the fast growth or rapid condensation parts. In type B bubble, the 53 Hz spike remains through the whole condensation process similarly as in type A bubble. The 125 Hz bubble arises when the oscillating bubble grows up. Similarly type A bubble consists of the 125 Hz frequency spike. The last part of type A and B bubbles are similar. The fast growth and rapid condensation part has both the 53 Hz spike and the 125 Hz spike, but both are almost flatten out.

Pressure transducers were used to measure pressure changes in the pool. Transducer p_1 was inside the blowdown pipe near the outlet and the transducer p_2 in the water, 5 cm under the blowdown pipe outlet, relatively near to the surface of the blown bubbles. The FFT clip up to the 153 Hz calculated from the pressure transducer data is shown in Fig. 11.

Fig. 11 shows that both transducers have pressure changes at

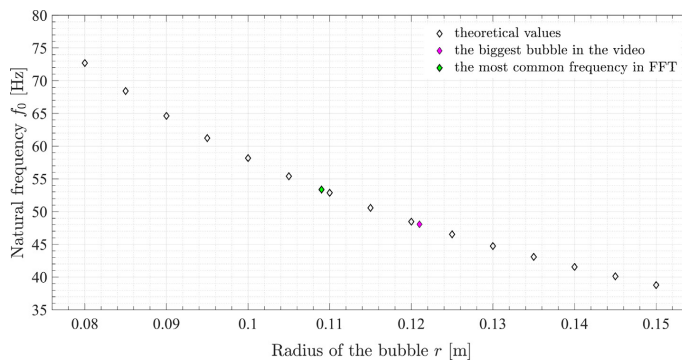


Fig. 6. Calculated natural frequencies f_0 [Hz] of the bubbles at different radii r [m] are marked in white filled markers. The most common higher frequency in FFT is marked green filled marker and the biggest bubble diameter evaluated from the video material is marked in magenta filled marker.

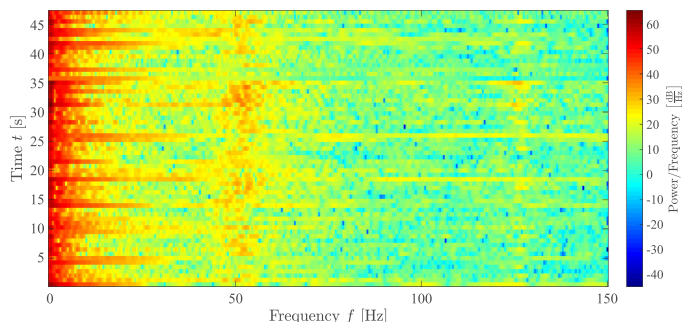


Fig. 7. Spectrogram of the DCC-05-4 experiment.

frequency of the 53 Hz and the 125 Hz. This confirms the FFT result of the pattern recognition data, and indicates that the 53 Hz and the 125 Hz spikes are most likely coming from the surface of the oscillating bubbles.

In the hammer tests, the suppression pool was hit by a hammer and frequencies were estimated from the pressure transducer p_6 data. The pressure transducer was placed at the bottom of the pool, where it stands also during the blowdown experiments. The FFT of the hammer tests are shown in Fig. 12.

In the empty pool, FFT shows a couple of sharp spikes: a high spike of 71.5 Hz and a lower one of 150.2 Hz. When the pool was filled with water up to the level 1.03 m above the pipe outlet, a lot more vibrations appeared. The largest downward widen spikes are around 125 Hz, 136 Hz and 151 Hz. Because in the blowdown experiments 125 Hz spike appears only with abruptly condensing type A and B bubbles but not with type C bubbles or as noise in video frames without bubble, it is highly possible that the vibrations of the pool resonate with the surface

vibrations of the bubbles and strengthens the condensation.

The FFT of the volume data was also compared to the simulation data of NEPTUNE_CFD (Patel et al., 2017). The FFT example of the simulation data (Patel et al., 2016) is presented in Fig. 13.

The 53 Hz spike is significant in successful CFD simulations too, and the most probable chugging frequencies varies at the same level as in the FFT of the volume data in Fig. 5. However, the 125 Hz spike and actually all frequencies over the 53 Hz are missing in the FFT. If the 125 Hz frequency is strengthened via resonance as it seems to be according to the hammer tests, it cannot be seen in the CFD simulation where the structures of the test facility are rigid. If the 125 Hz spike is the effect of the surface area of the bubble, increase of the grid resolution in the simulations might bring out the higher frequencies, so more research will still be needed.

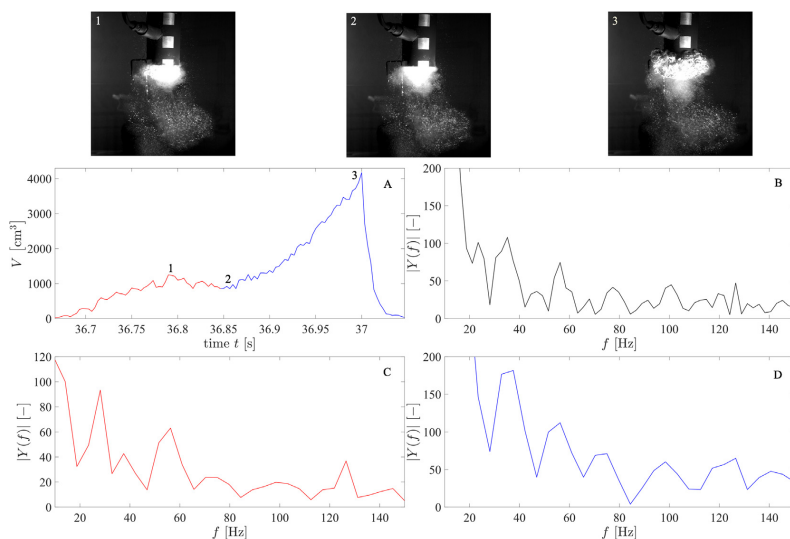


Fig. 8. A. The change of the volume V of type A bubble. B. FFT of the whole type A bubble volume data. $|Y(f)|$ is dimensionless absolute value of an amplitude and f [Hz] is the frequency. C. FFT of the first red part of the type A bubble volume data. D. FFT of the latter blue part of the type A bubble volume data. Images 1–3 represent different phases of the type A bubble.

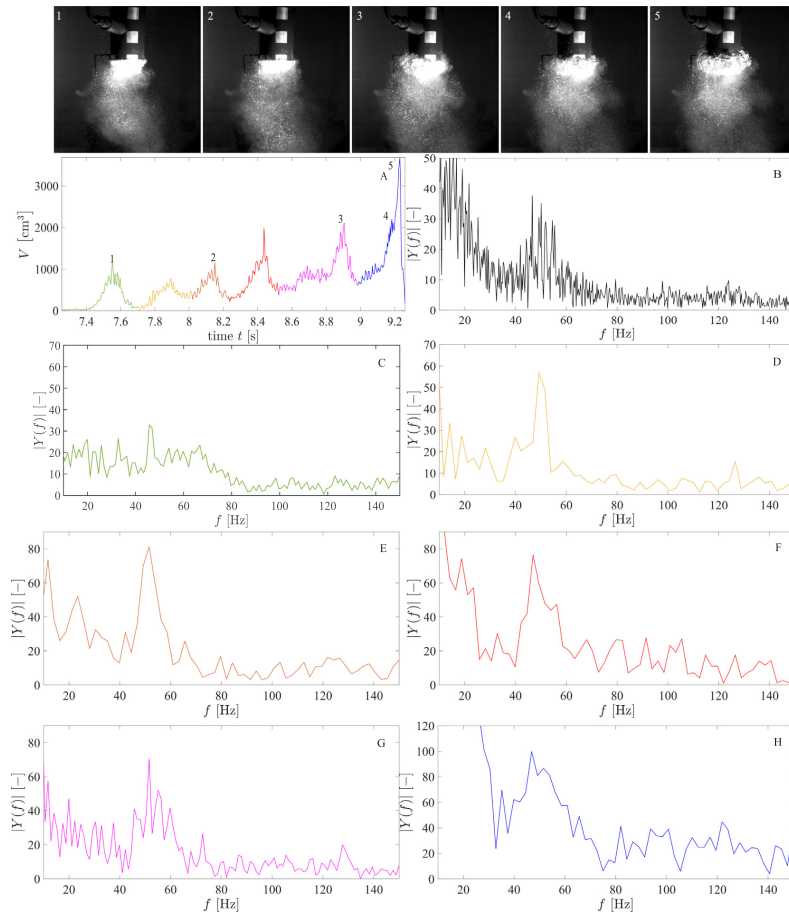


Fig. 9. A. The change of the volume V of type B bubble. B. FFT of the whole type B bubble volume data. $|Y(f)|$ is dimensionless absolute value of an amplitude and f [Hz] is the frequency. C. FFT of the 1st green part of the type B bubble volume data. D. FFT of the 2nd yellow part of the type B bubble volume data. E. FFT of the 3rd orange part of the type B bubble volume data. F. FFT of the 4th red part of the type B bubble volume data. G. FFT of the 5th magenta part of the type B bubble volume data. H. FFT of the latter blue part of the type B bubble volume data. Images 1–5 represent different phases of the type B bubble.

4. Conclusions

Frequency analysis of DCC-05-4 experiment of PPOOLEX test facility was made by using upgraded pattern recognition and data analysis algorithm. The chugging frequencies evaluated from the volume data applying FFT were around 1 Hz–3 Hz, which fitted well to the NEPTUNE_CFD simulation results and theoretical expectations (Aya et al., 1980; Aya and Kobayashi, 1983). Two different higher frequencies appeared in FFT, the 53 Hz and the 125 Hz. These frequencies turn up through the DCC-05-4 experiment.

The volume data was cut in parts and three different types of bubbles occurred, say, types A, B and C. Frequency analysis showed that the 53 Hz frequency appeared in all types of bubbles, but the 125 Hz spike only in types A and B. It looks like the 125 Hz frequency most likely leads to the fast growth and rapid condensation of the bubble and it does not exist when the bubble grows up and breaks down calmly

oscillating. The most probable explanation is that both frequencies are related to the surface area of the steam bubbles and the condensation process. Both spikes are visible in pressure transducer data, but the 125 Hz spike is missing in CFD simulations assuming rigid pool and piping structures. In 2D CFD simulations, the blowdown pipe was axisymmetrically at the center of the pool and non-condensable gases were not modeled. These might for one's part affect to the results. Hammer tests showed that the mechanical vibrations (flexing) of the containment structures may resonate with the bubble interface vibrations affecting rapid contact condensation. It is possible that fluid-structure interactions might lead to more effective or more stable condensation modes also in an actual BWR suppression pool. Because of this, the frequency analysis is an interesting subject, and more research need to be done.

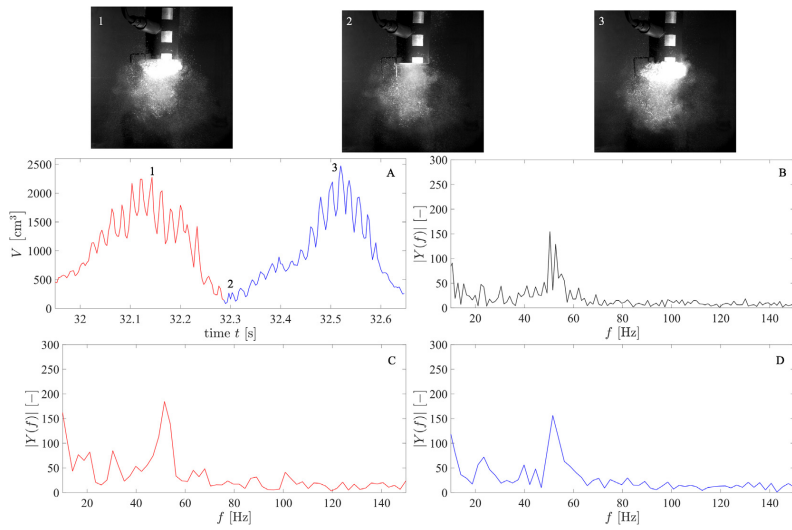


Fig. 10. A. The change of the volume V of type C bubble. B. FFT of the whole type C bubble volume data. $|Y(f)|$ is dimensionless absolute value of an amplitude and f [Hz] is the frequency. C. FFT of the first red part of the type C bubble volume data. D. FFT of the latter blue part of the type C bubble volume data. Images 1–3 represent different phases of the type C bubble.

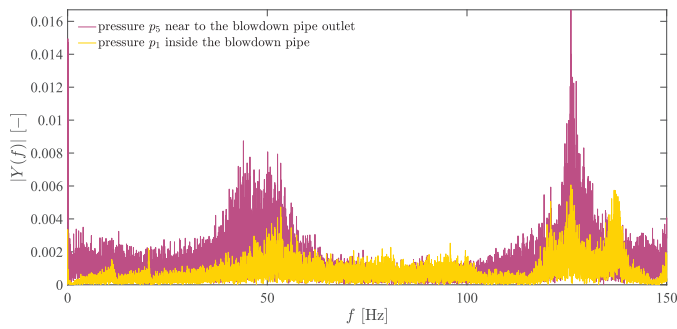


Fig. 11. FFT of the pressure transducers p_1 (yellow) and p_5 (magenta).

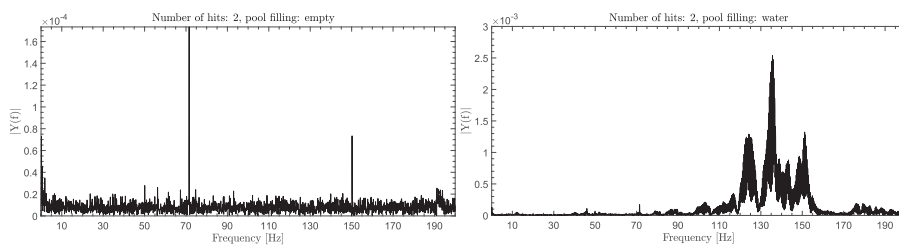


Fig. 12. FFTs of the hammer tests. The PPOOLEX tank was hit twice with the hammer and the data was recorded using pressure transducers. The amplitudes are comparable. Notice the tenfold difference between the empty tank (left) and the water filled tank (right).

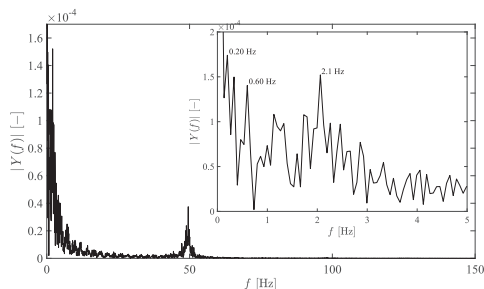


Fig. 13. FFT of the simulation of NEPTUNE_CFD. The data has significant 50 Hz frequency spike, without the 125 Hz spike. The most probable chugging frequencies 0.20 Hz, 0.60 Hz and 2.1 Hz are marked at their places.

Acknowledgements

The research leading to these results was partly funded by the Finnish Nuclear Waste Management Fund (VYR) via the Finnish Research Programs on Nuclear Power Plant Safety, SAFIR2014 and SAFIR2018. The authors gratefully acknowledge all this support.

Appendix A. Supplementary data

Supplementary data associated with this article can be found, in the online version, at <https://doi.org/10.1016/j.nucengdes.2018.09.018>.

References

- Aya, I., Kobayashi, M., 1983. Pressure and fluid oscillations in vent system due to steam condensation, (II) high-frequency component of pressure oscillations in vent tubes under at chugging and condensation oscillation. *J. Nucl. Sci. Technol.* 20, 213–227.
- Aya, I., Nariai, H., 1987. Boundaries between regimes of pressure oscillation induced by steam condensation in pressure suppression containment. *Nucl. Eng. Des.* 99, 31–40.
- Aya, I., Nariai, H., Kobayashi, M., 1980. Pressure and fluid oscillations in vent system due to steam condensation, (I) experimental results and analysis model for chugging. *J. Nucl. Sci. Technol.* 17, 499–515.
- Bestion, D., 2014. The difficult challenge of a two-phase CFD modelling for all flow regimes. *Nucl. Eng. Des.* 279, 116–125.
- Brennen, C., 2014. *Cavitation and Bubble Dynamics*, first ed. Cambridge University Press ISBN 978-1-107-64476-2.
- Gregu, G., Takahashi, M., Pellegrini, M., Mereu, R., 2017. Experimental study on steam chugging phenomenon in a vertical sparger. *Int. J. Multiph. Flow* 88, 87–98.
- Hujala, E., 2013. Evaluation of bubble formation and break up in suppression pools by using pattern recognition methods. Master thesis. Lappeenranta University of Technology. LUT Energy, Lappeenranta, Finland. Available online: <http://urn.fi/URN:NBN:fi-fe201304082709>.
- Hujala, E., Tanskanen, V., Hyvärinen, J., 2018. Pattern recognition algorithm for analysis of chugging direct contact condensation. *Nucl. Eng. Des.* 332, 202–212.
- Hujala, E., Tanskanen, V., Puustinen, M., 2013. Progress in the development of Pattern Recognition algorithm for the PPOOLEX video data. Technical Report. Lappeenranta University of Technology, School of Technology, Laboratory of Nuclear Engineering.
- Issa, S.A., Weisensee, P., Macian-Juan, R., 2014. Experimental investigation of steam bubble condensation in vertical large diameter geometry under atmospheric pressure and different flow conditions. *Int. J. Heat Mass Transf.* 70, 918–929.
- Kukita, Y., Namatame, K., Shiba, M., 1984. The LOCA air-injection loads in BWR Mark II pressure suppression containment systems. *Nucl. Eng. Des.* 77, 117–129.
- Kukita, Y., Namatame, K., Takeshita, I., Shiba, M., 1987. LOCA steam condensation loads in BWR Mark II pressure suppression containment system. *Nucl. Eng. Des.* 102, 225–228.
- Lahey, R., 2005. The simulation of multidimensional multiphase flows. *Nucl. Eng. Des.* 235, 1043–1060.
- Lahey, R., Moody, F., 1993. *The Thermal-Hydraulics of a Boiling Water Reactor*, 2 ed. American Nuclear Society, La Grange Park, Illinois, USA0-89448-037-5.
- Mimouni, S., Mechtoua, N., Foissac, A., Hassanaly, M., Ouraou, M., 2011. CFD modeling of wall steam condensation: Two-phase flow approach versus homogeneous flow approach. *Sci. Technol. Nucl. Install.* 2011.
- Utamura, M., Moriya, K., Uozumi, H., 1984. Numerical analysis on pressure propagation in pressure suppression system due to steam bubble collapse. *J. Nucl. Sci. Technol.* 21, 279–287.
- Patel, G., Tanskanen, V., Hujala, E., 2016. Direct Contact Condensation Calculations of PPOOLEX Experiment DCC-05. Technical Report. Lappeenranta University of Technology, School of Energy Systems, Nuclear Engineering, D.3.3.1.
- Patel, G., Tanskanen, V., Hujala, E., Hyvärinen, J., 2017. Direct contact condensation modeling in pressure suppression pool system. *Nucl. Eng. Des.* 321, 328–342.
- Pellegrini, M., Araneo, L., Ninokata, H., Ricotti, M., Naitoh, M., Achilli, A., 2016. Suppression pool testing at the SIET laboratory: experimental investigation of critical phenomena expected in the Fukushima daiichi suppression chamber. *Nucl. Sci. Technol.* 53, 614–629.
- Puustinen, M., Kyrki-Rajamäki, R., Tanskanen, V., Räsänen, A., Purhonen, H., Riikonen, V., Laine, J., Hujala, E., 2013. BWR Suppression Pool Studies with POOLEX and PPOOLEX Test Facilities at LUT. In: *The 15th International Topical Meeting on Nuclear Thermal Hydraulics (NURETH-15)*.
- Simpson, M.E., Chan, C.K., 1982. Hydrodynamics of a subsonic vapor jet in subcooled liquid. *J. Heat Transfer* 104, 271–278.
- Tanskanen, V., 2012. CFD modelling of direct contact condensation in suppression pools by applying condensation models of separated flow. *Acta Universitatis Lappeenrantaensis* 472. Lappeenranta University of Technology. ISBN 978-952-265-221-8, ISBN 978-952-265-222-5 (PDF), ISSN 1456-4491.
- Tanskanen, V., Hujala, E., Puustinen, M., 2014a. Numerical simulation and analysis of PPOOLEX DCC-05 chugging test. Technical Report. Lappeenranta University of Technology, School of Energy Systems, Nuclear Engineering.
- Tanskanen, V., Jordan, A., Puustinen, M., Kyrki-Rajamäki, R., 2014b. CFD simulation and pattern recognition analysis of the chugging condensation regime. *Ann. Nucl. Energy* 66, 133–143.
- Windreich, G., Kiryati, N., Lohmann, G., 2003. Voxel-based surface area estimation: from theory to practice. *Pattern Recogn.* 36, 2531–2541.

Publication III

G. Patel, V. Tanskanen, E. Hujala and J. Hyvärinen

Direct contact condensation modeling in pressure suppression pool system

Reprinted with permission from
Nuclear Engineering and Design,
Vol. 321, pp. 328-342, 2017
© 2017, Elsevier B.V.



ELSEVIER

Contents lists available at ScienceDirect

Nuclear Engineering and Design

journal homepage: www.elsevier.com/locate/nucengdes

Direct contact condensation modeling in pressure suppression pool system



G. Patel, V. Tanskanen*, E. Hujala, J. Hyvärinen

LUT School of Energy Systems/Nuclear Engineering, Lappeenranta University of Technology (LUT), PO Box 20, FIN-53851 Lappeenranta, Finland

HIGHLIGHTS

- Chugging condensation mode in drywell–wetwell suppression pool system was simulated.
- Bubble volumes and frequencies were obtained from video data by pattern recognition.
- Eulerian two-fluid approach of the compressible flow solvers was applied.
- Good results were obtained if Rayleigh–Taylor instability was taken into account.

ARTICLE INFO

Article history:

Received 31 May 2016

Received in revised form 12 August 2016

Accepted 19 August 2016

Available online 13 September 2016

ABSTRACT

The pressure suppression pool of boiling water reactor as a safety system has vital importance from the nuclear reactor safety point of view and it is an interesting challenge for numerical simulations of flow with rapid phase change. This paper presents the recent analysis of computational fluid dynamics (CFD) simulations of chugging direct contact condensation (DCC) mode observed in the drywell–wetwell suppression pool (PPOOLEX) experiments of Lappeenranta University of Technology. A pattern recognition algorithm was employed to determine the bubble volume and the chugging frequency during the test. The numerical simulations were performed by using Eulerian–Eulerian two-fluid approach of the compressible flow NEPTUNE_CFD software and the OpenFOAM CFD code. The interfacial heat transfer between steam and water was modeled by using three DCC models. Flow turbulence was solved by employing two $k-\epsilon$ turbulence models. The significance of interfacial area modeling on the chugging DCC was tested by implementing Rayleigh–Taylor interfacial area model. The performance of different DCC models, the effects of turbulence modeling and interfacial area modeling are presented. The sensitivity of chugging DCC to the initial conditions and to the modeled domain, and the effect of interfacial momentum transfer closure modeling on the chugging are briefly discussed. The choice of DCC model, accuracy of interfacial area modeling and the magnitude of liquid turbulence near the interface are all needed to replicate chugging in a drywell–wetwell suppression pool system. In coarse grid case, the DCC model of Coste 2004 with the Rayleigh–Taylor interface instability model of Pellegrini et al. (2015) provided best results.

© 2016 Elsevier B.V. All rights reserved.

1. Introduction

The boiling water reactor (BWR) cooling system can be more compact than the pressurized water reactor (PWR) one, due to the absence of secondary circuit. The proper functioning of pressure suppression pool (PSP) is very essential in BWRs containment because the pressure build-up and the released energy in the containment during a loss of coolant accident (LOCA) or safety relief valve actuation are mitigated in the PSP (Lahey and Moody, 1993).

In the fundamental engineering literature, the mostly studied vapor condensation issues include either dropwise condensation or filmwise condensation along a wall which separates the vapor and the coolant. However, the condensation heat transfer mode appearing particularly in a PSP system during transient and accidents conditions can be categorised as direct contact condensation (DCC) in which the continuous vapor and liquid phases share a large interface where the phase change takes place.

During a LOCA or safety relief valve actuation, a large amount of steam and non-condensable gases are blown via the upper drywell of the PSP system to the wetwell compartment through the blow-down pipes. Steam condenses in the water pool and the non-condensables rise up to the gas space of wetwell. The nature and

* Corresponding author

E-mail address: vesa.tanskanen@lut.fi (V. Tanskanen).

Nomenclature	
<i>Latin alphabet</i>	
d	diameter scale (m)
g	acceleration ($m\ s^{-2}$)
h	heat transfer coefficient ($W\ m^{-2}\ K^{-1}$)
H	total enthalpy ($J\ kg^{-1}$)
k	turbulent kinetic energy ($m^2\ s^{-2}$)
L	length scale (m)
Nu	Nusselt number (–)
P	pressure (Pa)
Pr	Prandtl number (–)
q''	heat flux ($W\ m^{-2}$)
Re	Reynolds number (–)
t	time (s)
u	velocity component ($m\ s^{-1}$)
U	velocity ($m\ s^{-1}$)
V	velocity scale ($m\ s^{-1}$)
<i>Greek alphabet</i>	
α	phase fraction (–)
Γ	mass transfer rate ($kg\ s^{-1}$)
ε	turbulence dissipation rate ($m^2\ s^{-3}$)
λ	thermal conductivity ($W\ m^{-1}\ K^{-1}$)
μ	dynamic viscosity (Pa s)
ν	kinematic viscosity ($m^2\ s^{-1}$)
Π	bulk interfacial heat transfer rate ($W\ m^{-3}$)
ρ	density ($kg\ m^{-3}$)
σ	surface tension ($N\ m^{-1}$)
τ	stress tensor (Pa)
<i>Subscripts</i>	
1, 2	liquid phase, vapor phase
i, j	cartesian tensor notation
k	arbitrary phase
K	Kolmogorov scale
sat	saturation
T	turbulent

efficiency of steam DCC phenomena in condensation pool depends on the sub-cooling of the pool liquid, the mass flux of injected vapor, drywell and wetwell volumes, the geometry of the vents and its corresponding exit shapes, and the fraction of non-condensables within the vapor.

As a whole, the discharge of steam into condensation pool is a quite intricate event which is associated with hydrodynamics and thermodynamics including bubble dynamics, thermal stratification, turbulent mixing, natural circulation, steam condensation within water pool, ducts, and at wall surfaces. The DCC of steam in water pool contains both the slow and very rapid time scale phenomena, which makes the analysis of condensation challenging either with experiments or numerical simulations (Tanskanen et al., 2014). Moreover, the rapid pressure oscillations resulting from steam condensation are generally unfavorable for the delicate measurement instrumentation and for the time-stepping of simulations. However, the steam blowdown experiments are important in order to enhance the understanding of physics involved in it.

Since the early '70s, several experimental studies of DCC of steam have been conducted. Some major experimental studies have been performed with vertical steam injection into condensation pool including various aspects, e.g., experiments done in the Marviken facility during 1972 to 1981 Wikdahl (2007), works of McIntyre et al. (1976), Grafton et al. (1977), Kennedy et al. (1978), Chan and Lee (1982), Aust and Seeliger, 1982, Nariai and Aya (1986), Walsche and Cachard (1996), Meier et al. (2000), the suppression pool experiments conducted with the PANDA (Smith, 2007) and LINX (Hart et al., 2001) experimental facilities, and Laine and Puustinen (2005) with the POOLEX. More details could be found in Tanskanen (2012) where he summarized the brief review of the experimental efforts conducted by other researchers on condensation pool experiments. More recently, experimental work has been performed by Puustinen et al. (2013) with the PPOOLEX facility aiming different issues of BWR containment. The POOLEX facility of Lappeenranta University of Technology (LUT) was an open wetwell facility with a long and straight blow-down pipe, and the PPOOLEX facility of LUT is a closed pressure vessel including drywell and wetwell.

Some extensive works were performed to classify the condensation modes in as regime maps e.g., Aya and Nariai (1987, 1991), Chan and Lee (1982), Liang and Griffith (1994) and de With et al.

(2007). A few works exist e.g., Aya and Nariai (1986) and Ali et al. (2007) in which analytical study of the oscillatory condensation modes is presented, including chugging.

Large scale computational fluid dynamics (CFD) simulations are now more affordable due to advancements in computational power. In the field of nuclear safety analysis, CFD has become an increasingly applicable tool for thermalhydraulic investigations (Bestion, 2012). Since 2000, gradual improvement in CFD simulations of chugging DCC in vertical vent pipes can be seen. For example, Meier et al. (2000, 2004) presented numerical study of large steam–air bubbles in a water pool without mass transfer by utilizing Volume of Fluid method. Further, Thiele (2010) tried VOF simulations with mass transfer based on temperature difference. Pättikangas et al. (2010) employed two-fluid Eulerian approach for PSP simulations with heat and mass transfer. Tanskanen (2012) and Tanskanen et al. (2014) simulated the STB-28 test done at POOLEX facility. Their results demonstrated the improved capability of Eulerian two-phase CFD codes to rather successfully predict chugging DCC in a blowdown pipe-wetwell system. In their work, a pattern recognition algorithm has been employed to extract the information of bubble size and bubble appearance frequency during the rapid chugging condensation mode. Pellegrini et al. (2015) conducted CFD simulations of chugging DCC of the same experiment of POOLEX facility. They proposed a method to treat the surface with growing instabilities based on the Rayleigh–Taylor theory. Tanskanen et al. (2015) presented a summary of their initial less successful simulations of the PPOOLEX DCC-05-4 test.

This paper presents the recent analysis of CFD simulations of the drywell–wetwell suppression pool system PPOOLEX. A set of numerical simulations have been performed with the CFD codes, NEPTUNE_CFD and OpenFOAM, in which a chugging DCC test case (DCC-05-4) is modeled by using the Eulerian two-fluid approach. In this work, the performance of different condensation models, the effects of turbulence modeling, interfacial area modeling, interfacial momentum transfer, geometry and interface initialization are analyzed. The significance of interfacial area modeling on the chugging DCC is tested by implementing Rayleigh–Taylor Interfacial (RTI) area model proposed by Pellegrini et al. (2015) to the NEPTUNE_CFD code. The pattern recognition data of a PPOOLEX test has been used here as a reference measurement of the bubble oscillations in the chugging condensation mode.

2. PPOOLEX DCC-05 experiment

The PPOOLEX test facility at LUT is a scaled down experimental facility for BWR containment safety related research. A schematic view of the PPOOLEX test facility is shown in Fig. 1. The PPOOLEX test facility consists both the drywell and wetwell (condensation pool) compartments of the containment.

The total height is 7.45 m and the inner diameter is 2.4 m. The main component of the facility is the approximately 31 m³ cylindrical test vessel. The drywell compartment is thermally insulated to prevent wall condensation. The test facility is able to resist overpressure up to 4 bar and underpressure of 0.5 bar. A DN100 blowdown pipe was used in the DCC-05 test. The blowdown pipe was positioned inside the wetwell compartment at a non-axisymmetric location (i.e. 420 mm apart from the center of pool). During the tests, the visual observation of the interior is possible via the windows on the side walls and in the bottom segment of the wetwell compartment.

Steam flow rate during the tests is measured with a vortex flow meter. The test facility is equipped with several thermocouples for measuring steam, pool water and structural temperatures and with pressure transducers for observing pressures in the drywell, inside the blowdown pipe(s), at the suppression pool bottom and in the gas phase of the wetwell. Standard instrumentation includes also strain gauges, vertical acceleration and movement transducers and valve position sensors. The drywell is equipped with a steam fraction measurement for estimating non-condensable gas presence.

The DCC-05 experiment was aimed to acquire test data for the validation of DCC models used in CFD codes and to obtain the multi-camera high speed video data of blowdown event to be used in the development work of pattern recognition algorithms. Therefore, the test facility included the system of three high speed cameras in order to capture the blowdown event of steam in water pool. Also, the temperatures were measured in various elevations within the blowdown pipe in order to achieve the frequency and the amplitude of steam/water interface oscillations.

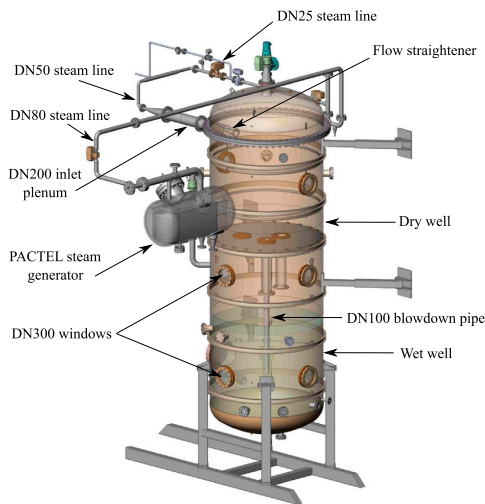


Fig. 1. PPOOLEX test facility (Puustinen et al., 2013).

The DCC-05 experiment was started in isothermal wetwell water (25°C) conditions so that the blowdown pipe outlet was submerged by ~1 m. During the clearing blow phase, practically all air was displaced from the drywell into the gas space of the wetwell after 500 s of the steam blowdown initiation. After that, the idea was to keep the pool water temperature rise as low as possible (rise of 10 K realized) but use a large range of different steam flow rates. Steam flow rates between 75 and 200 g s⁻¹ were used in the chugging blows of DCC-05 (Fig. 2).

The information about formation and break up of bubbles can be extracted by visual observation using a suitable pattern recognition algorithm. Tanskanen (2012) introduced a pattern recognition approach with which condensation rate in chugging DCC was analyzed indirectly from the video material of the suppression pool tests. However, the algorithm was based on a single camera output. For the DCC-05 PPOOLEX experiments, the introductory version of the pattern recognition algorithm was upgraded by Hujala (2013) to use three almost perpendicularly located high speed cameras. Volume of the bubbles were calculated by using bubble boundary data and numerical integration. From the data of the bottom camera an approximation, that the cross-sectional area of the bubbles is circular, can be estimated. The volume of the bubble can be measured by using cylindrical shaped plate elements of the height of single pixel. Each pixel row had its own diameter. Volume of a single row with the height of 1 pixel is easy to calculate. By collecting all the rows containing bubble pixels it was possible to estimate the volume of the bubble. The largest diameter seen in the side camera images should be the same as the diameter in the bottom camera image. Fig. 3 shows the recognized bubble volume in the DCC-05-4 experiment which was calculated by using pattern recognition.

In this work, Fast Fourier Transform (FFT) has been used to estimate the frequency of chugging motion from the recognized bubble volume obtained with pattern recognition. The FFT works best for purely periodic signals, therefore power spectrum of the volume data with peaks occurring at uneven time intervals tends to give multiple spikes with nearly equal frequencies. Fig. 4 shows the FFT from the recognized bubble volume in the DCC-05-4 experiment. It can be seen that the chugging frequencies are around 2 Hz, however, there are more energetic (larger) bubbles collapsing less frequently. A less distinguishable rapid interface oscillation of 50 Hz can be observed. This was result of the fluctuation or flickering of the interface at the natural frequency of oscillation before a bubble collapses (Brennen, 2014; Leighton, 1994).

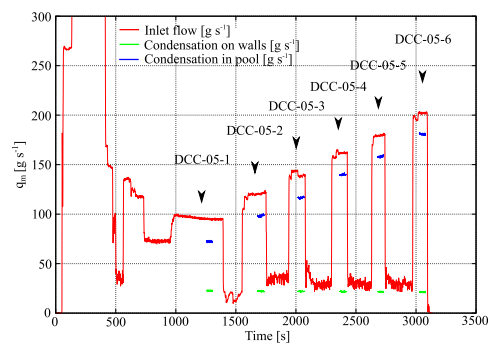


Fig. 2. Six chugging blows of the DCC-05 experiment (Tanskanen et al., 2015).

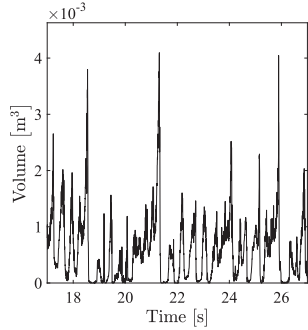


Fig. 3. The recognized bubble volume in the DCC-05-4 experiment.

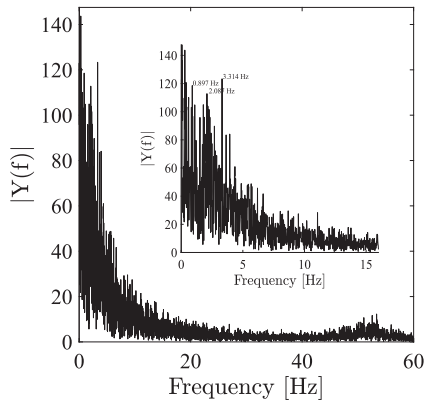


Fig. 4. FFT from the recognized bubble volume in the DCC-05-4 experiment.

3. Numerical models

3.1. Governing equations

The chugging phenomenon in vertical blowdown pipes is associated with strong pressure oscillations due to the extensive and rapid phase change. Also, most of the incompressible flow solvers of the computational fluid dynamics (CFD) software for two-phase system are inadequate in order to handle rapid and strong pressure oscillations of chugging phenomenon. Therefore, compressible flow formulation is favorable in such conditions (Tanskanen et al., 2015). In this study, the compressible flow Eulerian Finite Volume multi-field solver NEPTUNE_CFD (Bestion and Guelfi, 2005; Guelfi et al., 2007; Laviéville et al., 2006) version 2.0.1 utilizing CATHARE steam tables was used for chugging simulations. The OpenFOAM simulations were based on compressible two-flow solver of OpenFOAM 2.3.1. The equations for conservation of mass, momentum and energy in both CFD codes can be expressed as below, respectively:

$$\frac{\partial}{\partial t}(\alpha_k \rho_k) + \nabla \cdot (\alpha_k \rho_k \mathbf{U}_k) = \Gamma_k, \quad (1)$$

$$\frac{\partial}{\partial t}(\alpha_k \rho_k \mathbf{U}_k) + \nabla \cdot (\alpha_k \rho_k \mathbf{U}_k \mathbf{U}_k) = \alpha_k \nabla \cdot (\boldsymbol{\tau}_{k,ij} + \boldsymbol{\tau}_{k,ij}^t) - \alpha_k \nabla P + \alpha_k \rho_k \mathbf{g} + \mathbf{M}_k + \alpha_k \mathbf{S}_k, \quad (2)$$

$$\frac{\partial}{\partial t}(\alpha_k \rho_k H_k) + \nabla \cdot (\alpha_k \rho_k \mathbf{U}_k H_k) = \alpha_k \frac{\partial P}{\partial t} + \alpha_k \rho_k \mathbf{U}_k \mathbf{g} - \nabla \cdot (\alpha_k \mathbf{Q}_k) + \Gamma_k H_k + \Pi_k + q_{\text{wall},k}^{\prime\prime}, \quad (3)$$

Here, k indicates an arbitrary phase (later on $k = 1$ for liquid phase and $k = 2$ for vapor phase). In the momentum equation, $\boldsymbol{\tau}_{k,ij}$ and $\boldsymbol{\tau}_{k,ij}^t$ describe the molecular and turbulent stress tensors, respectively, \mathbf{M}_k indicates the interfacial momentum transfer between the phases, and \mathbf{S}_k denotes the external momentum source term. In this study, the \mathbf{M}_k term contains only the momentum transfer by a drag model i.e. the Large Interface Model 'Coste LIM' of Coste (2013) or the 'separated phase drag model' (Laviéville et al., 2006) in NEPTUNE_CFD simulations. The 'SN drag model' of Schiller and Naumann (1933) was used in OpenFOAM simulations, because it was the most suitable option of the already implemented models for gas–liquid flow. Despite of its limited applicability for fully separated phases, it produces reasonable drag if the reference bubble diameter value is adjusted to a suitable value. In this study, 1 mm bubble size was used as the reference based on the results of stable interface simulations of Patel et al. (2015). In the energy equation, \mathbf{Q}_k is the conductive heat flux.

3.2. Phase change and heat transfer modeling

By imposing the overall heat balance, the mass transfer due to the phase change at the steam–liquid interface can be calculated as

$$\Gamma_k = \frac{\Pi_1 + \Pi_2}{H_2 - H_1}. \quad (4)$$

In this work, the steam is in saturated state, therefore the vapor phase heat transfer contribution Π_2 is negligible. The interfacial heat transfer for liquid phase is defined as

$$\Pi_1 = a_i h_1 (T_{\text{sat}} - T_1). \quad (5)$$

Here, a_i is the interfacial area density which was calculated from the gradient of void fraction as

$$a_i = |\nabla \alpha_1|, \quad (6)$$

and h_1 is the heat transfer coefficient for the liquid phase which is calculated as

$$h_1 = \frac{\text{Nu}_1 \lambda_1}{L_1}. \quad (7)$$

For the Nusselt number in chugging simulations, the correlations predicting high condensation rates in separated flow cases have been promising (Tanskanen, 2012; Tanskanen et al., 2014). In this work, three Nusselt number correlations have been tested and their performance have been discussed. The details about Nusselt number correlations are listed below.

3.2.1. Hughes and Duffey model based on small eddies

The Hughes and Duffey model on small eddies (hereafter 'HD 1 model') is based on the surface renewal model of Hughes and Duffey (1991). The Nusselt number formulation is defined as

$$\text{Nu}_1 = \frac{2}{\sqrt{\pi}} \text{Re}_{K,1} \text{Pr}_1^{1/2}, \quad (8)$$

where $\text{Re}_{K,1}$ is the Reynolds number based on Kolmogorov length and velocity scales, L_K and V_K :

$$V_K = (\nu \varepsilon)^{1/4} \text{ and } L_K = \left(\frac{\nu^3}{\varepsilon}\right)^{1/4}. \quad (9)$$

3.2.2. Hughes and Duffey model based on large eddies

The 'HD 2 model' is the correlation of Hughes and Duffey (1991) based on the surface renewal theory of Banerjee (1978) which

includes the large eddies. The Nusselt number correlation for the HD 2 model can be presented as

$$\text{Nu}_1 = \frac{2}{\sqrt{\pi}} \text{Re}_{\tau,1}^{1/2} \text{Pr}_1^{1/2}, \quad (10)$$

where $\text{Re}_{\tau,1}$ is the turbulent Reynolds number which can be calculated as

$$\text{Re}_{\tau,1} = \frac{V_{\tau,1} L_{\tau,1}}{\nu_1}. \quad (11)$$

The turbulent velocity and length scales: V_{τ} and L_{τ} can be defined as

$$V_{\tau} = C_{\mu}^{1/4} k^{1/2} \quad \text{and} \quad L_{\tau} = \frac{C_{\mu}^{3/4} k^2}{\varepsilon}, \quad (12)$$

where the C_{μ} is the turbulence viscosity constant of the $k - \varepsilon$ model.

3.2.3. The Coste 2004 model

The Nusselt number formulation of the Coste continuous 'Coste C' model of Coste (2004) can be written as

$$\text{Nu}_1 = \text{Re}_{\tau,1}^{7/8} \text{Pr}_1^{1/2}, \quad (13)$$

where the turbulent velocity and length scales: V_{τ} and L_{τ} in the $\text{Re}_{\tau,1}$ are

$$V_{\tau} = \left(\frac{2}{3}k\right)^{1/2} \quad \text{and} \quad L_{\tau} = L_k = \left(\frac{\nu^3}{\varepsilon}\right)^{1/4}. \quad (14)$$

In the Coste C model, the V_{τ} is limited with $V_{\tau} = \min(|\mathbf{U}_1|, (\frac{2}{3}k)^{1/2})$.

3.2.4. Turbulence modeling

In the NEPTUNE_CFD simulations, flow turbulence was solved by employing the standard $k - \varepsilon$ turbulence model of Launder and Spalding (1974) for both phases. The equations of the turbulent kinetic energy and its dissipation can be written as follows,

$$\frac{\partial}{\partial t}(\rho_k k_k) + \nabla \cdot [\rho_k \mathbf{U}_k k_k - \left(\mu + \frac{\mu_t}{\sigma_k}\right) \nabla k] = \mathbb{P}_k + \mathbb{G}_k - \varepsilon_k + \Pi_{qk} \quad (15)$$

$$\begin{aligned} \frac{\partial}{\partial t}(\rho_k \varepsilon_k) + \nabla \cdot [\rho_k \mathbf{U}_k \varepsilon_k - \left(\mu + \frac{\mu_t}{\sigma_{\varepsilon}}\right) \nabla \varepsilon] \\ = C_{\varepsilon 1} \frac{\varepsilon_k}{k_k} [\mathbb{P}_k + (1 - C_{\varepsilon 3}) \mathbb{G}_k] - \rho_k C_{\varepsilon 2} \frac{\varepsilon_k^2}{k_k} + C_{\varepsilon 4} \frac{\varepsilon_k}{k_k} \Pi_{qk}. \end{aligned} \quad (16)$$

Here, μ_t is the turbulent viscosity, σ_k and σ_{ε} are the turbulent Prandtl numbers for k and ε , \mathbb{P} is the production of k , \mathbb{G} is the stratification attenuation term, and Π_q is the production or destruction of k due to the influence of other phases. The model constants are $\sigma_k = 1.0$, $\sigma_{\varepsilon} = 1.3$, $C_{\varepsilon 1} = 1.44$, $C_{\varepsilon 2} = 1.92$, $C_{\varepsilon 4} = 1.2$, $C_{\varepsilon 3} = 0$ if $\mathbb{G} \geq 0$ and $C_{\varepsilon 3} = 1$ if $\mathbb{G} < 0$. The turbulent viscosity μ_t is defined in the standard $k - \varepsilon$ model as

$$\mu_{t,k} = \rho_k C_{\mu} \frac{k_k^2}{\varepsilon_k}, \quad (17)$$

where $C_{\mu} = 0.09$.

In the OpenFOAM simulations, the $k - \varepsilon$ model is the one proposed by Lahey (2005). This ' $Lk - \varepsilon$ ' model was used for the continuous liquid phase turbulence. This model includes dispersed phase induced turbulence terms in the k and ε transport equations. In addition, the $Lk - \varepsilon$ model uses modified turbulent viscosity term written as

$$\mu_{t,1} = \rho C_{\mu} \frac{k_1^2}{\varepsilon_1} + C_{\mu} \alpha_2 d_2 |\mathbf{U}_1|, \quad (18)$$

where \mathbf{U}_1 indicates the relative velocity. Moreover, the $Lk - \varepsilon$ turbulence model contain the additional dispersed phase induced production terms $S_{k,1}$ and $S_{\varepsilon,1}$, respectively:

$$S_{k,1} = C_{p1} \frac{\alpha_1 \rho_1 \alpha_2}{d_2} \left[|\mathbf{U}_1 - \mathbf{U}_2|^3 + \left(\frac{C_d \text{Re}_d \nu_1}{d_2}\right)^{3/4} |\mathbf{U}_1 - \mathbf{U}_2|^{3/2} \right] + C_{12} k_2, \quad (19)$$

$$S_{\varepsilon,1} = C_3 S_{k,1} \frac{\varepsilon_1}{k_1} + C_{12} \varepsilon_2. \quad (20)$$

In Eq. (19), C_{p1} is the model constant and C_{12} is the transfer coefficient between the turbulence models of both the phases which is calculated from local phase fraction, gas phase turbulent time scale and simulation time step. More details about utilized turbulence models in OpenFOAM simulations can be found in Lahey (2005) and in Peltola (2015).

3.2.5. Rayleigh–Taylor instability (RTI) model

Generally, the interfacial area density is obtained from the gradient of volume fraction. However, the accuracy of this value depends on the grid resolution related to the interfacial details. The high accelerations cause interfacial instabilities e.g. Rayleigh–Taylor instability, which increase the interfacial roughness significantly. Pellegrini et al. (2015) proposed a simple model to treat the surface with growing instabilities based on the Rayleigh–Taylor theory. In the work of Pellegrini et al. (2015), the interfacial wave amplitude η was expressed as

$$\frac{d\eta}{dt} = n\eta, \quad (21)$$

where n is a function as $n = f(g, \kappa, A)$. Here, g is the acceleration (e.g. gravitational, but can be general as well), κ is the wave number and A is the Atwood number $\left(A = \frac{\rho_1 - \rho_2}{\rho_1 + \rho_2}\right)$.

Pellegrini et al. (2015) derived n from Duff et al. (1962) and Livescu (2004) as

$$n = \Re \left(\sqrt{\left(Ag - \frac{\sigma \kappa^2}{\rho_1 - \rho_2} \right) \kappa + \nu^2 \kappa^4 - \nu \kappa^2} \right), \quad (22)$$

where $\nu = \frac{\mu_1 + \mu_2}{\rho_1 + \rho_2}$. In two-fluid modeling, the interfacial area density is usually calculated as in Eq. 6. Using that, Pellegrini et al. (2015) simplified the area with approximation to square waves, therefore, the amplified length is expressed as

$$L = \sqrt{a_i \Delta v}, \quad (23)$$

where Δv indicates the cell volume. The amplified length is then obtained by adding the portion of wave as

$$L_{\text{amplified}} = L + \frac{kL\eta}{\pi}. \quad (24)$$

The interfacial area can be written as

$$a_{i,\text{amplified}} = \left(\frac{\kappa\eta + 1}{\pi}\right)^2 a_i. \quad (25)$$

Here, the wave number should be maximizing the wave growth. In order to simplify the calculation, Pellegrini et al. (2015) estimated it as

$$\kappa_{\text{max}} = \sqrt{\frac{Ag(\rho_1 + \rho_2)}{3\sigma}}. \quad (26)$$

The value of acceleration is calculated from the pressure gradient normal to the interface as

$$g = \frac{\nabla P \cdot \frac{\nabla \alpha_1}{|\nabla \alpha_1|}}{\rho}, \quad (27)$$

where, ρ refers to the average density of fluid in the interfacial cell. The amplitude of the wave is expressed as

$$\eta_t = \eta_{t-\Delta t} e^{\beta \Delta t} \quad (28)$$

As an initial perturbation, Pellegrini et al. (2015) used a small value i.e. $\eta_{t=0} = 10^{-5}$ m. In the current CFD implementation, the value of η is also limited by the cell size by using

$$\eta_t = \min(\eta_t, L) \quad (29)$$

4. Computational model and simulation set-up

A relatively long sample of transient had to be simulated in order to obtain enough data. As that was computationally time consuming in 3D simulations (Tanskanen et al., 2015), a 2D-axisymmetric representation of the PPOOLEX geometry was developed in the present study to make a greater case matrix possible.

4.1. Geometrical details and grid generation

A 2D-axisymmetric geometry containing a 1° sector of the PPOOLEX pool was modeled. Therefore, the grid of hexahedral cells was generated by rotating a quadrilateral grid to contain a single cell thickness in respect to z-axis. The main idea in the axisymmetric grid was to transfer the blowdown pipe to the center axis of the facility and the inlet plenum as well, but keep the other dimensions i.e. volumes of different parts of the pool unchanged. Due to the large size of the wetwell and relatively low inlet velocity, the inlet plenum re-location towards the blowdown pipe did not have significant effect on the phenomena in the wetwell (Tanskanen et al., 2016). Concerning the blowdown pipe relocation, the 2D simplification lost the likely asymmetric field of pool liquid circulation and asymmetric bubble shapes as well. However, the effect of these simplifications was assumed small due to the short samples simulated i.e. pool mixing remained weak, and due to the mainly symmetric bubbles which were observed when the DN100 blowdown pipe was used in the experiment.

In rapid condensation simulations, the interface area increase can be significant due to the acceleration by pressure decrease and chugging motion of the interface. This problem can be approached by two ways. First of these is a denser grid with which the interface details can be captured better. The second and more practical from the engineering point of view is an interface model that modifies the interfacial area density (Eq. (6)) to include the effect of increased interfacial area in the cases of coarse grids. The denser grid option was tested by making a grid able to capture at least the initial interfacial perturbation wave length of Rayleigh–Taylor instability in the DCC-05-4 case. The critical wave length can be calculated with (Ishii and Hibiki, 2011)

$$\lambda_c = 2\pi \sqrt{\frac{\sigma}{g(\rho_1 - \rho_2)}} \quad (30)$$

According to axial interface location data from the pattern recognition study of DCC-05-4 test, acceleration can be as high as $g = 500$ or even 1000 ms^{-2} . Then $\lambda_c = 2.2$ or 1.5 mm would be the corresponding critical wave lengths. Therefore, a grid with minimum 1 mm cell size was considered. The grid was refined inside the blowdown pipe and in the mouth region of the grid up to 1 mm . In order to analyze the other modeling issues on the chugging phenomenon, a similar but coarser grid with 5 mm cell size was used. Fig. 5 presents the 2D-axisymmetric geometry with the 5 mm grid. The grid with 1 mm cell size contained 273,200 computational cells, while the 5 mm cell size grid had 72,000 computational cells. These grids were suitable for standard wall functions as in the denser grid, $y^+ = 60$ inside the blowdown pipe. In

order to study the damping effect of the suppression pool drywell, a truncated geometry and grid without the drywell were made as well.

The sub-test DCC-05-4 was selected as the CFD validation case of this study. The initial and boundary parameters for the simulation of the case are listed in Table 1.

For the sake of simplicity, the wall condensation was not simulated in this study. The amount of wall condensation was estimated analytically using the correlation of Chen et al. (1987). The calculated value of wall condensate was deduced from the inlet mass flow rate to compensate its effect on the available steam mass flux in the blowdown pipe. Fig. 6 summarizes the initial temperature and pressure fields of the DCC-05-4 simulation.

In most of the simulations, the initial location of the steam-water interface at $t = 0 \text{ s}$ was set at elevation 1.8 m corresponding water level in pool inside the blowdown pipe. Therefore, the volume fraction of the vapor phase was set to unity inside the blow-

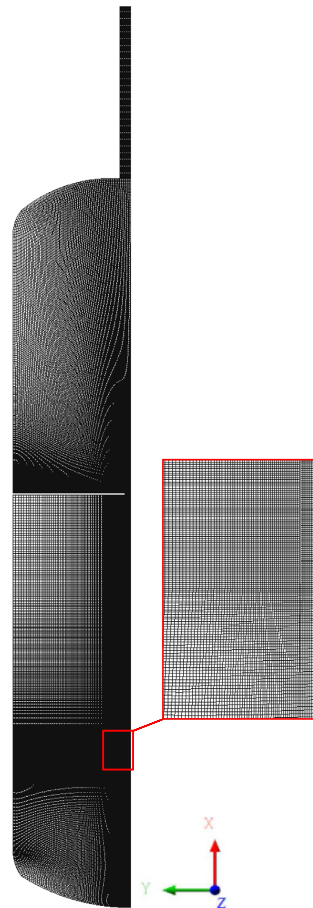


Fig. 5. 2D-axisymmetric representation of the PPOOLEX facility with 5 mm grid resolution.

Table 1
Initial and boundary conditions of DCC-05-4 simulation.

Maximum simulation duration	51 s (test sample)
Initial interface level in pipe	0.042 m or 1.03 m (above pipe outlet)
Water level in pool	1.03 m (above pipe outlet)
Initial drywell pressure	301310 Pa
Initial wetwell gas space pressure	293370 Pa
T_{sat} in drywell	406.8 K
T in drywell gas space	313.7–330 K
T in wetwell liquid	300.7–315.6 K (stratified)
T in water plug in pipe	374.3–405.6 K
Actual inlet mass flow rate	+0.1616 kg s ⁻¹ (mean)
Wall condensation estimation	-0.0217 kg s ⁻¹ (Chen et al., 1987)
Reduced inlet mass flow rate	+ 0.1399 kg s ⁻¹ (inlet BC.)
Inlet temperature	429.2 K
NC gas mass fraction in drywell gas space	0.984–0.964 (calculated)

down pipe up to 1.8 m. Some cases were also conducted with different steam-water interface initialization near blowdown pipe outlet in order to study the influence of interface initialization on chugging DCC. In all the simulations, the pool walls were considered to be adiabatic and a no-slip boundary condition was imposed at all the wall surfaces. In both the CFD codes, the 2D-axisymmetric unsteady CFD simulations were performed with the finite volume formulation. The code specific settings for the NEPTUNE_CFD 2.0.1 and OpenFOAM 2.3.1 are presented in Table 2.

The simulation case matrix and the varied parameters are presented in Table 3.

5. Results and discussion

The instantaneous condensation rate can not be measured reliably, but the characteristic phenomena like bubble size, bubble collapse rate and chugging frequency can be compared between experimental and simulation data qualitatively at least. The DCC rate depends on the chosen DCC model or correlation, interfacial

Table 2
CFD solver specific settings for the DCC-05-4 case.

NEPTUNE_CFD solver settings	
Predefined flow	Free-surface flow
Compressible	Phase 1: Yes, Phase 2: Yes
Energy resolution	Phase 1: Yes, Phase 2: Yes
Non-condensable gases	Off
Thermodynamics (tables)	Phase 1: Cathare Water L, Phase 2: Cathare Water V
Conjugate heat transfer	Off
Turbulence	Phase 1: $k-\epsilon$, Phase 2: $k-\epsilon$
Continuous phases coupling	Sep.phases with condensation
Interfacial momentum transfer	See Table 3
DCC model	See Table 3
Gravity	-9.81 ms ⁻²
Inlet thermal condition	Phase 1: $H_{sat}(P)$, Phase 2: $T_{imp} = 429.25$ k
Inlet D_h	0.2141 m
Navsto sub-cycles; Max. Alpha-P cycles	1; 50
Max. 1 - sum(z)	1e-8
Time step option	adaptive
Initial time step size	1e-5 s
CFL; FOU	1; 10
OpenFOAM solver settings	
Pressure-velocity coupling	PIMPLE
Compressible	Phase 1: Yes, Phase 2: Yes
Energy resolution	Phase 1: Yes, Phase 2: No
Non-condensable gases	No
Thermodynamics (tables)	No
Turbulence	Phase 1: $Lk-\epsilon$, Phase 2: $k-\epsilon$
Interfacial momentum transfer	See Table 3
DCC model	See Table 3
Gravity	-9.81 ms ⁻²
Max. 1 - sum(z)	1e-5
Time step option	adaptive
Initial time step size	1e-4 s
Courant number	< 1

area density modeling and subcooling rate. Of these, only the sub-cooling rate is assumed well initialized and modeled in the simulations. In this chapter, the effects of the DCC heat transfer model

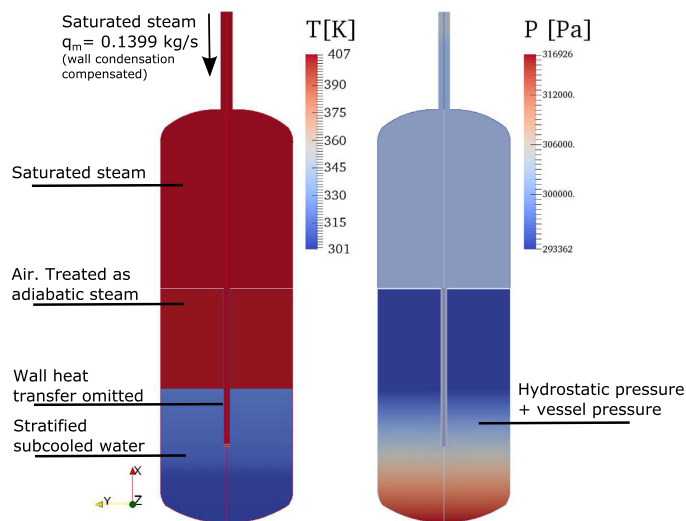


Fig. 6. Initial temperature and pressure fields in the simulations of the DCC-05-4 case.

Table 3
Simulation cases and varied parameters.

Case ID	Code	DCC model	Interfacial area density	Interfacial momentum transfer	Turbu. model	σ model	Initial interface location	Grid
CASE1	NE	Coste C	$ \nabla z_1 $	Coste LIM	sk- ϵ	none	w. level	5 mm
CASE2	NE	HD 1	$ \nabla z_1 $	Coste LIM	sk- ϵ	none	w. level	5 mm
CASE3	NE	HD 2	$ \nabla z_1 $	Coste LIM	sk- ϵ	none	w. level	5 mm
CASE4	NE	Coste C	$ \nabla z_1 $	Sep.Phases	sk- ϵ	none	w. level	5 mm
CASE5	OF	Coste C	$ \nabla z_1 $	SN	Lk- ϵ	none	w. level	5 mm
CASE6	NE	Coste C	$ \nabla z_1 $	Coste LIM	sk- ϵ	none	w. level	1 mm
CASE7	NE	Coste C	$ \nabla z_1 $ + RTI	Coste LIM	sk- ϵ	none	w. level	5 mm
CASE8	NE	Coste C	$ \nabla z_1 $	Coste LIM	sk- ϵ	none	near outlet	5 mm
CASE9	NE	Coste C	$ \nabla z_1 $	Coste LIM	sk- ϵ	none	near outlet	5 mm trunc.
CASE10	OF	Coste C	$ \nabla z_1 $	SN	Lk- ϵ	none	near outlet	5 mm
CASE11	OF	Coste C	$ \nabla z_1 $	SN	Lk- ϵ	none	w. level	5 mm trunc.
CASE12	NE	Coste C	$ \nabla z_1 $ + RTI	Sep.Phases	sk- ϵ	devel.	w. level	5 mm
CASE13	NE	Coste C	$ \nabla z_1 $ + RTI	Coste LIM	sk- ϵ	devel.	w. level	5 mm
CASE14	NE	HD 1	$ \nabla z_1 $ + RTI	Coste LIM	sk- ϵ	devel.	w. level	5 mm

NE = NEPTUNE_CFD; OF = OpenFOAM; Coste C = Coste (2004) continuous model; HD 1 = Hughes and Duffey (1991) model; HD 2 = Hughes and Duffey (1991) model based on large eddies; RTI = Rayleigh–Taylor instability model (Pellegrini et al., 2015).

Coste LIM = Large Interface Model of Coste (2013); Sep.Phases = separated phase drag model (Laviéville et al., 2006); SN = Schiller and Naumann (1933) drag model. sk- ϵ = standard $k-\epsilon$ turbulence model of Launder and Spalding (1974); Lk- ϵ = $k-\epsilon$ turbulence model of Lahey (2005); w. level = water level of the wetwell. devel. = under development/not validated; trunc. = truncated PPOOLEX geometry.

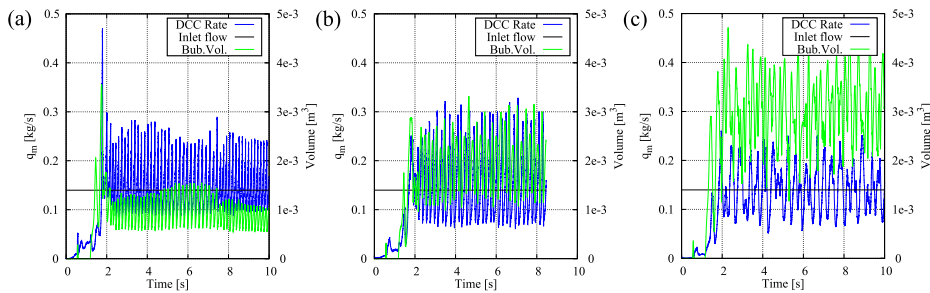


Fig. 7. DCC rates and bubble volumes in (a) CASE1, (b) CASE2, and (c) CASE3.

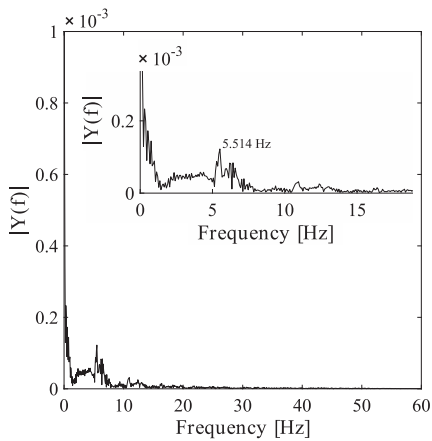


Fig. 8. FFT from the recognized bubble volume in the simulation of CASE1.

In general, turbulence kinetic energy within the DCC models and the interfacial area density modeling on the DCC rate is demonstrated. Furthermore, the sensitivity of chugging DCC to the initial

conditions and to the modeled domain is briefly tested. At the end of the chapter, the effect of interfacial momentum transfer closure modeling on the chugging is demonstrated.

5.1. Effect of DCC model

The DCC model of Coste (2004) and the NEPTUNE_CFD modification of Hughes and Duffey (1991) were proven promising in the chugging simulations of PPOOLEX blowdown pipe and wetwell system (Tanskanen, 2012). As to the results in the drywell–wetwell system of PPOOLEX, Fig. 7 summarizes the DCC rate and bubble size results of the basic cases.

Comparing the bubble volume data of Figs. 3 and 7, it can be seen that chugging did not occur in these simulations. Although the DCC rate was occasionally much higher than the inlet rate, it was due to the increase in the size of inflating bubble and not due to the interface ripping induced by rapid condensation. That is, even though the DCC rate was higher than the inlet rate, it was not still high enough to change the characteristic oscillating motion of non-condensing bubble towards actual chugging motion. After the CASE1, 2 and 3, the Rayleigh–Taylor instability model tests CASE7 and CASE14 were carried out. Based on the results, the highest DCC yielding model i.e. Coste (2004) was chosen as the default model for most of the simulation cases in this study. Fig. 8 shows the FFT of the bubble volume in the CASE1.

Power spectrum of bubble size in CASE1 is an example of the non-chugging cases. Compared this to the experimental data of

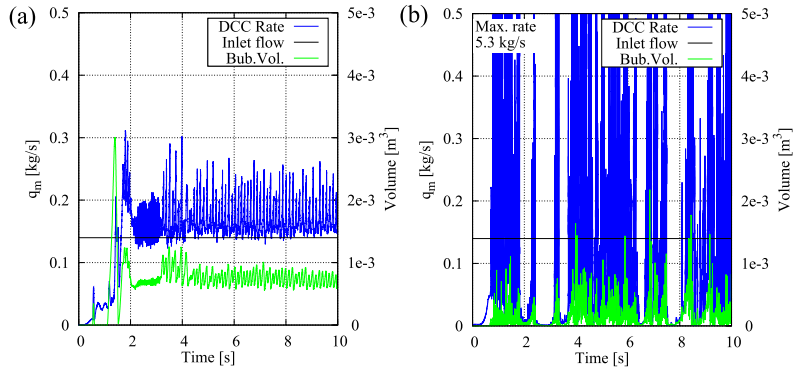


Fig. 9. DCC rates and bubble volumes in (a) CASE4 and (b) CASE5.

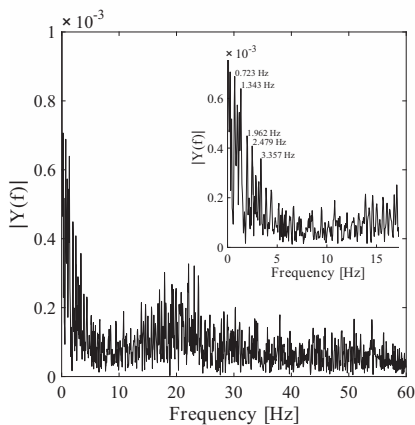


Fig. 10. FFT from the recognized bubble volume in the simulation of CASE5.

Fig. 4, the 0.5–3.3 Hz peak bunch is missing as well as the rapid interface oscillation of 50 Hz. Instead, a clear 5.5 Hz oscillation of permanently present bubble interface could be seen, demonstrating the absence of chugging.

5.2. Effect of turbulence modeling

The results of the DCC models used here are proportional to the velocity scale relative to the near interface turbulence kinetic energy or dissipation rate. The CASE4 in Fig. 9 was a NEPTUNE_CFD case with the standard $k-\varepsilon$ model, and the CASE5 was an OpenFOAM simulation with the $k-\varepsilon$ model of Lahey (2005), which should produce more turbulence kinetic energy. The momentum (drag) transfer models in these two cases were the basic separated phases models of the codes in order to make the case set-ups comparable between the codes.

As it should, the CASE4 result of NEPTUNE_CFD was very similar to the CASE1 result. Although bubble size was in CASE4 slightly smaller, the bubble stayed at the pipe outlet without chugging initiated. In the OpenFOAM CASE5, condensation rates were much

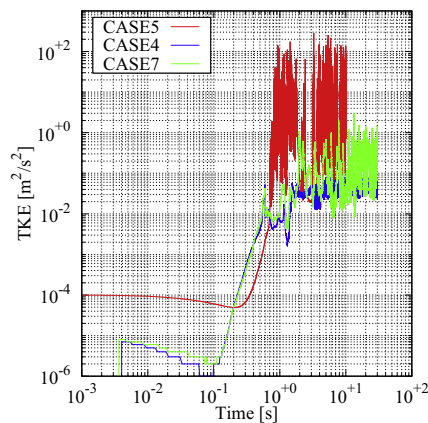


Fig. 11. Interfacial liquid turbulence kinetic energy level in CASE4, CASE5, and CASE7.

higher than in the cases with the standard $k-\varepsilon$ model. Bubbles collapsed and chugging occurred, but the frequency seemed too high and bubble sizes too small compared to the experiment. Fig. 10 shows the power spectrum of bubble size in the CASE5.

Some indications of 0.5–3.3 Hz frequencies of experiment could be seen in the CASE5, but the 20 Hz oscillation did not correspond to the test at all. Fig. 11 shows the interfacial turbulence kinetic energy history of the CASE4, CASE5 and CASE7.

The CASE4 could be considered as a case without chugging, the CASE5 as a case with too high chugging frequency and the CASE7 as a case with relatively correct chugging frequency. Turbulence kinetic energy near the interface was dramatically different between these cases, having the average orders of magnitude $10^{-2} \text{ m}^2 \text{ s}^{-2}$ in the CASE4, $10^{-1} \text{ m}^2 \text{ s}^{-2}$ in the CASE7 and $10^{-1} - 10^1 \text{ m}^2 \text{ s}^{-2}$ in the CASE5.

5.3. Effect of interfacial area modeling

In ideal CFD simulations, interfacial instabilities can be captured increasingly better by increasing the grid resolution to cover the

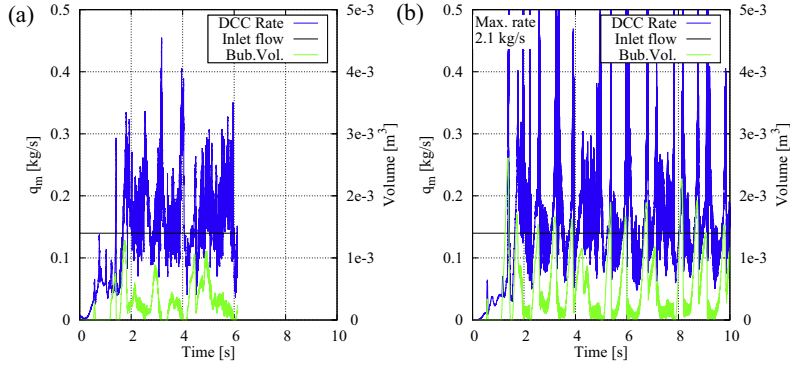


Fig. 12. DCC rates and bubble volumes in (a) CASE6 and (b) CASE7.

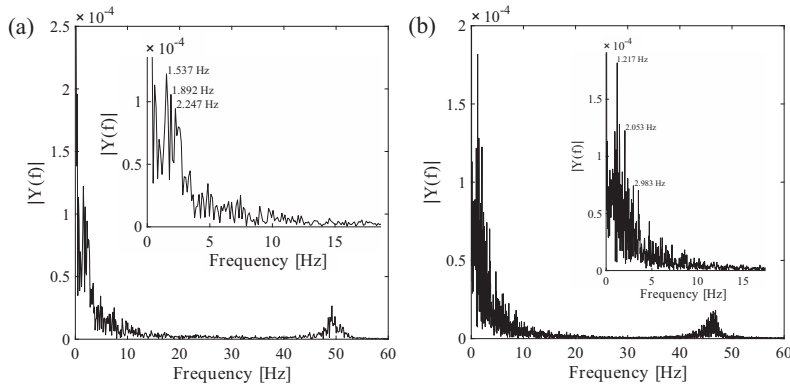


Fig. 13. FFT from the recognized bubble volume in the simulation of (a) CASE6 and (b) CASE7.

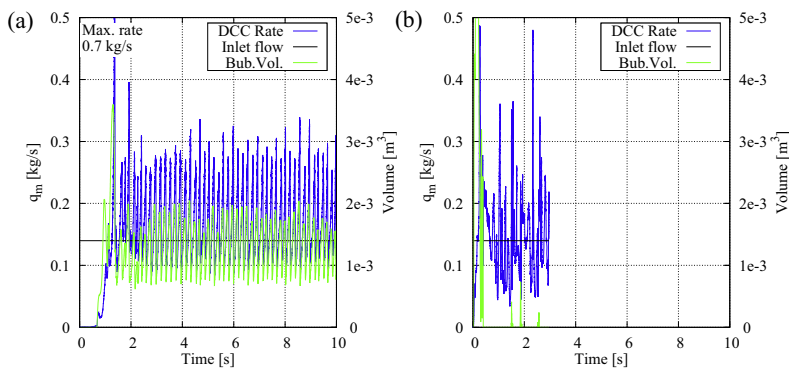


Fig. 14. DCC rates and bubble volumes in (a) CASE8 and (b) CASE9.

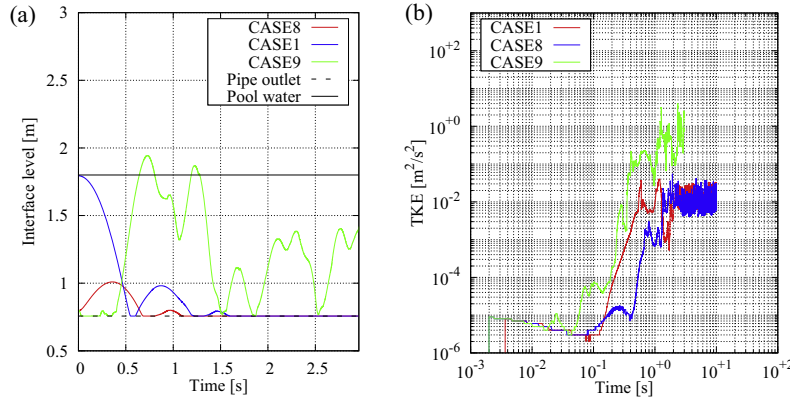


Fig. 15. (a) Interface level inside the blowdown pipe (left), and interfacial liquid turbulence kinetic energy level in CASE1, CASE8, and CASE9.

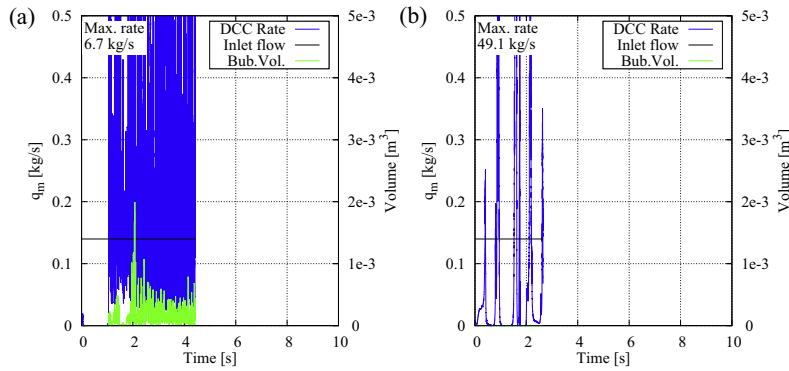


Fig. 16. DCC rates and bubble volumes in (a) CASE10 and (b) CASE11.

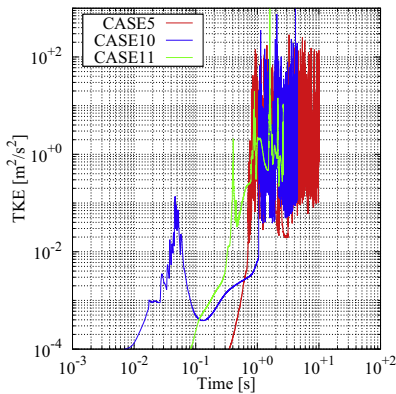


Fig. 17. Interfacial liquid turbulence kinetic energy level in CASE5, CASE10, and CASE11.

critical wave lengths of invoking instabilities, e.g. the Rayleigh–Taylor instability at first, then the Kelvin–Helmholz instability on the waves generated by the Rayleigh–Taylor one etc. The grid resolution in the CASE6 (Fig. 12) was good enough to capture the critical wave length of the Rayleigh–Taylor instability calculated from the recognized interface acceleration in the experiment. As it was not ideal in engineering sense to use such or even denser grids in the simulations, thus the Rayleigh–Taylor instability was modeled in the CASE7 (Fig. 12) by using the Pellegrini et al. (2015) model in the same coarse grid set-up as in the other cases in this paper.

Chugging occurred in both the cases CASE6 and CASE7, as the resolved or modeled increasing interfacial area increased the condensation rate, which in turn led to interface collapse and thus to cyclic process. The power spectra of bubble volumes in these two cases are shown in Fig. 13.

It was quite trivial to calculate volumes and interfacial areas during the CFD simulations, while the corresponding operation for the video material from the experiment tended to lose details of interface and structures beyond the visible interface. Taking this in the account, the FFT result of bubble volumes in the CASE6 and

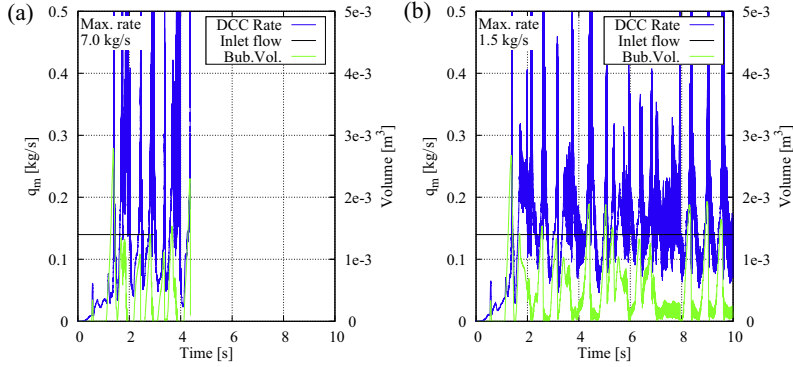


Fig. 18. DCC rates and bubble volumes in (a) CASE12 and (b) CASE13.

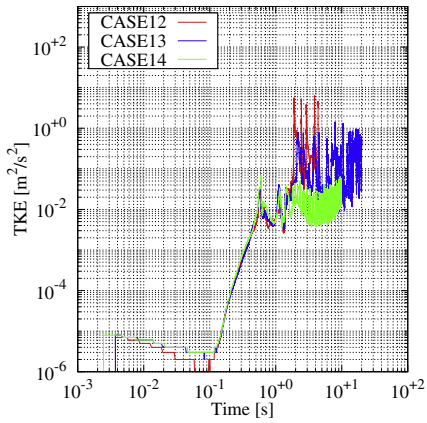


Fig. 19. Interfacial liquid turbulence kinetic energy level in CASE12, CASE13, and CASE14.

CASE7 were outstandingly near the experimental result of Fig. 4. In both the cases a group of maxima could be seen at 1–3 Hz and also the rapid oscillation of 50 Hz, indicating chugging.

5.4. Effect of geometry and interface initialization

One may ask why the chugging occurred in the simulations of a straight tube POOLEX experiment (Tanskanen, 2012; Tanskanen et al., 2014), although the grid was coarse and not any special interfacial instability modeling was applied. Tanskanen (2012) mentioned that the level of initial interface inside the blowdown pipe matters as a long traverse of interface and water plug before the first bubble generates lot of turbulence near the blowdown pipe exit, which initiates chugging more easily. The CASE8 in Fig. 14 demonstrated the effect of initial interface set near to the blowdown pipe outlet, which is in fact the correct location based on the starting point of experimental data of the DCC-05-4 subtest. The CASE9 in Fig. 14 was a test without the drywell taken into account i.e. drywell was removed from the geometry and massflow boundary condition was brought from the inlet plenum to the inlet of blowdown pipe.

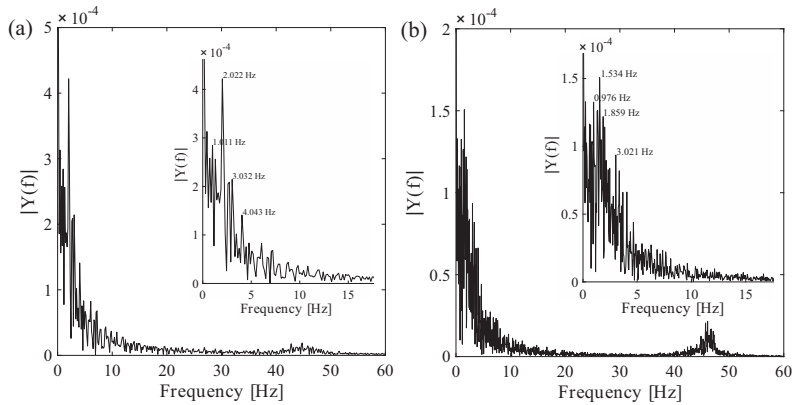


Fig. 20. FFT from the recognized bubble volume in the simulation of (a) CASE12 and (b) CASE13.

The CASE8 could be compared to the one of CASE1, as the initial interface location was the only difference. Results were almost identical apart from the first 2s of simulations. With the higher initial level (CASE1), there was one chug before the stabilization, while the CASE8 was stabilized immediately. The CASE9 set-up without drywell led to vigorous chugging with interface mostly churning inside the blowdown pipe. Fig. 15 (a) shows the interface location inside the blowdown pipe in the CASE1, CASE8 and CASE9.

The CASE8 started with a small upward motion of interface before the downward motion, bubble eruption, and stabilization. The CASE1 started with the downward motion, bubble eruption, collapse and then with similar stabilizing cycle as in the CASE8. At the end, the interfacial turbulence kinetic energy was same in both the cases as seen in Fig. 15(b). In the CASE9, a large bubble erupted immediately, after which interface collapsed deeply up to the blowdown pipe causing internal churning and low-frequency external chugging. Probably the internal motion increased the interfacial turbulence kinetic energy to the range of $10^{-1} \text{ m}^2 \text{ s}^{-2}$ in the CASE9. Although there was chugging in the CASE9, it was qualitatively different than in the experiment. The corresponding OpenFOAM results with the $k-\varepsilon$ model of Lahey (2005) are presented in Figs. 16 and 17.

Lower initial interface level did not help in the CASE10 as the maximum condensation rate was even higher than in the high initialization of CASE5. That is, chugging occurred, but the frequency was much higher than in the experiment. The drywell was removed in the OpenFOAM CASE11, which led to results without externally visible chugging as the steam condensed tremendously inside the blowdown pipe.

While the turbulence in the standard $k-\varepsilon$ cases was strongly affected by the truncation of geometry, the turbulence was quite equally high in the $Lk-\varepsilon$ cases. However, the geometry change itself was more interesting issue as the turbulence level was likely just a mere consequence of that. That is, there was not any more damping effect of such a large gas space without drywell. In practice this meant that soft 'pressure boundary condition' at blowdown pipe inlet changed to a rigid velocity boundary condition, which did not respond to the changes in the condensation rate. This led to rapid loss of steam inside the pipe leading to internal chugging which was further maintained by the strong turbulence generation by the wall shear stress within the blowdown pipe.

5.5. Effect of interfacial momentum transfer model

The CASE12, CASE13 and CASE14 were included to this study in order to test the effect of interfacial momentum transfer modeling assuming that the interfacial instability modeling would be in any case crucial for good results. Fig. 18 shows the DCC rate and bubble volume results for the CASE12 and CASE13.

The only difference between the CASE13 and CASE7 set-up was that the surface tension modeling was attempted in the CASE13. Effect of surface tension should not be very remarkable in the set-up studied, and the results were very similar. The chugging rate in the CASE13 (Fig. 20) was near to the one of CASE7. The result of CASE12 with the basic separated phase drag model (with surface tension) differed from the Coste LIM CASE7 and CASE13 in some extent. The simpler separated phases drag model took into account only the normal interfacial component of the drag, while the Coste LIM model would be able to calculate tangential friction as well. However, the turbulence kinetic energy rose occasionally higher with the basic separated phase drag model as seen in Fig. 19. Chugging occurred in the CASE12, but the rapid fluctuation phase of 50 Hz was less evident (Fig. 20).

A typical chugging cycle from a large bubble to rapid collapse and to a new eruption is presented in Fig. 21 for the CASE13. The

corresponding DCC rate and bubble size in the CASE13 are presented as well. It can be seen that a large steam bubble was formed at the blowdown pipe outlet in Fig. 21(a), and it rapidly condensed due to preferably high enough condensation rates (Fig. 21(b)). Following the collapse of steam bubble, the steam/water interface was retreated inside the blowdown pipe in Fig. 21(c), but a toroidal bubble formed in Fig. 21(d). The most of small amplitude high

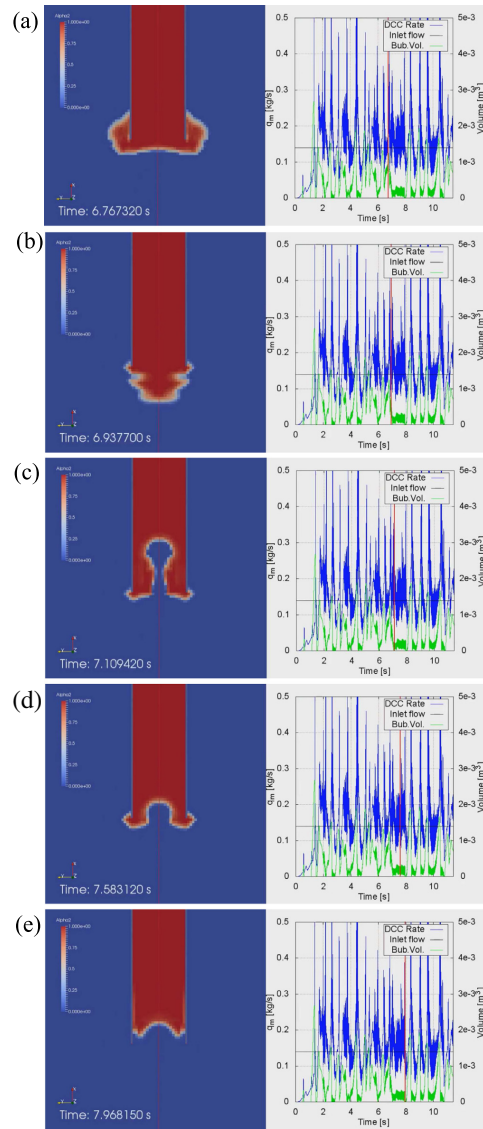


Fig. 21. Instantaneous steam volume fraction, corresponding DCC rates and bubble volumes in CASE13.

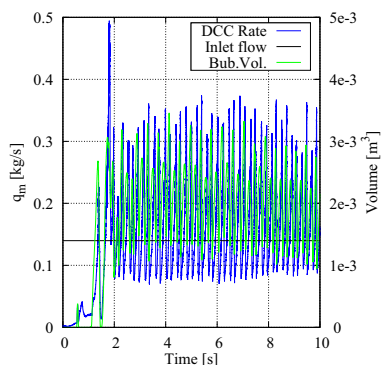


Fig. 22. DCC rates and bubble volumes in CASE14.

frequency oscillations seemed to occur in this phase, after which the toroidal bubble collapsed also as seen in Fig. 21(e) prior to the initial large bubble of a new cycle.

The results presented in this study suggest that the interfacial instability computation is the most crucial part of the DCC modeling of chugging condensation mode. Thus it was necessary to present the result of the second best DCC model (HD 1) with the Rayleigh–Taylor instability model applied (Fig. 22).

The HD 1 DCC model did not provide enough condensation in the CASE14, and the result was as poor as in the CASE2 even though the Rayleigh–Taylor instability modeling had been applied.

6. Conclusions

Modeling of chugging in a BWR suppression pool is numerically challenging due to the rapid condensation which leads to high velocities and pressure oscillations. In CFD, these lead to short time-stepping and high grid resolution requirements. In the reasonable engineering scales, these requirements could be met only partially which gives room for the other incompleteness in the required closure models.

Earlier work on the open-top suppression pool cases has shown that direct contact condensation mass transfer modeling requires an interface heat transfer model that provides high enough heat transfer rates. It was shown later that even relatively low heat transfer rates could be enough in these cases if the interface instability modeling is sufficient.

This work shows that physically justified yet simple modeling of interfacial waves (instabilities) necessarily improves the prediction of chugging in most cases but it is not the most dominant factor in the simulations including the drywell system as well.

Pattern recognition analysis of the PPOOLEX data was used to obtain chugging bubble frequencies. Numerical simulation with the Coste (2004) DCC model and Rayleigh–Taylor instability model yielded bubble frequencies in excellent agreement with the data. The performance of the Rayleigh–Taylor instability model was comparable to the corresponding dense grid simulations without the need of instability modeling. However, certain high enough DCC heat transfer rate was required in order to invoke chugging regardless of interfacial instability modeling. The standard $k-\epsilon$ model was applied in the most successful simulations, because e.g. the Lahey (2005) modification of $k-\epsilon$ model led to too high turbulence and thus too high chugging rate. The interfacial momentum transfer models (drag, surface tension...) and the ini-

tial state of the simulations have visible effects on the results, but these modeling issues are not as dominant factor in successful simulations as the DCC model, the interfacial area modeling and the turbulence modeling.

In addition to the FFT results shown here, more information can still be gathered from the pattern recognition and measurement data of the DCC-05 test. With that data, the analysis presented here could be sharpened. Otherwise, the next step in improving chugging modeling is to validate the best model combinations in 3D simulations and with other pipe geometries, even with spargers.

Acknowledgements

The research leading to these results is partly funded by the European Atomic Energy Community's (Euratom) Seventh Framework Programme FP7/2007-2011 under grant agreements No. 232124 and No. 323263. The research is also funded partly by the Finnish Nuclear Waste Management Fund (VYR) via The Finnish Research Programmes on Nuclear Power Plant Safety SAFIR2010, SAFIR2014 and SAFIR2018, and the Academy of Finland via the Doctoral Programme for Nuclear Engineering and Radiochemistry (YTERA). The authors gratefully acknowledge all this support. The authors would like to acknowledge the CSC-IT Center for Science, Finland for providing the scientific computing platform.

References

- Ali, S.M., Verma, V., Ghosh, A.K., 2007. Analytical thermal hydraulic model for oscillatory condensation of steam in presence of air. *Nucl. Eng. Des.* 237, 2025–2039.
- Aust, E., Seeliger, D., 1982. Pool dynamics and dynamic loads in pressure suppression containment systems. *Trans. Am. Nucl. Soc.* 41, 696–699.
- Aya, I., Nariai, H., 1986. Occurrence threshold of pressure oscillations induced by steam condensation in pool water. *Bull. JSME* 29 (235), 2131–2137.
- Aya, I., Nariai, H., 1987. Boundaries between regimes of pressure oscillation induced by steam condensation in pressure suppression containment. *Nucl. Eng. Des.* 99, 31–40.
- Aya, I., Nariai, H., 1991. Evaluation of heat-transfer coefficient at direct contact condensation of cold water and steam. *Nucl. Eng. Des.* 131, 17–24.
- Banerjee, S., 1978. A surface renewal model for interfacial heat and mass transfer in transient two-phase flow. *Int. J. Multiph. Flow* 4, 571–573.
- Bestion, D., 2012. Applicability of two-phase CFD to nuclear reactor thermalhydraulics and elaboration of best practice guidelines. *Nucl. Eng. Des.* 253, 311–321.
- Bestion, D., Gueffi, A., 2005. Status and perspective of two phase flow modelling in the NEPTUNE multiscale thermalhydraulic platform for nuclear reactor simulation. *Nucl. Eng. Technol.* 37 (6), 511–524.
- Brennen, C., 2014. *Cavitation and Bubble Dynamics*. Cambridge University Press, ISBN 978-1-107-64476-2.
- Chan, C.K., Lee, C.K.B., 1982. A regime map for direct contact condensation. *Int. J. Multiph. Flow* 8, 11–20.
- Chen, S., Gerner, F., Tien, C., 1987. General film condensation correlations. *Exp. Heat Transfer* 1, 93–107.
- Coste, P., 2004. Computational simulation of multi-d liquid-vapor thermal shock with condensation. In: *Proceedings of ICMF04, Yokohama, Japan, May 30–June 4*.
- Coste, P., 2013. A large interface model for two-phase CFD. *Nucl. Eng. Des.* 255, 38–50.
- de With, A.P., Calay, R.K., de With, G., 2007. Three-dimensional condensation regime diagram for direct contact condensation of steam injected into water. *Int. J. Heat Mass Transfer* 50, 1762–1770.
- Duff, R., Harlow, F., Hirt, C., 1962. Effects of diffusion on interface instability between gases. *Phys. Fluids* 5 (4), 417–425.
- Grafton, W.A., McIntyre, T.R., Ross, M.A., 1977. Mark II Pressure Suppression Test Program, Phase II and III tests: Technical Report. Boiling Water Reactor Projects Dept, General Electric Co., San Jose, CA, USA.
- Gueffi, A., Bestion, D., Boucker, M., Boudier, P., Fillion, P., Grandotto, M., Hérard, J.M., Hervieu, E., Péturaud, P., 2007. NEPTUNE: A new software platform for advanced nuclear thermal hydraulics. *Nucl. Sci. Eng.* 156, 281–324.
- Hart, J., Slegers, W.J.M., de Boer, S.L., Huggenberger, M., Jimenez, J.L., Gonzalez, J.L.M. C., Puigjaner, F.R., 2001. TEPSS—technology enhancement for passive safety systems. *Nucl. Eng. Des.* 209 (1–3), 243–252.
- Hughes, E.D., Duffey, R.B., 1991. Direct contact condensation and momentum transfer in turbulent separated flows. *Int. J. Multiph. Flow* 17, 599–619.
- Hujala, E., 2013. Evaluation of Bubble Formation and Break Up in Suppression Pools by Using Pattern Recognition Methods (Master thesis). Lappeenranta University of Technology, LUT Energy, Lappeenranta, Finland.

- Ishii, M., Hibiki, T., 2011. *Thermo-Fluid Dynamics of Two-Phase Flow*. Springer Science+Business Media, ISBN 978-1-4419-7984-1, e-ISBN 978-1-4419-7985-8.
- Kennedy, W., McGovern, D., Maraschin, R., Wolfe, K., 1978. Rigid and flexible vent header testing in the quarter scale test facility. Mark I Containment Program, Task 5.3.3. Technical Report. Acurex Corp., Alternate Energy Div, Mountain View, CA, USA.
- Lahey, R., 2005. The simulation of multidimensional multiphase flows. *Nucl. Eng. Des.* 235, 1043–1060.
- Lahey, R., Moody, F., 1993. *The Thermal-Hydraulics of a Boiling Water Reactor*. American Nuclear Society.
- Laine, J., Puustinen, M., 2005. Condensation Pool Experiments with Steam using DN200 Blowdown Pipe. NKS-111 ISBN 87-7893-171-1. Lappeenranta University of Technology.
- Lauder, B., Spalding, D., 1974. The numerical computation of turbulent flows. *Comput. Methods Appl. Mech. Eng.* 3 (2), 269–289.
- Laviéville, J., Quémérais, E., Mimouni, S., Boucker, M., Méchitoua, N., 2006. NEPTUNE CFD V1.0 theory manual: Technical Report. EDF.
- Leighton, T., 1994. *The Acoustic Bubble*. Academic Press, ISBN 978-0-12-441920-9.
- Liang, K., Griffith, P., 1994. Experimental and analytical study of direct contact condensation of steam in water. *Nucl. Eng. Des.* 147, 425–435.
- Livescu, D., 2004. Compressibility effects on the Rayleigh-Taylor instability growth between immiscible fluids. *Phys. Fluids* 16 (1), 118–127.
- McIntyre, T.R., Ross, M.A., Myers, L.L., 1976. Mark II pressure suppression test program: Phase I tests. [BWR]: Technical Report. Boiling Water Reactor Systems Dept., General Electric Co., San Jose, CA, USA.
- Meier, M., Yadigaroglu, G., Andreani, M., 2000. Numerical and experimental study of large steam-air bubbles injected in a water pool. *Nucl. Sci. Eng.* 136, 363–375.
- Nariai, H., Aya, I., 1986. Fluid and pressure oscillations occurring at direct contact condensation of steam flow with cold water. *Nucl. Eng. Des.* 95, 35–45.
- Patel, G., Tanskanen, V., Rintala, V., Hyvärinen, J., 2015. Numerical study of direct contact condensation of steam on stable interface in a BWR suppression pool test facility. In: *The 16th International Topical Meeting on Nuclear Reactor Thermal Hydraulics (NURETH-16)*, Chicago, IL, August 30–September 4, 14.
- Pättikangas, T., Niemi, J., Laine, J., Puustinen, M., Purhonen, H., 2010. CFD modelling of condensation of vapor in the pressurized PPOOLEX facility. In: *CFD for Nuclear Reactor Safety Applications (CFD4NRS-3) Workshop*, Bethesda, MD, USA, 14–16 September 2010, 12.
- Pellegrini, M., Naitoh, M., Josey, C., Baglietto, E., 2015. Modeling of Rayleigh-Taylor instability for steam direct contact condensation. In: *The 16th International Topical Meeting on Nuclear Reactor Thermal Hydraulics (NURETH-16)*, Chicago, IL, August 30–September 4, 15.
- Peltola, J., 2015. OpenFOAM 2.3.1 twoPhaseEulerFoam and twoPhaseNuFoam v0.6 extension to simulation of subcooled nucleate boiling: Technical Report. VTT.
- Puustinen, M., Kyrki-Rajamäki, R., Tanskanen, V., Räsänen, A., Purhonen, H., Riikonen, V., Laine, J., Hujala, E., 2013. BWR suppression pool studies with POOLEX and PPOOLEX test facilities at LUT. In: *The 15th International Topical Meeting on Nuclear Reactor Thermal Hydraulics (NURETH-15)*, Pisa, Italy, 12–17 May 2013.
- Schiller, L., Naumann, A., 1933. Über die grundlegenden berechnungen bei der schwerkraftbereitung. *Z. Vereins deutscher Ing.* 77, 318–320.
- Smith, B.L., 2007. A numerical investigation of three-dimensional flows in large volumes in the context of passive containment cooling in BWRS. *Nucl. Eng. Des.* 237 (11), 1175–1184.
- Tanskanen, V., 2012. CFD modelling of direct contact condensation in suppression pools by applying condensation models of separated flow. *Acta Universitatis Lappeenrantaensis* 472. Lappeenranta University of Technology. ISBN 978-952-265-221-8, ISBN 978-952-265-222-5 (PDF), ISSN 1456-4491.
- Tanskanen, V., Jorden, A., Puustinen, M., Kyrki-Rajamäki, R., 2014. CFD simulation and pattern recognition analysis of the chugging condensation regime. *Ann. Nucl. Energy* 66, 133–143.
- Tanskanen, V., Patel, G., Puustinen, M., Hujala, E., Kyrki-Rajamäki, R., Hyvärinen, J., 2015. CFD modelling of chugging condensation regime of BWR suppression pool experiments. In: *The 16th International Topical Meeting on Nuclear Reactor Thermal Hydraulics (NURETH-16)*, Chicago, IL, August 30–September 4, 14.
- Tanskanen, V., Hujala, E., Puustinen, M., 2016. Numerical simulation of a PPOOLEX chugging case with a Rayleigh-Taylor instability model for interfacial area: Research Report INSTAB 4/2015. LUT.
- Thiele, R., 2010. Modeling of direct contact condensation with OpenFOAM (Master thesis). KTH, Royal Institute of Technology, Division of Nuclear Reactor Technology, Royal Institute of Technology, Stockholm, Sweden. ISBN 0280-316X.
- Walsche, C.D., Cachard, F.D., 1996. Experimental investigation of condensation and mixing during venting of a steam/non-condensable gas mixture into a pressuresuppression pool. Technical Report. IAEA Report, 53–61.
- Wikdahl, C.E., 2007. Marvikenreaktor – ett industripolitiskt utvecklingsprojekt i otakt med tiden. Technical Report SKI Rapport 2007:18. SKI.
- Yadigaroglu, G., 2004. Computational Fluid Dynamics for nuclear applications: from CFD to multi-scale CMFD. *Nucl. Eng. Des.* 235, 153–164.



Contents lists available at ScienceDirect

Nuclear Engineering and Design

journal homepage: www.elsevier.com/locate/nucengdes

Corrigendum to Direct contact condensation modeling in pressure suppression pool system [Nuclear Engineering and Design 321 (2017) 328–342]

G. Patel, V. Tanskanen¹, E. Hujala, J. Hyvärinen

LUT School of Energy Systems/Nuclear Engineering, Lappeenranta University of Technology (LUT), PO Box 20, FIN-53851 Lappeenranta, Finland

The authors regret that two mistyped equations are remaining in the final publication. The Eqs. (22) and (25) were mistyped. The correct form of the Eq. (22) is

$$n = \Re \left(\sqrt{\left(Ag - \frac{\sigma \kappa^2}{\rho_1 + \rho_2} \right) \kappa + v^2 \kappa^4 - v \kappa^2} \right), \quad (22)$$

where (-) sign between ρ_1 and ρ_2 is replaced with (+) sign. The error should have only minor effect in the case of heavy fluid as phase 1 and light fluid as phase 2. Error was not present in the calculation model of the authors, only in the equation presented in the publication.

The correct form of the Eq. (25) is

$$a_{i,\text{amplified}} = \left(\frac{\kappa \eta}{\pi} + 1 \right)^2 a_i. \quad (25)$$

In the mistyped version of the Eq. (25) term (+ 1) was in the nominator instead of being outside. The error would have major impact to the results. However, this error was not present in the calculation model of the authors, only in the equation presented in the publication.

The authors would like to apologise for any inconvenience caused.
DOI of original article: <http://dx.doi.org/10.1016/j.nucengdes.2016.08.026>

DOI of original article: <http://dx.doi.org/10.1016/j.nucengdes.2016.08.026>

¹ Lappeenranta University of Technology (LUT)

E-mail address: vesa.tanskanen@lut.fi (V. Tanskanen).

<https://doi.org/10.1016/j.nucengdes.2018.01.038>

Publication IV

E. Hujala, V. Tanskanen, G. Patel and J. Hyvärinen

Image analysis of bubbling mode condensation oscillations in horizontal sparger

Reprinted with permission from

Proceedings of the 18th International Topical Meeting on Nuclear Reactor Thermal Hydraulics (NURETH-18), 2019

© 2019, American Nuclear Society (ANS)

IMAGE ANALYSIS OF BUBBLING MODE CONDENSATION OSCILLATIONS IN HORIZONTAL SPARGER

Elina Hujala, Vesa Tanskanen, Giteshkumar Patel and Juhani Hyvärinen

Nuclear Engineering, LUT School of Energy Systems, Lappeenranta-Lahti University of Technology LUT, Yliopistonkatu 34, 53850 Lappeenranta, Finland

Elina.Hujala@lut.fi, Vesa.Tanskanen@lut.fi, Giteshkumar.Patel@lut.fi, Juhani.Hyvarinen@lut.fi

ABSTRACT

Pattern recognition based image analysis algorithm was developed for analyzation of bubbling mode condensation oscillations in horizontal spargers. Safety relief valve test rig SEF-POOL was filled with a heated up (85 °C) water. The high mass flux steam (180 kg/(m²s) was pushed through a horizontal sparger (16 mm). The SEF-INF2 experiment was recorded using a high-speed video camera with a frame rate of 2800 fps. An improved image processing and analysis procedure have been applied to the video material. A new algorithm can deal with multiple simultaneous bubbles that can disappear for a while during the condensation. Features of the oscillating bubbles, e.g. formation frequency, lifetime, surface velocity, and acceleration, have been evaluated. The evaluated properties of the bubbles were also applied to CFD simulations, where the algorithm was used to determine critical wavelengths in succession to establish the most suitable grid density for the simulations. The preliminary results look promising. A large frame rate (2800 fps) yields significant information about condensation oscillations. Consequently, the bubble properties and oscillations are captured better than before. The accuracy of the pattern recognition algorithm has also been increased. 67 bubbles were tracked. Bubble mean lifetime was 0.0247 s, mean time difference between bubble formations was 0.0140 s which corresponds to 71.6 Hz formation frequency. 2D surface velocities and accelerations can now be estimated in all angles, which makes image analysis an effective tool in validation efforts of interfacial area and heat transfer models for numerical.

KEYWORDS

two-phase flow, image analysis, condensation oscillation, sparger

1. INTRODUCTION

All operating boiling water reactors (BWRs) use pressure suppression containment [1]. Usually, two kinds of steam injection mechanisms are used: the safety/relief valve (SRV) spargers and the blowdown pipes. The use of these mechanisms during normal operation or in a possible loss-of-coolant accident (LOCA) may cause structural loads to the suppression pool due to the rapid condensation of the steam. Experimental research and computational fluid dynamics (CFD) simulations have widely been used to study these structural loads. As the CFD modeling of two-phase flow has its challenges [2], new measuring techniques for CFD model validation purposes have been put into operation, such as particle image velocimetry (PIV), wire-mesh sensors (WMS), and high-speed cameras. Different camera types, from movie cameras to modern high-speed cameras, have been used to record experiments for decades, but not until lately, the high-speed cameras are used to record the experiments in more thorough manner [3-5]. As the amount of experimental data has increased significantly, the use of high-speed cameras permits more feasible data analysis.

Previously, a pattern recognition methods based algorithm was applied for vertical vent pipe experimental data [5-7], where the algorithm was used to recognize large steam bubbles from the video material and

evaluate the basic properties of the bubbles. The image analysis data of the vertical vent pipe algorithm provided also initial parameters and boundary conditions for CFD simulations. When the algorithm was successfully applied to vertical cases, a decision was made to expand the algorithm to cover horizontal spargers.

A separate effect test facility (SEF-POOL) of LUT University makes it possible to study the momentum caused by the oscillating condensing steam jets injected into the water pool using sparger orifice. A phenomenological reference system for the SEF-POOL facility is the SRV sparger pipe of a BWR. The compact size scale of the SEF-POOL facility provides good conditions for high-speed video recording and for other measuring techniques as well. The initial results from the SEF-POOL experiments have currently been analyzed for the validation purposes of the effective heat/momentum source (EHS/EMS) models [8, 9] in KTH, and 3D CFD simulations of the tests have been done by VTT [10].

The idea of the SEF-INF test series of SEF-POOL was to produce validation data for large interface two-fluid condensation and interfacial area density CFD models in sparger cases. Due to the origins of such models, the best initial validation case for them would be a test containing visible large continuous interface, i.e. a large condensing bubble. However, such conditions provide also a good environment for extending the pattern recognition algorithm for large bubbles by Hujala et. al. [5] to be applicable in sparger studies, which, in turn, could be used in CFD model validation purposes as well.

This paper presents the improvements made to the developed pattern recognition based image analysis algorithm for horizontal sparger cases, and the preliminary results of the image analysis of bubbling mode condensation oscillations recorded during the SEF-INF2 experiment of the SEF-POOL test facility

2. SEF-POOL TEST FACILITY AND SEF-INF2 EXPERIMENT

The SEF-POOL test facility was designed for the direct measurement of the effective momentum induced by a steam injection through a single hole or a few sparger holes. Fig. 1 shows a general view of the SEF-POOL test facility.

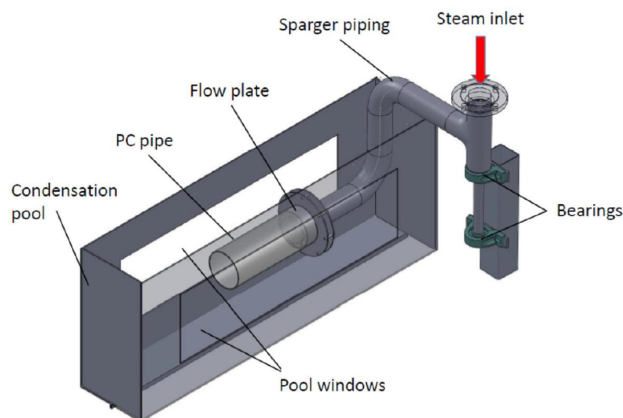


Figure 1. General view of the SEF-POOL test facility

The facility consists of an open, water-filled, uninsulated, 1500 mm long, 300 mm wide, and 600 mm high stainless steel condensation pool and an insulated stainless steel DN80 line ending up to an orifice plate. Steam line, connected to a steam generator, runs downwards from the top of the condensation pool and bends to the horizontal direction. The steam is injected through the orifice plate, which has a one or multiple orifices. Steam condensates inside an open polycarbonate (PC) pipe connected to the flow plate system, which guides replacement water to the PC tube. Different diameters of orifices can be used and the PC pipe is removable if not needed in the experiment. Large windows along both sides of the pool enable the use of high-speed video cameras and different lighting conditions. A more detailed description of the SEF-POOL test facility is presented in [11].

2.1 SEF-INF2 Experiment

A short test series, named SEF-INF, of the SEF-POOL facility, was carried out to reach the condensation oscillation (CO) and bubbling condensation oscillation modes (BCO) obtaining good quality high-speed video samples of condensing jets and bubbles. SEF-INF series consists of two experiments, SEF-INF1 and SEF-INF2, which had a different steam mass flow rates, 65 g/s, and 36 g/s, respectively. The SEF-INF2 test was chosen for this study. The initial water level on the pool was 0.47 m, and the initial water temperature was 12 °C. A flow plate with a single, diameter of 16 mm orifice, was used. The steam mass flow rate was kept constant (~36 g/s), when the corresponding steam mass flux was approximately 180 kg/(m²s). During the test, the temperature of the condensation pool water T_w increased up to 85 °C. Six video shots, named as SEF-INF2-1...SEF-INF2-6, in different pool water temperatures (44 °C - 85 °C) were recorded. The frame rate of 2800 fps was used in the video recordings, while the length of each video shot was approximately 1 s limited by the cameras data storage capacity. Fig. 2 shows the image sequence of each video shot.

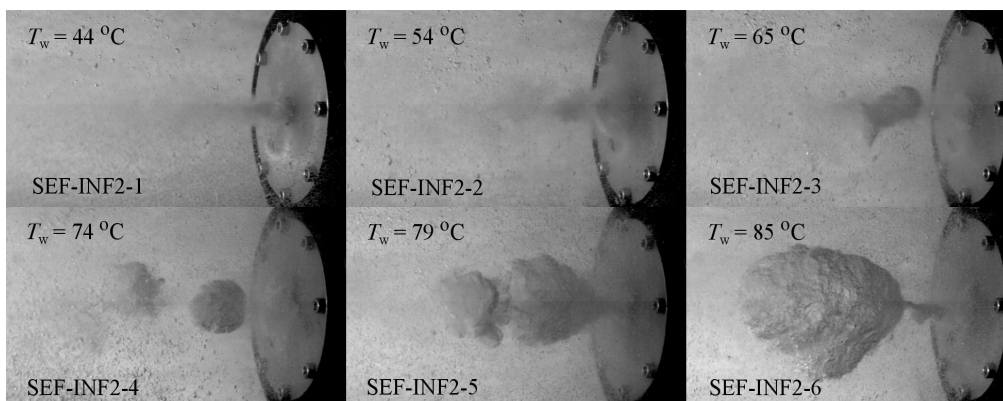


Figure 2. Examples of SEF-INF2-1...SEF-INF2-6 video frames.

A condensation mode of each test was determined using a regime map of Song et. al. [12], presented in Fig. 3. The regime map in Fig. 3 and images from the tests SEF-INF2-1...SEF-INF2-6 in Fig. 2 showed that the medium temperature (44 °C-65 °C) samples SEF-INF2-1...SEF-INF2-3 are within CO mode. The warm temperature tests SEF-INF2-4 and SEF-INF2-5 are approaching the BCO mode, and the hot temperature test SEF-INF2-6 seems to be clearly within the BCO mode.

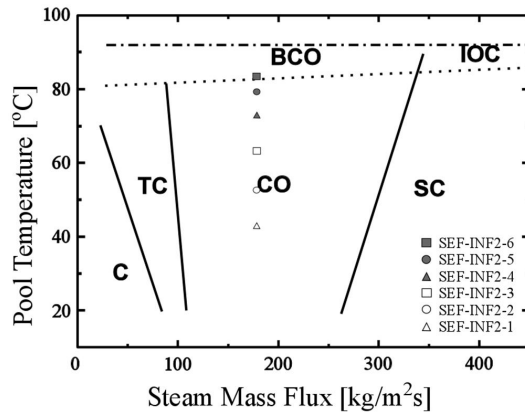


Figure 3. Regime map of Song et al., [12], in which, C refers chugging, TC transitional chugging, CO condensation oscillation, BCO bubbling condensation oscillation, SC stable condensation, and IOC interfacial oscillation condensation mode.

The regime map of Song et. al. corresponds well to the visual observations of SEF-INF2 video samples. The bubbles in SEF-INF2-6 have a clear continuous interface (called a large interface in CFD simulations) and they detach from the orifice and condense in a frequent manner. Thus, a sample of BCO mode is interesting for both, the numerical large interface condensation modeling and the image analysis of large bubbles. Furthermore, these warmed up pool BCO conditions are less frequently measured amongst and modeled modes. Thus, the SEF-INF2-6 test was chosen as a reference test for this study.

3. ANALYSIS METHODS AND LIMITATIONS

In the previously analyzed large vent blowdown experiments [5-7], steam was pushed through a large diameter (DN100/DN200) vertical blowdown pipe to the pressurized suppression pool. Typically, the system created a single steam bubble, which built up slowly, returned inside the pipe or condensed rapidly to the pool water due to chugging. The bubbles hardly ever detached from the outlet of the pipe, and usually, only one bubble appeared at a time. The pattern recognition and data analysis algorithm were successfully applied to the vertical blowdown pipe experiments, and estimations of basic features of the bubbles such as volume, surface area, vertical formation and break up velocity and acceleration of the bubble surface were obtained [5].

Because the use of image analysis and pattern recognition methods for the analysis of transient two-phase flow experiments has great potential, the image analysis algorithm has been improved further to encompass the properties of multiple simultaneous bubbles and arbitrary angles of the bubble surface velocity and acceleration.

In a horizontal sparger operating within BCO mode, the steam pushes through the orifice; bubble grows up, detaches from the orifice plate, then oscillates for a while and finally condensates disappearing. A new bubble might grow up immediately after the detachment of the previous bubble, or after a while. Probably due to the pressure oscillations, some of the bubbles or swarm of its residue bubbles even grow back before finally condensing.

When analyzing this kind of experiment with reasonable effort, a suitable image analysis algorithm is needed. The extended algorithm consists of three parts: pre-processing part, where all image processing is performed, simplified pattern recognition part, where the edges of the steam bubbles have been detected, and a post-processing part, where all image analysis and data collection takes place.

In the SEF-INF2 video material, the frames are clipped in such a way that the whole path of a bubble fits in the image. In other words, when the bubble leaves the image it is due to condensation, not just passing the border of the image. In the SEF-INF2 material, the same frame contains usually two to three bubbles – one nascent bubble, one oscillating bubble, and one vanishing bubble. Due to this more complex bubble cycle compared to the vertical blowdowns, some new analysis techniques have been applied.

The image analysis was made using MATLAB packages [13]. Pre-processing and recognition of bubble boundaries are based on the pattern recognition algorithm for the vertical blowdown pipe experiments, [5], where every pixel of the grayscale image has a certain color limit threshold. In order to distinguish a bubble, the image is compared to an empty background image, and the output image should contain only the changed pixel values that are recognized as bubble parts. The method is easy in theory, but has its weaknesses in changing conditions, for example in differing lighting levels, the appearance of a swarm of small bubbles, and bubbles due to the presence of incondensable gases. Fig. 4 shows examples of bubble borders using edge detection.

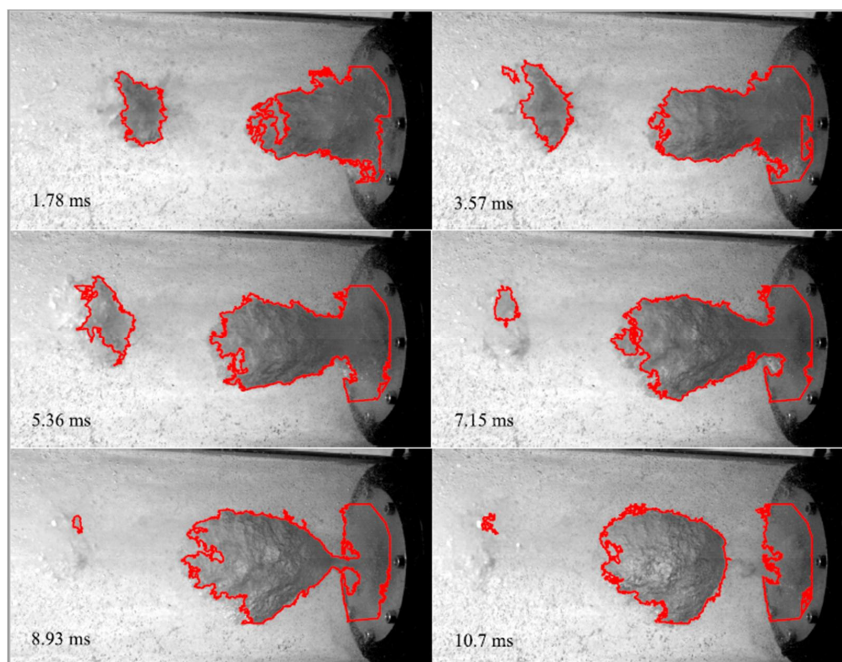


Figure 4. Every 5th frame of a 9 ms video sample from a SEF-INF2 test. Recognized boundaries are marked as red.

As is visible in Fig. 4, edge detection of the bubble boundaries has some issues due to brightness changes of the bubble surface. In these areas, the threshold limit cannot be found properly and the threshold value

of the bubble is too near to the threshold value of the background. In vertical vent cases, the threshold difference between the bubbles and the background was clear. Thus, improvements were needed with the SEF-INF2 case.

When the shadows of the bubbles make the threshold value of part of the bubble near or same as the threshold value of the background image, the boundary was detected incorrectly and an extra hole might appear inside the bubble as shown in the top left image of the Fig. 4. The frame rate of the SEF-INF2 video was 2800 fps, which means that the duration of one image is less than 0.36 ms, which is small compared to a bubble cycle. If the recognition should repair itself within a figure or two, an effective repair method can be used, even if it itself would make some errors.

The centers of mass (x_0, y_0) were calculated for all recognized bubbles. Also, every pixel of the bubble boundary has its own coordinate pair (x, y). In polar coordinates,

$$x = r \sin \theta \quad (1)$$

and

$$y = r \cos \theta, \quad (2)$$

where r is the distance from the center of mass and θ is the angle. For all recognized objects, the cartesian coordinates have been changed to the polar coordinates and the distances r from the center of mass have been calculated from 0° to 360° . In cases where recognition contains a hole in the bubble and r crosses more than one borderline, a mean value of the coordinates of the lines have been used for that direction. Fig. 5 presents a border repair method of edge detection.

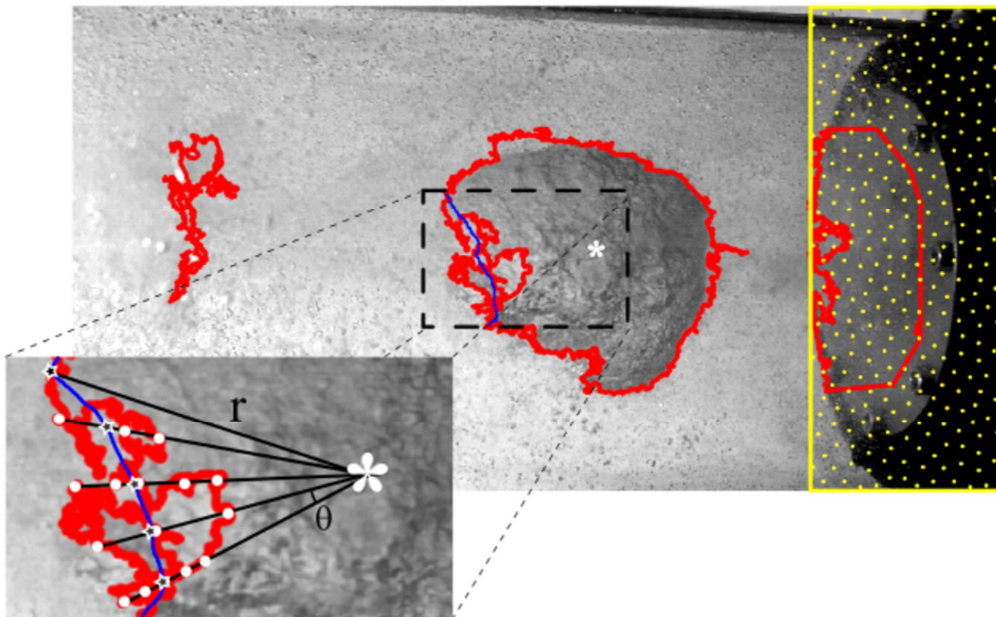


Figure 5. Improving edge detection by the border repair method.

In Fig. 5, the recognized bubble boundary (red) has an issue due to the threshold level of the left border of the bubble. Recognition does not have enough connection points, which makes a hole to the border. The distances r (black lines) from center of mass (white asterisk) in different angles θ are estimated. Due to the incorrect recognition, more than one pixels of the border (white circles) set to the same lines. The distance r was calculated for all border pixels in the same direction and the mean value is calculated (black and white stars). The blue line estimates the corrected bubble border. The method underestimates the border distance but is better than the original recognition. In addition, the maximum value of r could be used instead of mean value, which could overestimate the boundary distance in some cases. It is visible in Fig. 4 and Fig. 5 that at the beginning of the bubble growth near the orifice, pixels of the bubbles have nearly the same threshold value than the threshold value of the orifice plate. Due to this, the orifice plate region, (rectangle with dot pattern in Fig. 5) was cut out from the edge detection. Thus, edge detection takes only into account the detaching bubbles.

When a frame contains more than one bubble, an appropriate tracker algorithm was needed to connect bubbles in subsequent frames to correct bubble tracks. Tracking of the condensing bubbles was based on a Simple Tracker by Tinevez, [14]. The Simple Tracker is a particle tracking algorithm that can deal with 'gaps'. A gap happens when one particle that was detected in one frame is not detected in the next one but appears afterward. If not dealt with, this generates a track break, or a gap, in the frame where the particle disappears, and a false new track in the frame where it re-appears. In this study, the centers of mass of the bubbles act as such particles.

The Simple Tracker needs two input values, the maximum linking distance, and the maximum gap closing. The maximum linking distance defines a maximum value in bubble linking. Two bubbles will not be linked, even if they are the closest pair if the distance of their center of masses is larger than maximum linking distance. The maximum gap closing defines a maximum frame distance in gap closing. Frames further way than this value will not be investigated for gap closing. In this study, 100 pixels (px) (approx. 30 mm) maximum linking distance and the five frames gap closing value was used. In other words, when the bubble grows up tracker tracks the coordinates of the centers of mass. When a growing bubble detaches from the orifice plate and a new bubble starts to grow, this new bubble is linked to the first bubble as long as the distance between the centers of the masses of these two bubbles is smaller than 100 px. 100 px is so near that automatically all of the growing bubbles are marked new bubbles after the first bubble detachment. When a bubble starts to condensate, it might disappear for a while. If the bubble does not reappear within 5 frames, tracking of the bubble ends. If the bubble returns after the five frames gap, it will be marked as a new track, even if the distance between the returning bubble and the previous bubble is less than 100 px.

After all, tracks have been detected, all bubble life cycles should have recorded. The algorithm saves boundary pixel values of all bubbles in every image and calculates corresponding surface velocities and accelerations using the forward difference method. Also, the basic properties of the bubbles, such as volume and surface area could be evaluated.

4. RESULTS AND DISCUSSION

When all of the bubbles were recognized, tracked and linked, the final analysis can be made. Fig. 6 shows the fractions of recognized bubble lifetimes. A total of 67 bubbles were tracked. The mean lifetime of the bubbles was 0.0247 s, and bubble lifetimes varied from 0.0096 s to 0.0361 s. 70 percent of the bubbles had a lifetime between 0.020 s to 0.030 s and approximately 20 percent had the lifetime longer than that, between 0.030 to 0.037 s. All large bubbles of the SEF-INF2 experiment live longer than 20 frames (7.1 ms) and only the tracks longer than this were taken into account. Shorter tracks appeared, for example, when the bubble detached from the orifice plate and the tail of the bubble remained alone for a while. If a new bubble did not appear immediately, the tail was recognized as a useless new short track.

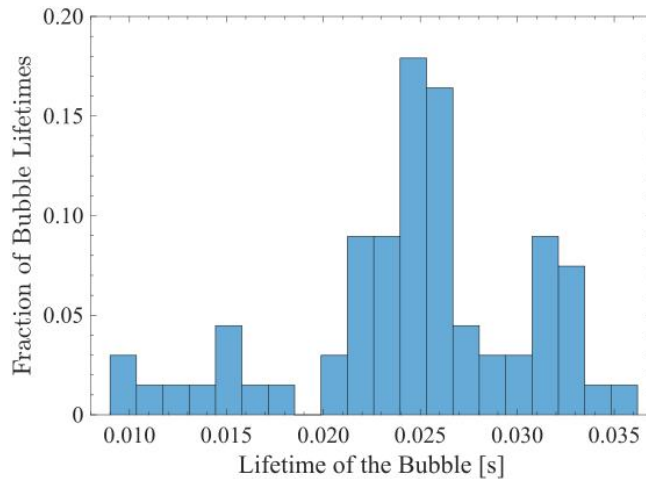


Figure 6. The fraction of 67 tracked bubble lifetimes from the formation to the condensation. The maximum linking distance was 100 px, and the maximum gap closing was five frames.

When looking at the formation frequency of the bubbles in Fig. 7 (marked as formation time), it is visible that the formation frequency stayed quite constant during the experiment. Only one longer gap in the bubble formations is visible between 0.52 s to 0.53 s of video sample and one group of increased formation frequency is visible near 0.6 s. The distribution of the formation time between two bubbles is shown in the top of Fig. 8. The line shows a normal distribution fitted to the data. Meantime difference between the bubble formations is 0.0140 seconds ranging from 0.0018 s to 0.0293 s. The line shows normal distribution fitted to data. Mean of normal distribution $\mu = 0.0139719$ s [0.0129682 0.0149755] and standard deviation $\sigma = 0.00408283$ s [0.00348571 0.00492874]. The intervals next to the parameter estimates in square brackets are the 95 % confidence intervals for the distribution parameters. The corresponding mean frequency of the bubble formation is approximately 71.6 Hz.

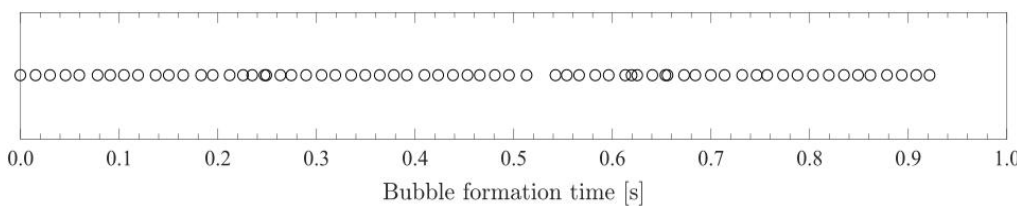


Figure 7. Formation times of the bubbles in the SEF-INF2 experiment.

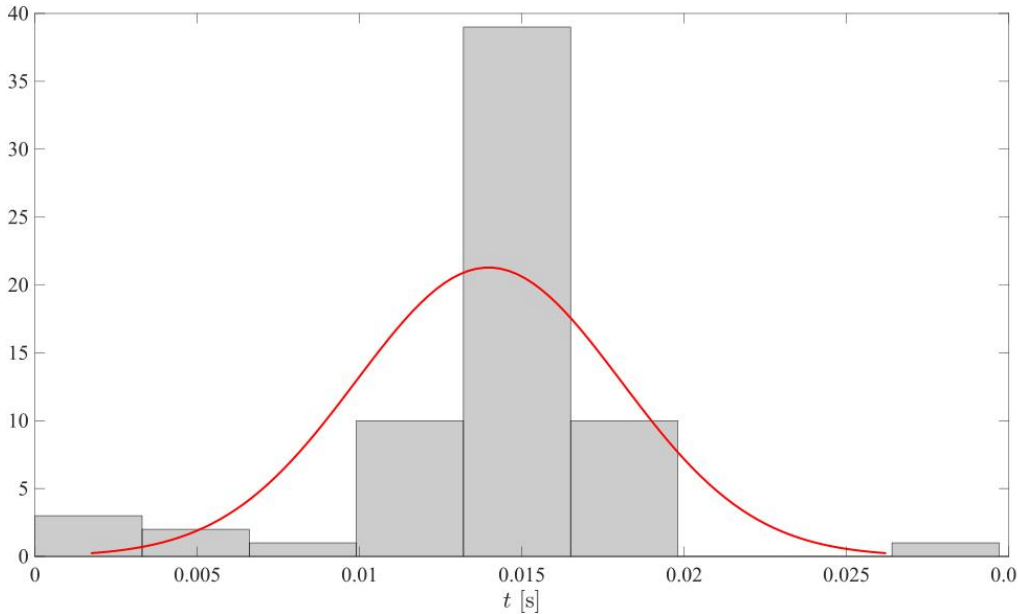


Figure 8. Time difference between two formations of 67 tracked bubbles in the SEF-INF2 experiment.

In the pattern recognition algorithm for the vertical blowdown pipes, [5], only the vertical velocity and acceleration were estimated. In this study, the arbitrary angles between 0° to 360° in 2D plane were estimated (only one camera was available, which provided video of the 2D profile of the bubbles). Fig. 9 and Fig. 10 present velocities and accelerations in different angles θ , for one tracked bubble during its lifetime. The standard polar coordinate system angle directions are used, 0° faces to the orifice and the angle increases counterclockwise.

In the Fig. 9 the positive velocity is to the bubble growing direction, in other words, from right to left. The velocities are plotted in the steps of 45° . The biggest change in the bubble surface velocities can be found in 90° direction – straight upwards. The largest velocities found in this bubble are near 50 m/s. Some bubble surfaces had the velocities larger than 80 m/s. Larger changes can be found also in other upward directions 45° , and 135° . By contrast, the forward direction, 180° , seems to be calm and changes in the velocity small for the whole lifetime of the bubble. Downward directions are quite calm, except 270° , where large, near 30 m/s change occurs at 0.03 s.

Due to the high frame rate, the calculated accelerations of the bubble surfaces grow large. The biggest acceleration difference is near $5 \cdot 10^5 \text{ m/s}^2$ to upward direction as shown in Fig. 10. To straight upward direction, only one larger change is visible at the middle of the bubbles lifetime. In other upward directions 45° and 135° , larger changes in acceleration can be seen during the whole lifetime of the bubble. Downward directions stay calm, but now horizontal directions 180° and 360° show more activity than the corresponding velocities showed.

Velocities and accelerations for all directions, in a 2D plane between 0° to 360° with 1° interval, were estimated in this study.

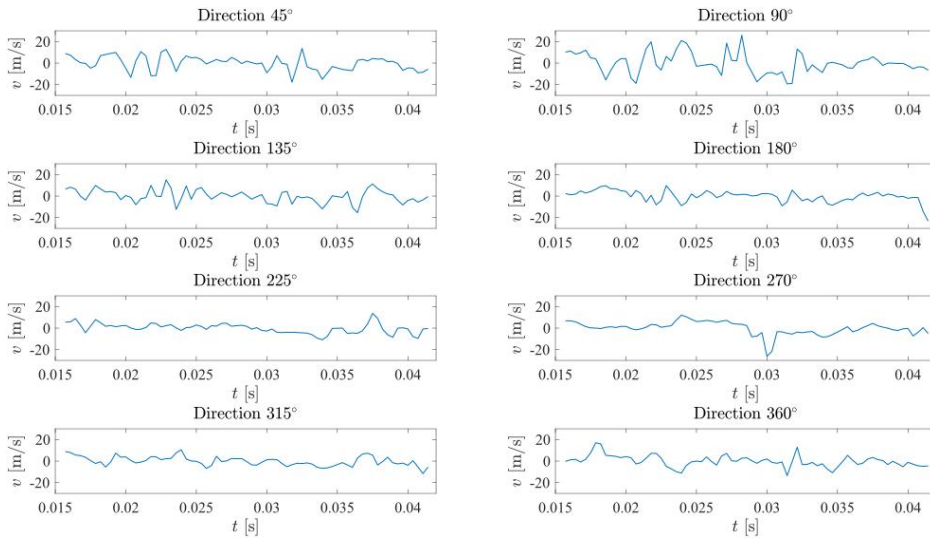


Figure 9. The velocities of one tracked bubble in the different directions from 45° to 360° in the step of 45° .

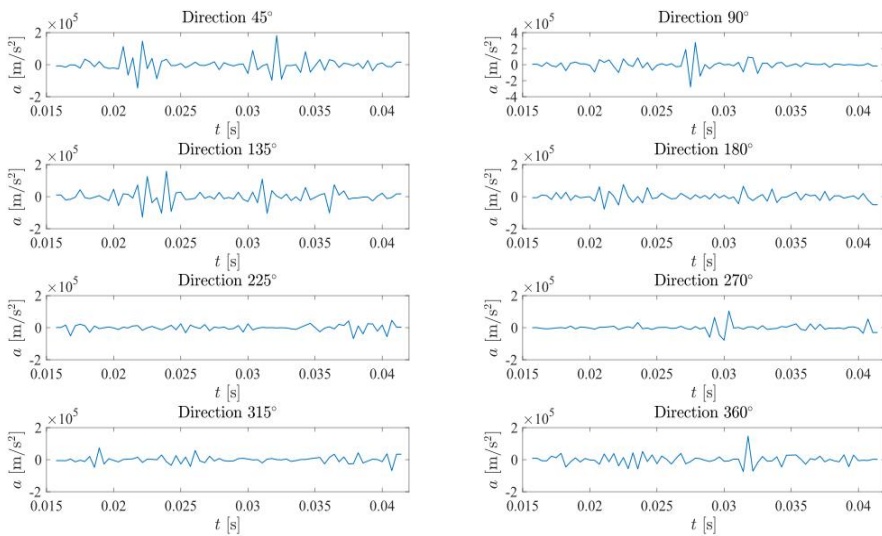


Figure 10. The acceleration of one tracked bubble in the different directions from 45° to 360° in the step of 45° .

5. CONCLUSIONS

The separate effect test facility SEF-POOL was used to study condensation oscillations in a heated up (85 °C) pool using image analysis. Six, approximately 1-second video shots of the SEF-INF2 experiment were recorded. SEF-INF2-6 test was chosen for this study. The extended pattern recognition based image analysis algorithm was developed and improvements presented in this study. A new algorithm can deal with multiple bubbles, which can temporarily disappear. The algorithm recognizes the bubble boundaries, links bubbles in the subsequent frame to each other, and tracks the whole bubble lifetime.

In total, 67 bubbles were tracked. The mean lifetime of the bubbles was 0.0247 s and the mean time difference between bubble formations was 0.0140 s when corresponding bubble formation frequency was 71.6 Hz. Higher bubble formation frequency shows that the use of a high frame rate is reasonable. In lower frame rates such as 300 fps, two consecutive bubbles might be mixed and misrecognized.

The surface velocities and accelerations were also estimated. The use of only one camera limits the evaluation for a 2D plane which increases errors in cases where bubble path changes from the original axis. Angles between 0° to 360° with a one-degree interval were considered. Velocities were up to 80 m/s and accelerations up to $5 \cdot 10^5$ m/s². The highest values were calculated to 90° (straight upward) direction. Forward and backward directions showed calm velocities, but more active accelerations. Downward directions showed mostly calm velocities and accelerations.

Image analysis and pattern recognition have great potential in thermal-hydraulic research. The image analysis algorithm has been improved and works well with multiple bubbles. With suitable video recordings, the algorithm can be used with pipe flows too. Surface velocity and acceleration estimation at arbitrary angles give important knowledge, for example in which direction condensation of the steam bubble begins and will be a good aid for CFD validation purposes.

NOMENCLATURE

BCO	bubbling condensation oscillation
CFD	computational fluid dynamics
CO	condensation oscillation
EHS	effective heat source
EMS	effective momentum source
KTH	Kungliga Tekniska högskolan (Royal Institute of Technology, Stockholm, Sweden)
LOCA	loss-of-coolant accident
LUT	Lappeenranta-Lahti University of Technology LUT
PC	polycarbonate
SEF-INF	test series of the SEF-POOL facility in INFRAL project
SEF-POOL	separate effect facility
SRV	safety/relief valve
VTT	VTT Technical Research Center of Finland LTD

ACKNOWLEDGMENTS

The research leading to these results was partly funded by the Finnish Nuclear Waste Management Fund (VYR) via the Finnish Research Programs on Nuclear Power Plant Safety SAFIR2018 and SAFIR2022. The authors gratefully acknowledge all this support.

REFERENCES

1. R. Lahey and F. Moody, *The Thermal-Hydraulics of a Boiling Water Reactor*, American Nuclear Society, La Grange Park, Illinois, USA, 2. edition, (1993). ISBN: 0-89448-037-5.
2. D. Bestion, "The Difficult Challenge of a Two-Phase CFD Modelling for all Flow Regimes," *Nuclear Engineering and Design*, 279, pp. 116-125, (2014).
3. S. Al Issa, P. Weisensee and R. Macian-Juan, "Experimental Investigation of Steam Bubble Condensation in Vertical Large Diameter Geometry under Atmospheric Pressure and Different Flow Conditions," *International Journal of Heat and Mass Transfer*, 70, pp. 918-929, (2014)
4. V.. Tanskanen, *CFD Modelling of Direct Contact Condensation in Suppression Pools by Applying Condensation Models of Separated Flow*, PhD. Thesis, Lappeenranta University of Technology, (2012).
5. E. Hujala, V. Tanskanen, and J. Hyvärinen, "Pattern recognition algorithm for analysis of chugging direct contact condensation", *Nuclear Engineering and Design*, 332, pp. 202-212, (2018)
6. E. Hujala, *Evaluation of Bubble Formation and Break Up in Suppression Pools by Using Pattern Recognition Methods*, MSc. Thesis, Lappeenranta University of Technology (2013). <http://lutpub.lut.fi/handle/10024/89985>
7. E. Hujala, V. Tanskanen, and J. Hyvärinen, "Frequency analysis of chugging condensation in pressure suppression pool system with pattern recognition", *Nuclear Engineering and Design*, 339, pp. 244-252, (2018)
8. Gallego-Marcos, I., Filich, L., Villanueva, W., Kudinov, P., "Modelling of the Effects of Steam Injection through Spargers on Pool Thermal Stratification and Mixing", Nordic Nuclear Safety Research, Research Report NKS-347, pp. 1-45. Nuclear Power Safety, Royal Institute of Technology (KTH), Stockholm, Sweden, (2015).
9. Li, H., Villanueva, W., Kudinov, P., "Effective momentum and heat flux models for simulation of stratification and mixing in a large pool of water", Nordic Nuclear Safety Research, Research Report NKS-266, pp. 1-61, Nuclear Power Safety, Royal Institute of Technology (KTH), Stockholm, Sweden, (2012).
10. T. Pättikangas and V. Hovi, "CFD simulation of condensation of vapor jets", VTT Research Report, VTT-R-00993-18, (2018)
11. K. Tielinen, A. Räsänen, E. Kotro, and I. Saure, "General description of SEF-POOL test rig", technical report, INSTAB 2/2017, Lappeenranta University of Technology, (2017).
12. C.H. Song, S. Cho, H.S. Kang, "Steam jet Condensation in a pool from fundamental understanding to engineering scale analysis," *J. Heat Transfer*, **143**, (2012)
13. MATLAB R2016b Academic license, The MathWorks, Inc. (2016)
14. J.-Y. Tinevez, "Simple tracker, version 1.5.0.0", MATLAB Central File Exchange, Retrieved 17 February 2019, <https://se.mathworks.com/matlabcentral/fileexchange/34040-simple-tracker>

ACTA UNIVERSITATIS LAPPEENRANTAENSIS

833. KARELL, VILLE. Essays on stock market anomalies. 2018. Diss.
834. KURONEN, TONI. Moving object analysis and trajectory processing with applications in human-computer interaction and chemical processes. 2018. Diss.
835. UNT, ANNA. Fiber laser and hybrid welding of T-joint in structural steels. 2018. Diss.
836. KHAKUREL, JAYDEN. Enhancing the adoption of quantified self-tracking wearable devices. 2018. Diss.
837. SOININEN, HANNE. Improving the environmental safety of ash from bioenergy production plants. 2018. Diss.
838. GOLMAEI, SEYEDMOHAMMAD. Novel treatment methods for green liquor dregs and enhancing circular economy in kraft pulp mills. 2018. Diss.
839. GERAMI TEHRANI, MOHAMMAD. Mechanical design guidelines of an electric vehicle powertrain. 2019. Diss.
840. MUSIENKO, DENYS. Ni-Mn-Ga magnetic shape memory alloy for precise high-speed actuation in micro-magneto-mechanical systems. 2019. Diss.
841. BELIAEVA, TATIANA. Complementarity and contextualization of firm-level strategic orientations. 2019. Diss.
842. EFIMOV-SOINI, NIKOLAI. Ideation stage in computer-aided design. 2019. Diss.
843. BUZUKU, SHQIPE. Enhancement of decision-making in complex organizations: A systems engineering approach. 2019. Diss.
844. SHCHERBACHEVA, ANNA. Agent-based modelling for epidemiological applications. 2019. Diss.
845. YLIJOKI, OSSI. Big data - towards data-driven business. 2019. Diss.
846. KOISTINEN, KATARIINA. Actors in sustainability transitions. 2019. Diss.
847. GRADOV, DMITRY. Experimentally validated numerical modelling of reacting multiphase flows in stirred tank reactors. 2019. Diss.
848. ALMPANOPOULOU, ARGYRO. Knowledge ecosystem formation: an institutional and organisational perspective. 2019. Diss.
849. AMELI, ALIREZA. Supercritical CO₂ numerical modelling and turbomachinery design. 2019. Diss.
850. RENEV, IVAN. Automation of the conceptual design process in construction industry using ideas generation techniques. 2019. Diss.
851. AVRAMENKO, ANNA. CFD-based optimization for wind turbine locations in a wind park. 2019. Diss.
852. RISSANEN, TOMMI. Perspectives on business model experimentation in internationalizing high-tech companies. 2019. Diss.
853. HASSANZADEH, AIDIN. Advanced techniques for unsupervised classification of remote sensing hyperspectral images. 2019. Diss.

- 854.** POPOVIC, TAMARA. Quantitative indicators of social sustainability applicable in process systems engineering. 2019. Diss.
- 855.** RAMASAMY, DEEPIKA. Selective recovery of rare earth elements from diluted aqueous streams using N- and O –coordination ligand grafted organic-inorganic hybrid composites. 2019. Diss.
- 856.** IFTEKHAR, SIDRA. Synthesis of hybrid bio-nanocomposites and their application for the removal of rare earth elements from synthetic wastewater. 2019. Diss.
- 857.** HUIKURI, MARKO. Modelling and disturbance compensation of a permanent magnet linear motor with a discontinuous track 2019. Diss.
- 858.** AALTO, MIKA. Agent-based modeling as part of biomass supply system research. 2019. Diss.
- 859.** IVANOVA, TATYANA. Atomic layer deposition of catalytic materials for environmental protection. 2019. Diss.
- 860.** SOKOLOV, ALEXANDER. Pulsed corona discharge for wastewater treatment and modification of organic materials. 2019. Diss.
- 861.** DOSHI, BHAIRAVI. Towards a sustainable valorisation of spilled oil by establishing a green chemistry between a surface active moiety of chitosan and oils. 2019. Diss.
- 862.** KHADIJEH, NEKOUJIAN. Modification of carbon-based electrodes using metal nanostructures: Application to voltammetric determination of some pharmaceutical and biological compounds. 2019. Diss.
- 863.** HANSKI, JYRI. Supporting strategic asset management in complex and uncertain decision contexts. 2019. Diss.
- 864.** OTRA-AHO, VILLE. A project management office as a project organization's strategizing tool. 2019. Diss.
- 865.** HILTUNEN, SALLA. Hydrothermal stability of microfibrillated cellulose. 2019. Diss.
- 866.** GURUNG, KHUM. Membrane bioreactor for the removal of emerging contaminants from municipal wastewater and its viability of integrating advanced oxidation processes. 2019. Diss.
- 867.** AWAN, USAMA. Inter-firm relationship leading towards social sustainability in export manufacturing firms. 2019. Diss.
- 868.** SAVCHENKO, DMITRII. Testing microservice applications. 2019. Diss.
- 869.** KARHU, MIIKKA. On weldability of thick section austenitic stainless steel using laser processes. 2019. Diss.
- 870.** KUPARINEN, KATJA. Transforming the chemical pulp industry – From an emitter to a source of negative CO2 emissions. 2019. Diss.



ISBN 978-952-335-424-1
ISBN 978-952-335-425-8 (PDF)
ISSN-L 1456-4491
ISSN 1456-4491
Lappeenranta 2019